2010

# Brachytherapy Seed and Applicator Localization via Iterative Forward Projection Matching Algorithm using Digital X-ray Projections

Damodar Pokhrel
*Virginia Commonwealth University*

School of Medicine
Virginia Commonwealth University

This is to certify that the dissertation prepared by Damodar Pokhrel entitled "BRACHYTHERAPY SEED AND APPLICATOR LOCALIZATION VIA ITERATIVE FORWARD PROJECTION MATCHING ALGORITHM USING DIGITAL X-RAY PROJECTIONS" has been approved by his committee as satisfactory completion of the thesis or dissertation requirement for the degree of Doctor of Philosophy.

Dr. Jeffrey F Williamson, Department of Radiation Oncology

Dr. Martin J Murphy, Department of Radiation Oncology

Dr. Dorin A Todor, Department of Radiation Oncology

Dr. Elisabeth Weiss, Department of Radiation Oncology

Dr. Yuichi Motai, Department of Electrical and Computer Engineering

Dr. Jerome F Strauss, Dean of School of Medicine

Dr. F. Douglas Boudinot, Dean of the School of Graduate Studies

October 29, 2010

# Brachytherapy Seed and Applicator Localization via Iterative Forward Projection Matching Algorithm using Digital X-ray Projections

**Damodar Pokhrel**

Thesis advisors: Dr. Jeffrey F Williamson, Ph.D. and Dr. Martin J Murphy, Ph.D.

Department of Radiation Oncology, School of Medicine
Virginia Commonwealth University
401 College St., Richmond, VA, 23229, United States, 2010

Doctoral Dissertation 2010
Department of Radiation Oncology, School of Medicine
Virginia Commonwealth University
Richmond, VA 23229 United States

ABSTRACT

Interstitial and intracavitary brachytherapy plays an essential role in management of several malignancies. However, the achievable accuracy of brachytherapy treatment for prostate and cervical cancer is limited due to the lack of intraoperative planning and adaptive replanning. A major problem in implementing TRUS-based intraoperative planning is an inability of TRUS to accurately localize individual seed poses (positions and orientations) relative to the prostate volume during or after the implantation. For the locally advanced cervical cancer patient, manual drawing of the source positions on orthogonal films can not localize the full 3D intracavitary brachytherapy (ICB) applicator geometry. A new iterative forward projection matching (IFPM) algorithm can explicitly localize each individual seed/applicator by iteratively matching computed projections of the post-implant patient with the measured projections. This thesis describes adaptation and implementation of a novel IFPM algorithm that addresses hitherto unsolved problems in localization of brachytherapy seeds and applicators. The prototype implementation of 3-parameter point-seed IFPM algorithm was experimentally validated using a set of a few cone-beam CT (CBCT) projections of both the phantom and post-implant patient's datasets. Geometric uncertainty due to gantry angle inaccuracy was incorporated. After this, IFPM algorithm was extended to 5-parameter elongated line-seed model which automatically reconstructs individual seed orientation as well as position. The accuracy of this algorithm was tested using both the synthetic-measured projections of clinically-realistic Model-6711 $^{125}$I seed arrangements and measured projections of an in-house precision-machined prostate implant phantom that allows the orientations and locations of up to 100 seeds to be set to known values. The seed reconstruction error for simulation was less than 0.6 mm/3$^{o}$. For the physical phantom experiments, IFPM absolute accuracy for position, polar angle, and azimuthal angel were (0.78 ± 0.57) mm, (5.8 ± 4.8)$^{o}$, and (6.8 ± 4.0)$^{o}$, respectively. It avoids the need to match corresponding seeds in each projection and accommodates incomplete data, overlapping seed clusters, and highly-migrated seeds. IFPM was further generalized from 5-parameter to 6-parameter model which was needed to reconstruct 3D pose of arbitrary-shape applicators. The voxelized 3D model of the applicator was obtained from external complex combinatorial geometric modeling. It is then integrated into the forward projection matching method for computing the 2D projections of the 3D ICB applicators, iteratively. The applicator reconstruction error for simulation was about 0.5 mm/2$^{o}$. The residual 2D registration error (positional difference)

between computed and actual measured applicator images was less than 1 mm for the intrauterine tandem and about 1.5 mm for the bilateral colpostats in each detector plane. By localizing the applicator's internal structure and the sources, the effect of intra and inter-applicator attenuation can be included in the resultant dose distribution and CBCT metal streaking artifact mitigation. The localization accuracy of better than 1 mm and $6^{o}$ has the potential to support more accurate Monte Carlo-based or 2D TG-43 dose calculations in clinical practice. It is hoped the clinical implementation of IFPM approach to localize elongated line-seed/applicator for intraoperative brachytherapy planning may have a positive impact on the treatment of prostate and cervical cancers.

CONTENTS Page

PREFACE

This dissertation is mainly based on the following papers which will be referred to in the text by their Roman numerals.

I. Damodar Pokhrel, Martin J Murphy, Dorin A Todor, Elisabeth Weiss, and Jeffery F Williamson, "Clinical application and validation of an iterative forward projection matching algorithm for permanent brachytherapy seed localization from conebeam-CT x -ray projections," Med. Phys. 37 (9), 5092-5101 (2010)

II. Damodar Pokhrel, Martin J Murphy, Dorin A Todor, Elisabeth Weiss, and Jeffery F Williamson, "Reconstruction of brachytherapy seed positions and orientations from cone-beam CT x-ray projections via a novel iterative forward projection matching method," accepted for publication in Medical Physics (September 2010)

III. Damodar Pokhrel, Martin J Murphy, Dorin A Todor, Elisabeth Weiss, and Jeffery F Williamson, "Localizing intracavitary brachytherapy applicators from cone-beam CT x-ray projections via a novel iterative forward projection matching," accepted for publication in Medical Physics (October 2010)

# A INTRODUCTION

Radiation therapy is an important modality for cancer treatment. According to NCI, almost 50% of all cancer patients are treated with radiation. Radiation may be obtained from a machine outside the body (external beam radiation therapy –EBRT), or it may come from encapsulated radioactive sources placed inside the body in or near the cancer cells (brachytherapy). In the brachytherapy treatment, the dose is delivered continuously, either over the lifetime of the source to a complete decay (permanent implants) or over a short period of time (temporary implants). The goal of brachytherapy is to apply radiation to kill cancer cells and shrink tumors, while minimizing dose to the normal tissues. This goal is not always achievable due to different types of uncertainties induced throughout the course of brachytherapy treatment. These are mainly from (1) seed and applicator localization relative to the target volume, (2) target volume definition due to image quality, (3) patient motion and anatomic deformation during implantation, uncertainty about tumor extent, inter-observer tumor delineation variation, etc. Among these sources of uncertainties, accurate seed and applicator localization relative to the target volume using digital x-ray projections is the primary focus of this thesis. Because of the rapid fall off of dose from the brachytherapy sources, small differences in the pre-planned and actual localizations can lead to large differences in planned and delivered doses. Also, accurate and complete localization of brachytherapy seeds and applicators inside the patient 3D anatomy is essential to improve image quality by suppressing metal streaking artifacts for more accurate target definition.

Several topics are discussed here to explain the overall clinical rationale for carrying out the research for this thesis. A brief description of conventional methods for interstitial and intracavitary brachytherapy (ICB) planning and treatment delivery is given. The major limitations of the conventional methods for intraoperative seed/applicator localization are reviewed. The topic is further narrowed down to developing and validating novel iterative forward projection matching (IFPM) algorithm for brachytherapy seed and applicator localization, which overcomes many of the difficulties of the conventional methods. Prostate and cervical cancers are identified as the main clinical applications of this new method. Potential application of dedicated ACUITY CBCT imaging system (Varian Medical Systems, Palo Alto,

CA) in conjunction with IFPM approach for localizing brachytherapy seeds and applicators, in support of intraoperative brachytherapy planning is emphasized.

An estimated 192,280 new cases of prostate cancer occurred in the United States in 2009. Prostate cancer is the most common cancer in men. According to American Cancer Society Facts and Figures 2009 (*ACS facts and figures*), it was estimated that there were 27,360 deaths in 2009; prostate cancer being the second-leading cause of cancer death in men.

For early stage prostate cancer patients, brachytherapy –permanent interstitial seed implantation (sources are implanted within the tumor volume) has become the standard treatment procedure in many cancer centers in the United States. Improvement in the diagnosis of disease at an early stage, and refinement in the brachytherapy procedures due to imaging, planning, and treatment delivery has led to the popularity of permanent interstitial seed implantation. Image guided brachytherapy has been shown to support long term diseases control comparable to radical prostatectomy with a more favorable profile of complications.[1] The overall prostate-specific-antigen (PSA) progression-free at 10-year survival rate is 80% to 90% for early stage (low-risk) cancer patients.[2, 3] Prostate seed implants are currently performed using $^{125}I$ ($E_{avg}$ ~ 28 keV, $T_{1/2}$ ~ 60 days) and $^{103}Pd$ ($E_{avg}$ ~ 22 keV, $T_{1/2}$ ~ 17 days) shielded radioactive sources under template and image guidance (see Figure 1 (a)). The recommended total prescription dose to the periphery of the target volume is ~144 Gy for $^{125}I$ and ~116 Gy for $^{103}Pd$ when a brachytherapy is the sole treatment modality. Brachytherapy treatments can also be administered in combination with EBRT to deliver localized doses to the patients. The main advantage of the permanent seed implant over EBRT is to deliver higher doses to the tumor (increasing the likelihood of destroying the tumor) and smaller doses to the surrounding healthy tissues. Brachytherapy has become significant convenience over seven weeks of daily EBRT treatment can be replaced by one day of outpatient surgical procedure. It is minimally invasive along with fewer side effects[4] and has resulted in continuous growth of this treatment modality.

The conventional approach of prostate seed implant involves a pre-plan method[4], (creating a treatment plan a few days or weeks before the procedure using transrectal ultrasound (TRUS) images of the patient). The prostate is then implanted according to that pre-plan on the

treatment day. Post-implant localization (after 4 to 6 weeks of implantation) of brachytherapy seeds implanted in the prostate allows for validation against the planned seed poses as well as the opportunity to recalculate the actual delivered dose. As currently practiced, post-implant dosimetry is performed using CT images acquired 4 to 6 weeks after the implantation to evaluate the dose delivered to the 90% of the prostate ($D_{90}$) and the volume of the prostate receiving the full prescription ($V_{100}$). However, this pre-plan method may introduce large uncertainties because of the alternations in the prostate shape and size, patient re-positioning and setup errors. A separate TRUS imaging is required to create a pre-plan, which causes discomfort in patient.[4]

To overcome the above difficulties , the American Brachytherapy Society (ABS) recommended the use of intraoperative planning and dosimetry to allow for the adjustment in seed placement to achieve the intended dose (without moving patient and TRUS probe between the volume study and seed insertion procedure).[5] However, the routinely used TRUS and template guided prostate seed implant provides adequate imaging of the soft tissue anatomy but it cannot localize all of the implanted seeds.[6] A major problem in implementing TRUS-based intraoperative planning is the inability (it can only localize about 60% of total the implanted seeds) of TRUS to accurately localize individual seed pose (position and orientation) relative to the prostate volume during or after the implantation.[6] Reconstructing seeds from radiographic projections and then fusing the seed coordinates with 3D TRUS is widely used in intraoperative brachytherapy planning.[7] However, the seed localization problem is difficult because of the overlapping seed clusters, image distortions[96] due to non-rigidly mounted non-isocentric C-arm imager (due to change in orientation of image intensifier with the earth's or other stray magnetic fields), uncertainties in the projection geometry, and detector motion in/out of the plane, inconstancy in seed count, patient motion, etc.

In addition to limited seed localization, TRUS has a number of limitations including an anatomy distorted by the patient lithotomy position and intrarectal imaging probe. Thus post-implant CT is the current standard of practice for evaluating and reporting the delivered dose[8-14], however, it does not allow for altering and optimizing the treatment plan intraoperatively. In addition to poor soft-tissue contrast and large (up to 8 mm when compared with axial magnetic resonance images) prostate contouring errors[15], 3D CT suffers from streaking artifacts arising

from the implanted metal seeds, overlapping seed clustering, and resolution limited by the slice thickness as shown in Figure 1 (b).

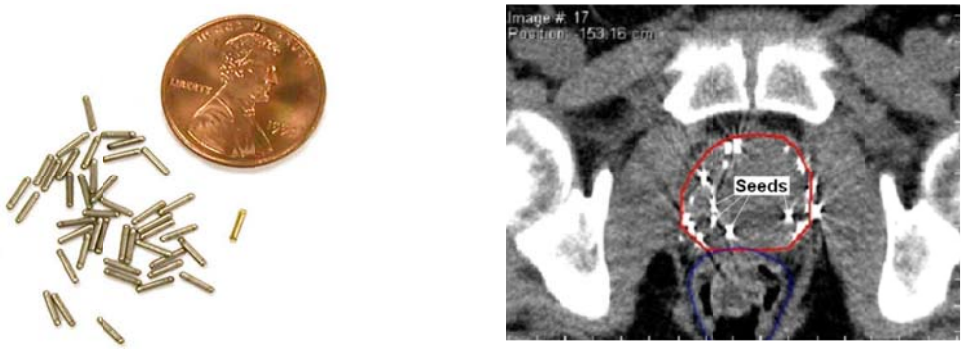


(a) (b)

Fig.1. (a) Model 6711 $^{125}$I brachytherapy seeds (*http//www/orau/ptp/collection/brachytherapy)*. Typically they are 4.5 mm in length and 0.8 mm diameter. (b) CT image of a brachytherapy prostate seed implant patient showing global effect of metal streaking artifacts arise from implanted seeds.

A major advantage of adaptive intraoperative evaluation of the dose delivery is that it would allow the identification of under-dosed regions and remedial seed placement, thus making sure that the entire prostate volume receives the prescribed dose. But the main challenge is the difficulty in accurately localizing 3D pose of the implanted seed in near-real-time and updating the dose distribution. This requires a fast, automatic, and robust method to reconstruct individual seed pose at the time of implantation. The role of intraoperative planning is not only limited to prostate cancers. Its role has been increasing in other anatomical sites such as gynecological malignancies. ICB is most commonly used in the treatment of carcinomas of the uterine cervix to deliver prescribed dose.

According to American Cancer Society Facts and Figures 2009 (*ACS facts and figures*), an estimate 53,430 cases of locally advanced cervical and endometrial cancer were diagnosed in 2009. Among them 11,850 deaths were reported. The 5-year relative survival rates for cervical and endometrial cancer patients are 71% and 83%, respectively.

ICB is a well-established and effective treatment technique for definitive treatment of locally advanced cervical cancer. It is currently performed with $^{137}$Cs ($E_{avg}$ ~ 662 keV, $T_{1/2}$ ~ 30 years) radioactive sources using low dose rate (LDR) applicators (tandem and colpostats) temporary placement. $^{137}$Cs is used because less shielding is required, and afterloading may be

performed with this source. All of the sources are encapsulated, and may be filtered to produce gamma radiation of moderate energy. But the disadvantage is that the patient is required to remain in hospital bed for the duration of the treatment. The patient has the applicator in for 48-72 hours. In modern remote afterloading devices, $^{192}$Ir ($E_{avg}$ ~ 400 keV, $T_{1/2}$ ~ 74 days) is the commonly used radioactive source for outpatient interstitial and high dose rate (HDR) brachytherapy with shorter treatment time (high specific activity). The major advantages of using HDR systems over LDR systems are dwell-time optimization of dose distribution, more accurate source/applicator positioning, reduced geometric uncertainty due to better patient immobilization, etc. However, its relatively short half-life is a particular downside, since frequent replacement of sources is required (typically 3 to 4 times annually). In addition, other disadvantages in the use of HDR systems are uncertainty in biological effectiveness and the potential risks for accidental high exposures and serious errors in the treatment delivery.

In current clinical practice, ICB planning is routinely performed manually utilizing 2D orthogonal radiographs on which single source dose distributions are superimposed. No TRUS or MR images are available for the planning purposes. Because of the poor lateral radiographic image quality, it is very difficult to accurately estimate the source position in the bilateral colpostats. A fast, automatic, and robust method is required to localize ICB applicators, in support of intraoperative brachytherapy planning and adaptive replanning.

## A.1 Conventional methods for brachytherapy seed localization

### A.1.1 3D CT-based method

For each prostate brachytherapy patient, the ABS recommends[5] that post-implant dosimetry should be performed (at week four following the implantation) by localizing seed positions using reconstructed 3D CT images.[8-14] However, as reported in the literature[9, 24] and found from our clinical experience with VariSeed (Varian Medical System, Palo Alto, CA) planning, this method frequently finds more than the actual number of implanted seeds, as the same seed may appear in more than one slice. This is mainly because of the CT slice thickness limitation and metal streaking artifacts. Difficulty in resolving overlapping seed clusters and

inter-slice spacing in reconstructed CT images are also the major causes that create difficulty in localizing seed using CT images.

Several researchers have made valuable contributions to automate the process of seed reconstruction from MRI or CT images. Roy *et al*.[8] developed a semi-automated method for reducing the number of seeds and later Feygelman *et al*.[10] modified Roy's method to interactively determine physical seed locations from the post-implant CT images. The methods presented by Brinkmann and Kline[8] and Li *et al*.[13] are based on data clustering, which determine seed positions by grouping the separate spots in CT images. They showed that the algorithm was able to identify the seed locations to within 1 mm of known locations but these methods are limited by low resolution in the *z*-direction due to inter-slice separation. Because of the CT slicing effect (partial volume averaging), a radioactive seed can appear on more than one CT slice. To overcome this difficulty, Bice *et al*.[9] designed an automated process for reduction of source location, using the nearest-neighbor approach. Yue *et al*.[12] developed another method using a pair of orthogonal scout views and a stack of transverse cuts. Liu *et al*.[14] presented a geometry-based recognition method (i.e., larger overlapping cluster areas were split into smaller ones by geometry-based filtering in each slice), which automatically determines the 3D seed position of the seed centers in a CT study of the post-implant patients. The average error was about 1.6 mm when compared against orthogonal-film technique. A promising brachytherapy seed reconstruction method using seven digital-tomosynthesis (DTS) projections has recently been applied to clinical datasets.[43] In their method, seed-only 3D binary images were obtained by back-projecting each detector pixel shadowed by an elongated seed based upon pre-reconstruction binarization of each projection. Then the seed orientation was estimated by finding the major and minor axes of the each reconstructed 3D binary voxel cluster. However, their method can not distinguish between orientations of seed clusters and individual seeds.

However, the current 3D CT-based post-implant evaluation process does not allow for intervention during the implant procedure to improve the actual treatment outcomes. 3D CT suffers from inconsistencies in both seed localization (mainly caused by CT slice thickness limitation and streaking artifacts arising from the implanted metal seeds (see Figure 1 (b)) and soft-tissue structure delineation. Also, intraoperative fan-beam CT installations in brachytherapy

suites are uncommon precluding intraoperative planning and would require moving and re-positioning the patient from the operating room (OR) to the imaging room and then back to the OR.

With the introduction of dedicated ACUITY cone-beam CT (CBCT) imaging system in the OR for seed placement, the advantages of a rigidly-mounted intraoperative imaging system and reconstruction of 3D anatomy in the same coordinate system can be combined.[93] However, the CBCT imaging system in our procedure room requires about 4 minutes (limited by constrain on gantry speed) to acquire CT images and cannot provide useful images with the TRUS probe and metal stirrups in the field of view.[65] Therefore, the current CBCT imaging is able to support only 2D projection based intraoperative brachytherapy guidance.

### A.1.2 Back-projection (BP) methods

A more common approach to 3D seed localization is the BP of seed positions in 2D x-ray projections using two-film[17] and three-film[18-23] techniques. For any given seed, BP localizes the 3D seed positions by ray-tracing from the projected seed positions backward along the projection paths and finding the point of closet intersection for the projection rays as shown in Figure 2. The two-film technique has raised the problem of matching seed ambiguity, by increasing number of projection from 2 to 3 further reducing the risk of mismatching of the seed in the projections. Taking the projections images from gantry rotations, Altschuler *et al*.[21] used 3 non-coplanar projections and reduced the ambiguity in seed matching. The reconstructed implant geometry is then fused to intraoperatively acquired ultrasound images, upon which dose planning can be performed. However, in the widely studied BP methods[24-34, 37, 38], corresponding seed in each projection must be identified and matched. This is a difficult problem mainly because of overlapping clusters[27, 34], resulting in inaccurate seed localization due to mismatch or missing seeds. While a few investigators have developed generalized BP algorithms[38, 43] for reconstructing seed orientation as well as position, they suffer from the same limitations as their more widely used centroid localization methods.

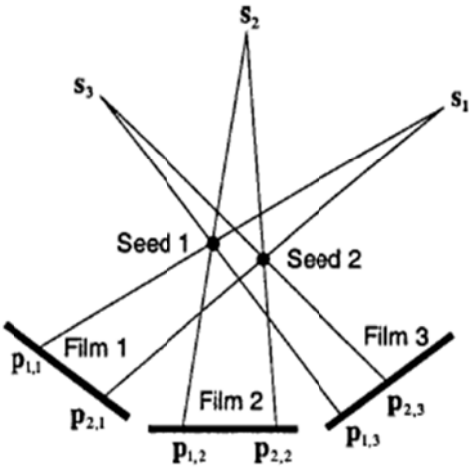


Fig.2. Illustration of the seed matching in back-projection method. Figure reproduced with permission from Todor *et al.* 2002.

Todor *et al*.[27] determined the number of seeds within a cluster by measuring the characteristics of each cluster of seeds and processing the morphological differentiation towards improved accuracy. The average error in the phantom reconstruction was about 1.5 mm. Narayana *et al*.[32] developed a method for the reduction of the matching complexity by using up to four images. Su *et al*.[34] conducted both the simulation and phantom studies on the measurement of the overlapping seed by modifying Narayanan's method. This method was very useful in identifying the overlapping seed clusters but it can not reproduce a satisfactory result for completely overlapping seeds. Lee *et al*.[29] have proposed a fluoroscopy based seed reconstruction algorithm to solve the overlapping seed problem using dimensionality reduction technique.

Patient motion and uncertainty in imaging device positioning during image acquisition can further confound seed localization when using BP methods. This particularly happens if the images are acquired using a non-isocentric mobile C-arm imager. Tubic *et al*.[25] proposed an algorithm using simulated annealing, which has integrated the motion correction up to 5 mm translation and $\pm 2.5^{o}$ in the rotational errors. Given infinite computation time, the simulated annealing is not subject to trapping in local minima. Todor *et al*.[28] and Lee and Zaider presented algorithms for intraoperative dosimetric assessment.[29] Current clinical applications rely mainly

on BP algorithms[24-34, 37, 38] for intraoperative planning. The main problems of these methods are overlapping clusters and inconsistencies in seed count due to missing seeds[33, 34], patient motion between image acquisition[36], image distortions[30, 96] and uncertainties in source and detector position[25, 26] on not-rigidly mounted non-isocentric C-arm imaging system due detector flex (moving electrons inside the image intensifier are deflected by external magnetic fields[96]) which complicates the seed reconstruction process as described earlier. One of the major challenges to BP methods is localizing the seed positions on each projection and matching each seed from one projection to the others[24-35, 37, 38] *–the so called correspondence problem*. Some clinical BP methods tried to manage this problem through morphological differentiation and identification of seed images in the clusters by heuristic learning approach[27, 28] or equally distributing the activity of the missing seeds among the reconstructed seeds in the implant.[17]

Having far better spatial resolution, radiographic seed localization can address some of the problems associated with CT-based method, including suppression of metal streaking artifacts. Recent advances in imaging and treatment delivery technology such as ACUITY CBCT now provide the opportunity to perform intraoperative dose reconstruction to further optimize the implant.[93] However, even with the resulting improvements in the calibration and stability of the imaging geometry, seed reconstruction via BP method still remains problematic.

Several algorithms are available for reconstructing 3D seed pose, including seed orientation, from measured 2D projections.[24, 25, 38] The algorithms presented by Tubic *et al.*[24, 25] use mathematical morphology to detect the center of the seeds as well as their orientation on the 2D image plane. This information (seed center and orientation in 2D) was then used to perform 3D reconstruction of each individual seed including orientation.[90] However, their method fails to correctly reconstruct seeds in large clusters of more than three seeds. Another approach, proposed by Siebert *et al.*[38], separately back-projects the tip and end positions of each seed image and uses a heuristic search algorithm to efficiently solve the NP3 matching problem. While in principle this method identifies seed orientation, no quantitative data were presented.

As currently practiced, conventional seed localization techniques only attempt to find the center of the elongated line seeds (i.e., point source approximation) for dose calculation. By

directly measuring the individual 3D pose of each implanted brachytherapy seed, more accurate Monte Carlo-based dose calculations (or 2D TG-43 dose calculations[47]) can be employed to include the effect of 2D anisotropy and interseed attenuation on the resultant dose distribution. The effect of seed orientation on the prostate dose volume histogram (DVH) for $^{125}$I seed implants was studied by Corbett *et al*.[44] They found that incorporating 2D anisotropy functions into the dose calculation slightly improved (~1%) DVH accuracy relative to the isotropic point seed model, but they did not report on local dose differences. However, the theoretical study presented by Prasad *et al*.[48] concluded that the actual dose rate may differ from the expected dose rate by a factor of 2 when taking account of the anisotropy of the individual seeds. In the post-implants geometry using $^{125}$I and $^{103}$Pd seed, Lindsay *et al*.[45] showed that omitting 2D anisotropy corrections introduced large local dose variations that collectively exceeded 10% in 20% to 40% of the target volume. Monte Carlo-based dose evaluations demonstrated that interseed attenuation[87, 89] may reduce $D_{90}$ doses by as much as 5% and dose-calculation models that account for the interseed attenuation and local seed anisotropy[88] may deviate by as much as 7.5% from one-dimensional point-source dose computations. Leclerc *et al*.[90] showed as much as 6 to 7.5% errors for the $D_{90}$ of the penile bulb and maybe about 2 to 4% for bladder and rectum when ignoring 2D anisotropy.

## A.2 Conventional methods for ICB applicator localization

Current ICB treatment planning uses orthogonal 2D radiographs to localize the radioactive sources (tandem and colpostats) in the patient.[16, 55] Because, this process involves manual drawing of the source positions on films or digital images; it is time consuming and may be prone to user error. Tandem sources are difficult to visualize in the 30% of cases for larger patient (thickness greater than 38 cm) due to poor lateral radiograph quality as shown in Figure 3. The edges of colpostats are almost always obscured in the lateral view because of the pelvic bone and the overlap of the two colpostats and the tandem shaft.[55] Source tip and end positions only localization using orthogonal films does not provide full 3D applicator pose in the CT frame. So, it can not localize full 3D pose of applicator geometry that is needed to account for intra- and inter-applicator attenuation maps for more accurate dose calculation or mitigation of metal artifacts. Brachytherapy applicators have complex internal structures[56-59], the pose of

which relative to the patient's anatomy needs to be determined for more accurate dose evaluation via Monte Carlo simulation.[59-61, 66] Monte Carlo studies have shown that applicator shielding reduces doses up to 25% when the dose distributions from the bilateral colpostats and intrauterine tandem are included.[59, 60, 63]

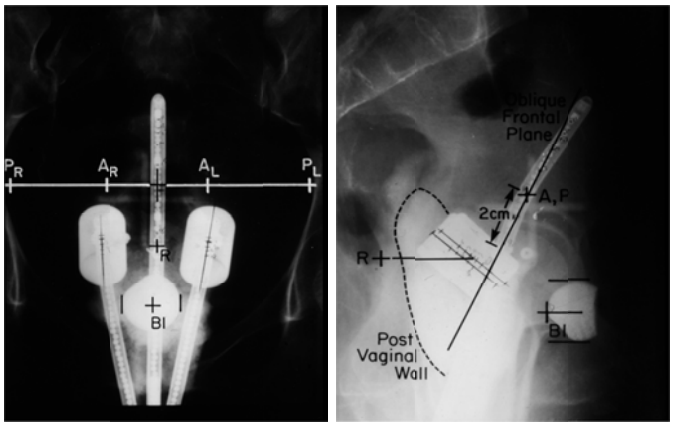


Fig.3. Orthogonal x-ray films of the ICB applicator (tandem and colpostats) patient (Courtesy of Dr. Jeffrey F Williamson).

Li *et al.*[81] has developed a method for localizing ICB applicators based on identifying several corresponding landmark points on the 2D radiographic projections, which allows the pose of the object to be reconstructed. However, the conventional ICB clinical workflow involves moving and repositioning the patient with applicator inserted on the fan beam CT table often inaccurately and then returning the patient to the treatment room. It can cause patient discomfort and may introduce large (up to 10 mm) patient setup error pertains to EBRT in combination with high dose rate brachytherapy.[64] Several methods are available for automatically localizing ICB sources and applicators from 3D CT studies[57, 61, 79] including brachytherapy catheters.[80] The plastic (low Z material) applicators developed by Schoeppel *et al.*[79] does not produce streaking artifacts in the CT images and has the ability to shield portions of the bladder and rectum by using tungsten alloy shields that are after-loadable with the radioactive sources. However, the physical size of the applicators geometry was very large which may cause patient discomfort. In the applicator pose determination, it is difficult to accurately segment and threshold fully plastic applicators components and overlap with bony structures. Weeks[57] explicitly localize applicator and source positions, by determining particular geometric features of the Fletcher-Suit applicator directly from the axial CT images. Lerma and

Williamson[61] have developed an approach in which a 3D rigid model of the external applicator shape was rigidly registered to the corresponding surface that was manually contoured in the reconstructed CT images. For typical ICB applicator orientations, they demonstrated that the localization accuracy was about 1/3 of the slice thickness. By localizing the applicator internal structure and the sources, the effect of intra- and inter-applicator attenuation can be applied to include the effect of colpostats shielding in the resultant dose distribution.[60]

Since the streaking artifact arises from the metal applicator itself, the manually drawn contour may introduce large error in dose evaluation. Applicators localization problem is closely related to the problem of metal streaking artifacts. The widely used shielded vaginal applicators[67-68] produce severe streaking artifacts limiting the value of CT imaging for segmenting critical organs at risk relative to the implanted applicators. The artifacts are mainly due to under-sampling of the photons (photon starvation) on the detector plane[68-71] that passes through the metal object (high Z material) regions of patient scans. Over the past few decades, the problem of metal artifact suppression has been studied extensively by restoring the missing information in the sinogram region either using interpolation techniques[68-71] or registering a prior metal-free CT images.[72] Another more general approach is to use iterative solutions. The alternating minimization (AM) and other iterative statistical algorithms[73-74] can provide artifact-free CT images of the soft tissues near implanted foreign metal bodies; provided that a priori model of the metal object, including its pose, shape, and attenuation map is essential when using AM image reconstruction to suppress metal streaking artifacts. Because of the excellent soft-tissue contrast, MRI-based applicator reconstruction[82-84] could be the future trend. However, as it is now, the cost associated with intraoperative MRI in brachytherapy suite causes their instillations to be uncommon and MR-compatible applicators are expensive themselves.

Automatically reconstructing applicator poses from radiographic images (with high spatial resolution) can address some of the problems associated with the post-operative CT as described above. Therefore, there is a need for fast, fully automatic, and more accurate method to localize ICB applicator to address some of the above mentioned problems.

## A.3 New method –iterative forward projection matching (IFPM) algorithm

A novel IFPM algorithm proposed by Drs. Murphy and Todor[75] was adapted in this research. A series of prototype codes, clinical workflows, and associated validation methodologies were created for accurately localizing point (see section B) and elongated line seeds inside patient 3D anatomy using as few as 3 synthetic and experimentally acquired radiographic projections. *The IFPM method was designed to avoid the major problems of BP localization methods, such as the need to determine the seed correspondences between different projections, the ambiguities presented by clustered or missing seeds in the projections, and uncertainties in the projection geometry. It accomplishes this by iteratively adapting an initial estimate of the 3D seed configuration that minimizes the pixel-by-pixel sum of the squared intensity differences (SSQD) between computed projections of the estimated seed configuration and radiographic projections of the implant until the computed seed images match the measured ones.* By matching the projection of the full seed configuration rather than individual seed projections, IFPM intrinsically accommodates incomplete and ambiguous data by recreating the overlapping seeds in the matching computed images.

This algorithm also allows the imaging viewpoints for the digitally reconstructed radiographs (DRRs) to be adjustable parameters to accommodate gantry angle uncertainties up to $8^{o}$ with respect to the first projection (i.e., the reference projection, which is not allowed to vary, other imaging viewpoints are defined relative to the first projection in terms of rotation and translation). This is a particularly useful feature if the images have been acquired using a mobile C-arm imager.

This algorithm was generalized to reconstruct the 3D pose of implanted elongated line seeds using a set of a few measured 2D projections (see section C). It was further extended to localize larger metal objects in the brachytherapy treatment, for example ICB applicators (tandem and colpostats) of arbitrarily-shape (see section D).

This thesis presents solutions for the localization of brachytherapy seeds and ICB applicators via IFPM approach using few (3 to 10) measured digital x-ray projections that

address some of the problems as described earlier including individual seed orientation measurement, resolving overlapping clusters and reconstruct full 3D pose of seed/applicator geometry. The main content of the present work concerns the development and clinical validation of the two-step 3-parameter IFPM algorithm, further development and validation of the generalized IFPM algorithms (extension from 3-parameter to 5 and 6-parameter models to localize elongated line-seed and arbitrary-shaped ICB applicator, respectively), development of a novel precision-machined multi-configuration prostate line-seed phantom, evaluation of IFPM's accuracy in the clinical setting and investigations of principle limitations of the algorithms.

## A.4 ACUITY CBCT for image-guided brachytherapy

The ACUITY CBCT imaging system used for image-guided brachytherapy in our institute has the potential to support more accurate 3D seed and applicator localization, intra- and post-operative dose planning for improving implant quality, and more accurate post-implant dose evaluation (see Figure 4). The main advantage of this imaging system for brachytherapy procedures is the relative ease and flexibility of imaging system positioning with the patient immobilized on a surgical procedure table. Availability of intraoperative 3D or planar imaging allows the localization of brachytherapy seed and applicator relative to the patient's 3D anatomy without moving or repositioning the patient. This eliminates the need to schedule a separate CT imaging procedure following release of the patient from the recovery room and allows incorrect implants to be removed/ corrected on the spot.

Fig.4. ACUITY CBCT imaging system in the brachytherapy imaging suite at our institute (VCU health system)

However, a significant challenge to brachytherapy CBCT applications is the streaking artifacts caused by implanted metal objects in the patient scan regions. Metallic seed and applicator can cause moderate to severe streaking artifacts on CBCT images that make segmentation of soft-tissues difficult and eventually introduce large error in dose calculations. As mentioned earlier, the artifacts are mainly due to undersampling of the photons on the detector plane[68-71] that passes through the metal object regions of the patient scans. The flat panel detector (FPD) used in CBCT imaging has more prominent effect of streaking artifacts due to scattered photons[85] and associate noise propagation. These effects create pronounced streaking artifacts in the reconstructed CBCT images. Therefore, more accurate pose estimate of the implanted metal object (*find the metal object boundary and its orientation in the sinogram region*) in the patient scan region is needed to study these effects and to suppress streaking artifacts. *This is important for metal streaking artifacts mitigation because if we overestimate the metal object we miss the soft-tissue information on the metal object boundary regions where as if we underestimate the metal objects we still have residual streaking artifacts.*

As mentioned earlier, the metal streaking artifacts problem is closely associated with the brachytherapy seed and applicator localization problem. The IFPM approach[75-78] can contribute to metal artifact mitigation solution by using high spatial resolution projections, rather than streak-limited CT images for seed/applicator localization and by making accurate seed/applicator pose estimates available as an input to the iterative CT images reconstruction algorithm.[73-74] CBCT sinogram projections could be adapted to validate these algorithms in the clinical setting.

## B EXPERIMENTAL VALIDATION OF IFPM ALGORITHM –point seed model

The prototype IFPM algorithm was adapted from Murphy and Todor[75] and experimentally validated in this study. It finds the set of seed positions that minimizes the pixel-by-pixel sum of the square intensity difference (SSQD) between blurred computed and experimentally acquired auto-segmented projections of the seed array. IFPM starts with an initial approximation to the seed configuration, e.g., the pre-planned seed arrangement and then iteratively refines the 3D seed positions and imaging viewpoint parameters[75] until the SSQD converges. Then the $(x, y, z)$ coordinates of each seed are independently adjusted in an iterative

search process until the computed projections optimally match the measured images (i.e., when the total SSQD for all image pairs has been minimized).

The aim of this study was to experimentally validate IFPM algorithm using both the phantom and post-implant patient's datasets in a clinical setting. Two in-house brachytherapy phantoms (12 and 72 seeds) and four selected low risk Stage-I prostate patients (60 to 81 seeds) imaged for post-implant dose evaluation intraoperatively, (i.e. approximately 4 weeks after implanting Theragenics Model 200 $^{103}$Pd interstitial sources) were included in this study. The details of this research are published in *Medical Physics,* which is included as paper I.[76]

## B.1 ACUITY image acquisition details and image post-processing

The image datasets of both the phantom (12 and 72 seeds) and patient (60, 62, 67 and 81 seeds) were experimentally acquired from the Varian ACUITY intraoperative imaging system integrated in the brachytherapy treatment room for image guidance procedures in our institute. Projection images were acquired in different gantry angle positions using the Varian 4030CB imager. The detector is 40 cm × 30 cm with a 1024 × 768 image size resulting in pixel resolution of 0.388 mm each. The ACUITY imaging geometry consists of a 100 cm source to isocenter distance (SID) and a 150 cm source to detector distance (SDD). It was operated at 80 kVp, 80 mA, and 25 ms with an exposure of 2.56 mAs /projection. The IFPM projections were selected from approximately 660 sinogram projections acquired for CBCT imaging. The choice of perspectives was based on maximizing visibility of the implanted seeds in the projections and avoiding excessively small angular parallaxes.

The post-processing involves a) cropping the images to a 256 × 256 pixel square region of interest (ROI), b) normalizing the image intensity by finding its maximum and minimum values in the image, c) morphological top-hat filtering to suppress the background, and d) automatic thresholding using the 3-standard deviation value of the pixel intensity histogram to create a binary marker for each seed in each projection in order to separate the seeds from the background. The images were processed to create binary bitmap images with zero intensity in the background and intensity of one over the area of each projected seed marker. In the phantom

study, the seed centroids were obtained by computing the center of mass for each elongated line seed marker. For the patient study, it was represented by entire radio-opaque marker of the $^{103}$Pd seed (1.09 × 0.5 mm$^2$) as shown in Figure 5. This avoids resolving seed clusters in the 2D measured projections (paper I).

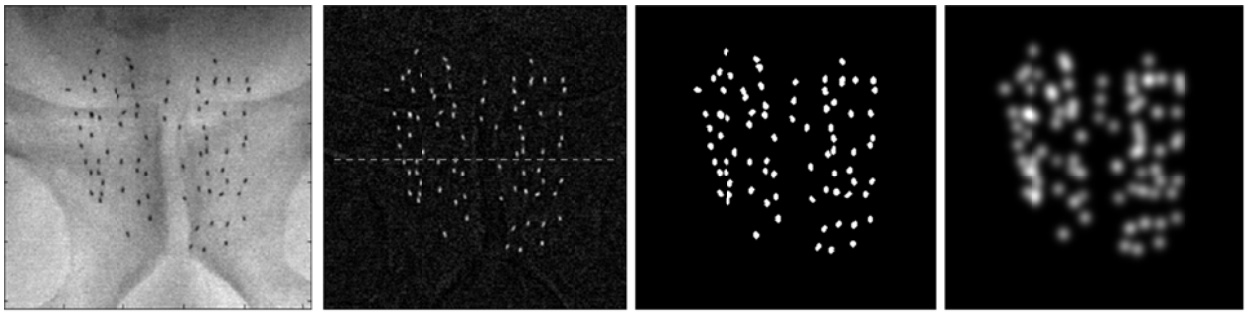


Fig.5. One image viewpoint showing an example of the image post-processing of the projection image obtained from the Varian 4030CB digital simulator; (a) raw projection image, (b) filtered image, (c) seed only image, and (d) blurred image used by IFPM algorithm for Patient III (81 implanted Theragenics model 200 $^{103}$Pd seeds).

The binary images were then convolved with a 2D Gaussian blurring function to create diffuse spots with a known intensity distribution. This produces smoothly-varying image gradients that can be computed analytically in the computed projections to guide towards minimization of the similarity, SSQD, and speed up the convergence of the matching process.

*Initial seed configuration estimates and computed projection images*

For the precision-machined phantoms, we knew the exact seed locations (with machined uncertainty of +/- 0.2 mm). The initial seeds configuration $\{\mathbf{r}\}_k$ was obtained by perturbing the known 3D seed configuration, by adding a randomly chosen displacement from a uniform distribution [-2.0 mm, +2.0 mm] in each of the three directions, resulting in a mean displacement of 1.98 mm, where k is the seed number, *N* is total number of seeds, and $0 < \mathrm{k} \leq \mathrm{N}$. In the patient study, the initial estimate of the seed configuration $\{\mathbf{r}\}_k$ was obtained from the ultrasound volume study of the prostate of the patient, which gives x, y, and z coordinates of each seed centroids within the planning target volume (PTV) for each patient. This pre-plan was used as the initial guess of the implant seed configuration. Since this IFPM algorithm used the

CBCT reference frame, the TRUS-based pre-plan coordinates were transformed to the CBCT coordinate system by using rotation, translation and scaling. As with the phantom study, the transformed 3D seeds configuration (ultrasound-to-CBCT reference frame) was rotated and translated for each imaging viewpoint and then projected on the imaging plane. The projected seeds $\{\mathbf{r}\}_k$ on the imaging plane were digitized to create the binary images and dilated one pixel along each direction to reproduce $^{103}$Pd seed like marker in the computed projections. The computed binary images of image intensity were then convolved with the same 2D Gaussian blurring function as used for measured projections.

*Similarity metric and gradient search*

The overall similarity metric, SSQD is the total of the pixel-by-pixel sum of the squared intensity differences between the all blurred computed $I_c\left(u,v\,|\,\{\mathbf{r}\}_k,\sigma,\gamma\right)$ and measured $I_m\left(u,v\,|\,\sigma,\gamma\right)$ seed image pairs (paper I);

$$SSQD\left(\{\mathbf{r}\}_k\,|\,\sigma,\gamma\right)=\sum_{\gamma}\sum_{u,v}\left[\,I_c\left(u,v\,|\,\{\mathbf{r}\}_k,\sigma,\gamma\right)-I_m\left(u,v\,|\,\sigma,\gamma\right)\,\right]^2 \tag{1}$$

where $(u,v)$ are pixel indices in the 2D image plane, $\sigma$ is the width of Gaussian blurring function and $\gamma$ is the gantry angle. The initial seed positions $\{\mathbf{r}\}_k$ were iterated by simultaneously adjusting 3D seed coordinates and the imaging viewpoints while projecting computed images. The adjustment to each degree of freedom was calculated from the gradient of SSQD with respect to that degree of freedom. After computing the analytical gradients to adjust all free parameters, the process iteratively refines the 3D seed positions and each imaging viewpoint parameters until the computed seed projections matched the measured projections of the seed geometry. The computed and measured projections must have the same imaging geometry, image size and pixel resolution. Three to six pairs of computed and measured projection image datasets with corresponding imaging geometry were used for one reconstruction process. The *3N* seed positions plus 6 (*l* -1) degrees of freedom of the imaging viewpoints are the freely moveable parameters in each iteration, where *l* = (*3, M*) is the imaging viewpoint index and *M* is the number of projections.

## B.2 Validation test with phantoms

The phantom study shows very good agreement between the IFPM seed positions and the physically measured precision-machined seed coordinates.

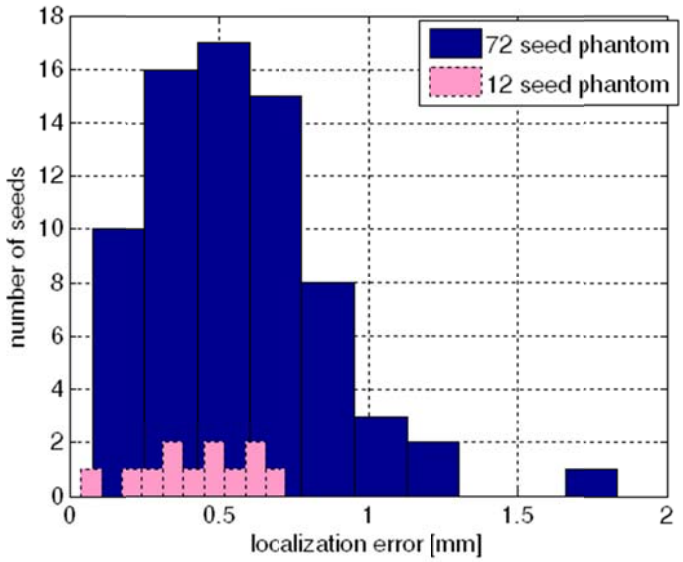


Fig.6. Histograms of the seed positional error for the 12 and 72 seed phantom study.

For the 72 seed phantom case, from one-to-one correspondence between the measured and computed sets of seed coordinates, the root-mean-square (RMS) error was found to be (0.58 ± 0.33) mm. The distribution of seed reconstruction errors is reported in the histogram in Figure 6 where it shows that greater than 96% of the reconstructed seed positions are within 1 mm from the measured seed positions. For the 12 seed phantom case, the RMS error was even smaller (0.43 ± 0.24) mm.

## B.3 Patient study

In Figure 7 we show the convergence process for a configuration of 81 seeds: Patient III. The three imaging viewpoints were positioned at $0^o$, $\pm 20^o$ gantry angle. Since, the patient datasets have overlapping seed clusters and highly-migrated seeds, we followed a two-stage iterative process in which the images were initially processed with a larger blurring function and then, after 1st step convergence, the images were reprocessed with a smaller blurring function to sharpen the resolution and complete the convergence to the final solution.

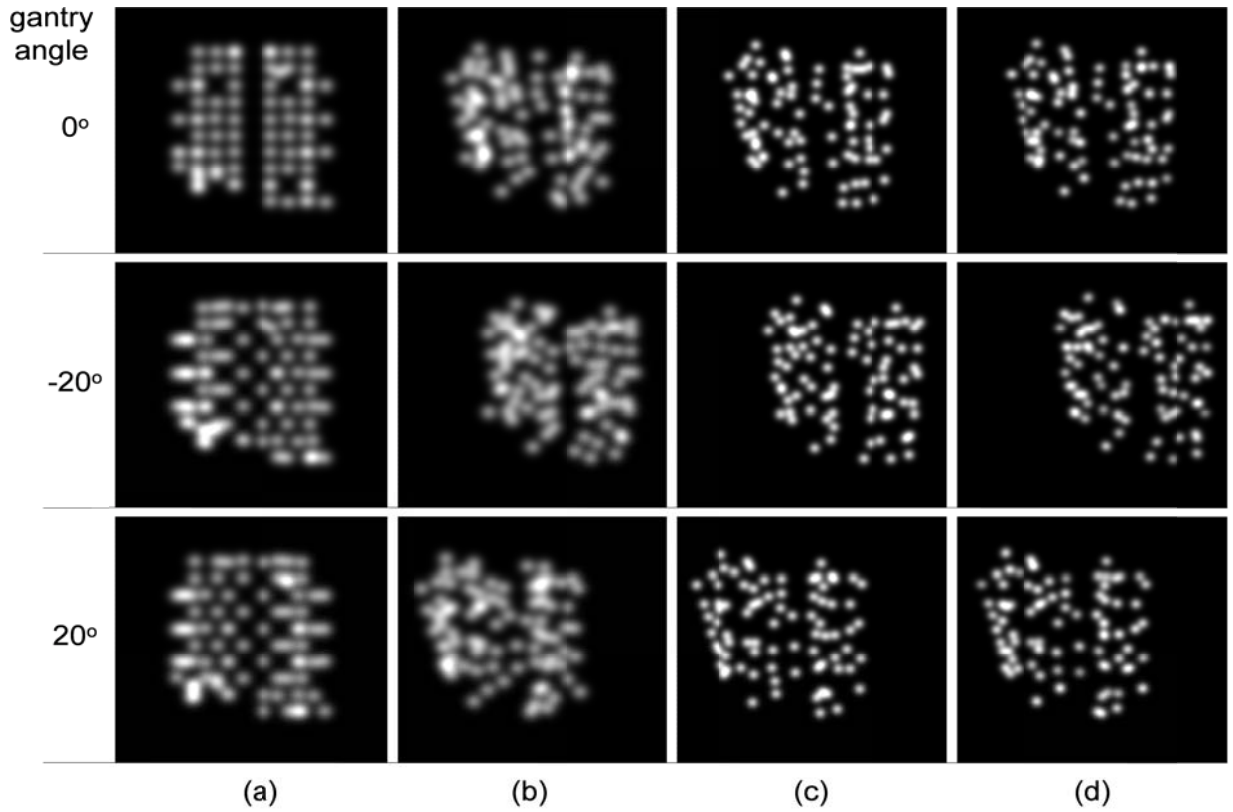


Fig.7. An illustration of the iterative sequence morphing of the convergence process, (a) initial estimate of the seed configuration, (b) computed images after first step of convergence, (c) computed images after second step of convergence, and (d) the measured images at different gantry angle for Patient III. Despite large differences between the pre-planned seed geometry (based on a TRUS volume study acquired about a week before the implant) and that observed four weeks after the implant; IFPM was able to accurately reproduce the desired seed configuration.

The initial estimate of the seed configuration (obtained from the TRUS pre-plan) is portrayed in the image group (a); the measured images are displayed in group (d). Part (b) of the figure shows the iterated seed configuration after 1$^{st}$ step convergence using the larger Gaussian blurring function; part (c) shows the final convergence after switching to the smaller blurring function. Comparison of (c) and (d) shows good agreement, including replication of overlapping seed clusters which appears as brighter or extended features in the images (paper I).

Figure 8 shows the two-stage convergence rate for the four example patient cases. The red arrow indicates that the plateau region of the SSQD when switching larger to smaller Gaussian width, for the example case patient III. Similar transitions can be seen for remaining patient's convergence histories.

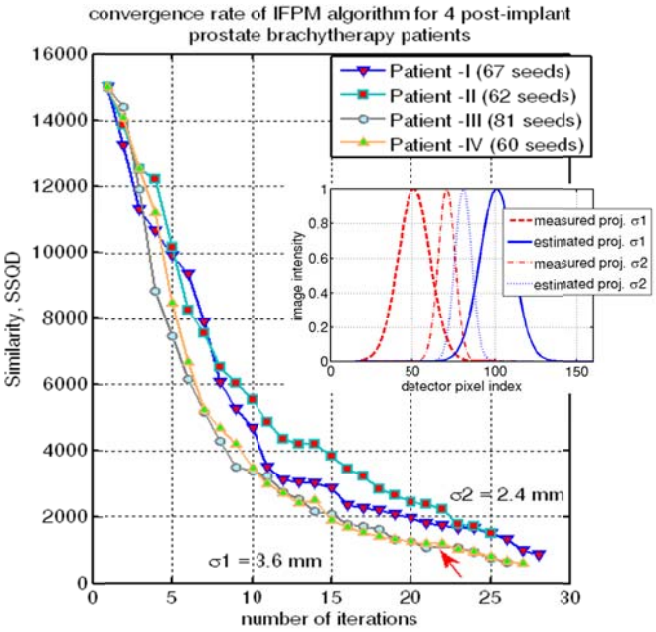


Fig.8. The convergence rate of the two step IFPM algorithm for the 4 example post-implant patient cases; Red arrow indicates that the transition from larger to smaller Gaussian spread for one of the test case. One-dimensional profile of the source attractive two-step blurring scheme can be seen in the inset.

For all example cases, the IFPM converged in 16 to 22 iterations and in 4 to 7 iterations following reduction of Gaussian blurring function width with computation time of about 1.9 to 2.8 minutes/iteration on a 1GHz processor (running time depended upon number of seeds used in the implants, i.e., the number of free parameters to optimize).

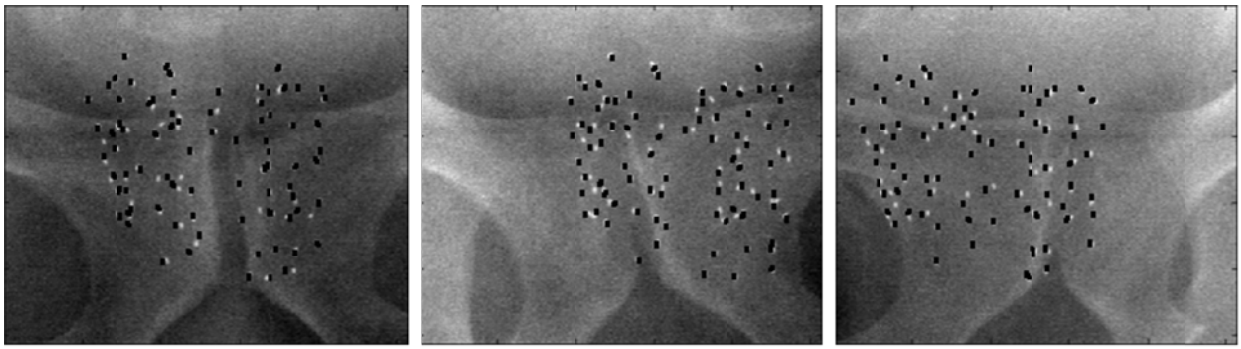


Fig.9. Superposition of measured seed images (white seeds) with automatically detected seed positions (black markers) projected on the detector planes, (a) $0^o$ gantry angle, (b) $-20^o$ gantry angle, and (c) $+20^o$ gantry angle for Patient III. While many seeds coincide exactly, a few still exhibit significant discrepancies.

An example of the reconstructed seed positions projected on the digital simulator images is presented in Figure 9 (a), (b) and (c) where the three projections are shown at $0^o$, $\pm 20^o$

respectively, along with the automatically obtained seed positions (black markers). From these images, for every candidate computed seed we empirically calculated the nearest-neighbor distance between the computed and measured seed positions on each detector plane -residual 2D registration error. The RMS errors were 0.78 ± 0.56 mm ($0^o$), 0.89 ± 0.49 mm ($-20^o$), and 0.82 ± 0.54 mm ($+20^o$), respectively. Comparison of the results obtained by IFPM algorithm, and those obtained by the VariSeed (Varian Medical Systems, Palo Alto, CA) planning provided a measure of the accuracy in the positions deduced by IFPM, as summarized in Table I for all example case patients. Since we don't know the ground truth for the patient study, this seed localization error includes not only the error from the IFPM algorithm but also the error contributed by the VariSeed planning system. In Table I we also show the residual 2D registration error while comparing against measured seed projection in each image plane. In all cases the RMS value of the seed registration error was better than 1 mm and maximum seed displacement ($d_{max}$) did not exceed 2.5 mm on the detector planes (paper I). Experiments showed that increasing the number of projections from 3 to 6 reduces this error approximately by a factor of $\sqrt{2}$ at the cost of doubling computation time.

TABLE I. Summary of the comparisons of the seed positions deduced by the IFPM algorithm and by the VariSeed planning system for all example case patients. The mean value, standard deviation (sd) in each of the three directions, and overall 3D RMS error is reported. The seed registration error in the 2D image plane in terms of RMS value. The sd and the maximum displacement ($d_{max}$) of the seed is also presented.

| | | | IFPM vs VariSeed (mm) | | | | 2D registration error in each image plane (mm) | |
|---|---|---|---|---|---|---|---|---|
| Patient no. | Image viewpoint used (deg) | Total no. of iterations | $\overline{\delta x} \pm$ sd | $\overline{\delta y} \pm$ sd | $\overline{\delta z} \pm$ sd | 3D RMS error | RMS error | $d_{max}$ |
| I | 0 | 28 | 0.38 ± 0.97 | 0.20 ± 0.98 | 0.25 ± 0.87 | 1.64 ± 0.54 | 0.63 ± 0.86 | 1.96 |
| | +15 | | | | | | 0.74 ± 0.53 | |
| | −16 | | | | | | 0.78 ± 0.72 | |
| II | 180 | 25 | 0.35 ± 0.98 | 0.19 ± 1.08 | 0.26 ± 0.89 | 1.76 ± 0.59 | 0.82 ± 0.83 | 2.44 |
| | −160 | | | | | | 0.94 ± 0.74 | |
| | +165 | | | | | | 0.86 ± 0.92 | |
| III | 0 | 26 | 0.22 ± 0.96 | −0.24 ± 0.97 | 0.23 ± 0.92 | 1.58 ± 0.56 | 0.78 ± 0.56 | 2.35 |
| | −20 | | | | | | 0.89 ± 0.49 | |
| | +20 | | | | | | 0.82 ± 0.54 | |
| IV[a] | 0 | 27 | 0.37 ± 1.16 | −0.29 ± 1.04 | 0.28 ± 0.98 | 1.86 ± 0.68 | 0.83 ± 0.63 | 2.48 |
| | −20 | | | | | | 0.98 ± 1.22 | |
| | +18 | | | | | | 0.96 ± 0.82 | |

[a]Incomplete data case.

A novel IFPM method was experimentally validated to reconstruct 3D brachytherapy seed configurations from measured 2D projection images. The iterative process doesn't require one to establish seed correspondences between the projection images. It also estimates the gantry angle if unknown or incorrect. This study shows that IFPM provided about 0.5 mm accuracy in

reconstructing the 3D positions of brachytherapy seeds when tested on 12 and 72 seed phantom datasets using CBCT x-ray projections. In the patient study, we obtained better than 1 mm accuracy tested against measured projection images.

By matching overall image content rather than individual seed projections, IFPM intrinsically accommodates incomplete and ambiguous data (i.e., missing seeds in the measured or computed projections) by iteratively recreating the overlapping seeds in the computed images (paper I). It is also observed that IFPM successfully found the overlapping seed clusters and the highly-migrated seeds.

To improve the accuracy of the seed localization validation study, we have designed and fabricated a novel prostate seed implant phantom and tested IFPM performance against a more accurate ground truth (paper II). Also, more extensive evaluation of the initial estimate as well as more optimal search of the blurring parameter with elongated overlapping seed clusters is being investigated as an extension of this method (paper II). Other geometric uncertainties such as detector in/out of plane motion and inaccuracy in the magnification factor are also an area of future investigation.

These early test cases of the IFPM algorithm found the $(x, y, z)$ coordinates of the seed centroids. The data presented here suggest that the IFPM algorithm works effectively for seeds with radio-opaque components having an aspect ratio no larger than 2:1 ratio characteristic of the Model 200 $^{103}$Pd source. Other currently available brachytherapy seeds satisfying this criteria include the Prospera Model MED3631[39], IsoAid Advantage™ Model IAPd-103A[40], and Best Model 2335 sources.[41] The point-seed model can not reproduce the alignment (orientation) of highly elongated seed, such as Model 6711 $^{125}$I. *The IFPM method described in paper I does not accurately localize seeds centers with un-process highly elongated radiographic markers. This is because the disk-shaped binary seed image modeled by the forward projector within the algorithm does not reproduce the binary images produced by cylindrical seeds in shape and size, which can vary from a small disk to highly elongated rectangles depending on seed orientation.* For highly elongated seeds such as Model 6711 $^{125}$I, which dominate the market there are two additional degrees of freedom for each seed that describe their orientation in the 3D space.

Therefore, our next developmental priority is to model an entire elongated line-seed and match with the measured projections. This allows IFPM to estimate individual seed orientations and locations that has been characterized by five degrees of freedom of each line-seed model (paper II).

*Innovation/Impact*

Our results demonstrate ~1 mm accuracy in reconstructing the 3D positions of brachytherapy seeds from the measured 2D projections of the post-implant patients. IFPM successfully localizes overlapping clustered and highly migrated seeds in the implant. Post-implant imaging is currently done four weeks after implant but can potentially be done intraoperatively via CBCT to permit immediate post-implant dosimetry assessments. The fully automatic IFPM algorithm is accurate, robust, and capable of completing a reconstruction in a few minutes using state-of-the-art workstations and is therefore a highly promising tool for implementing fusion-based intraoperative brachytherapy planning a reality.

## B.4 Sinogram interpolation and CBCT image reconstruction

Metallic $^{103}$Pd or $^{125}$I seeds cause moderate to severe streaking artifacts on CBCT images introducing errors in soft-tissue segmentation, deformable image registration and CT-based dose calculation. Accurate identification of the metal seed boundary and its orientation in the sinogram region is very important for metal streaking artifacts suppression. *Overestimation of the seed regions on the sinogram projections results in the loss of soft-tissue information on the boundary regions where as underestimation results in the residual streaking artifacts from metallic seeds themselves.*

Once the accurate *feature (metal object boundaries) of the implanted seed from the measured sinogram is* obtained, the seed only image can be subtracted from the original projections. The missing soft-tissue information's obscured by the metal seed can be recovered by 2D interpolation between the edges of the each metal seed region as shown in Figure 10.

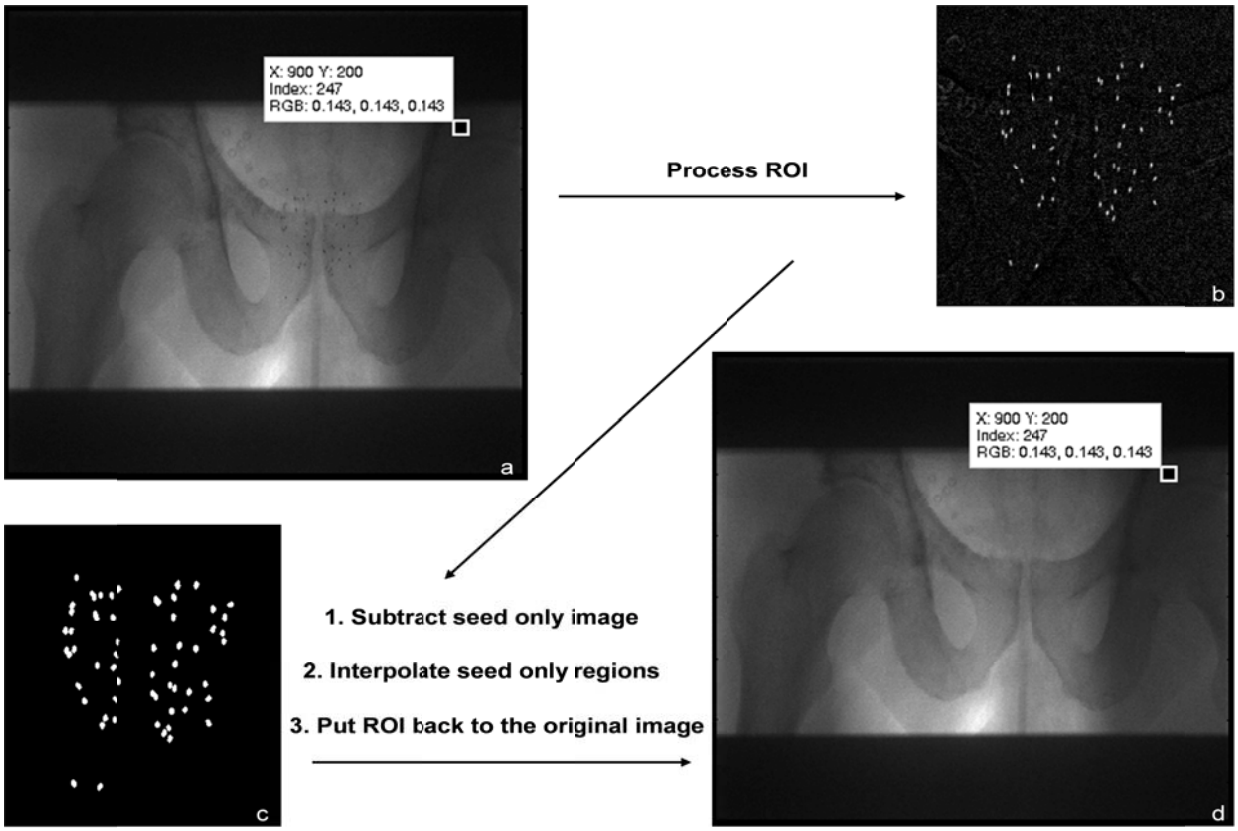


Fig.10. Seed features extraction and removal from the sinogram projections for a post-implant patient, (a) raw projection image showing implanted 60 $^{103}$Pd brachytherapy seeds in one projection, (b) filtered image region of interest (ROI), (c) seed only image ROI, and (d) same projection image after using 2D natural-neighbor interpolation over each metal seed region only.

The 2D natural-neighbor interpolation method[86] was used to interpolate inward from the pixel values corresponding to the boundary of the nonzero pixels in the grayscale image. After completing interpolation (i.e. recovering missing soft-tissue information obscured by the implanted metal seeds), the processed ROI encompassing implant was inserted into the original projection (see Figure 10) and the corrected projections were sent for CBCT image reconstruction. An in-house FDK algorithm[65] was used to reconstruct CBCT images with and without removing seed images from projections. Projection images were normalized by dividing with the norm phantom calibration data. The reconstructed images were 512 × 512 with voxel $0.5 \times 0.5 \times 3$ mm$^3$. Ramp filter was used to filter sinograms before back-projection. In Figure 11 (a) and (b) it shows the reconstructed ROI of a transverse central slice images with seeds and removed seeds. The corrected images exhibit significantly improved image quality in and around the prostate.

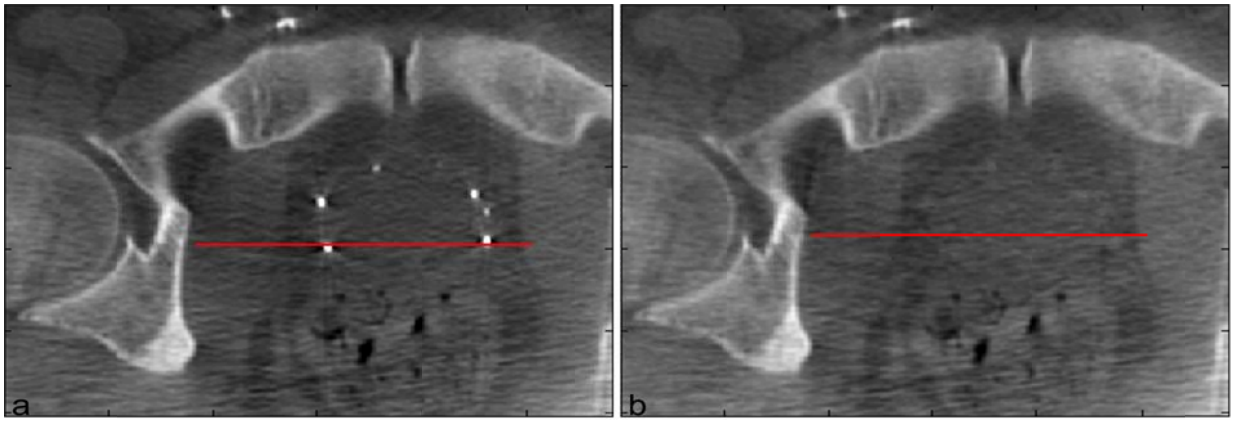


Fig.11. Central slice of the reconstructed CBCT image-ROI of Patient I, (a) without seed projection removal showing streaking artifacts, and (b) with projected seed image suppression showing significant streak reduction; some residual artifact remains because only about 30% of seeds could be segmented in the right/left lateral projections.

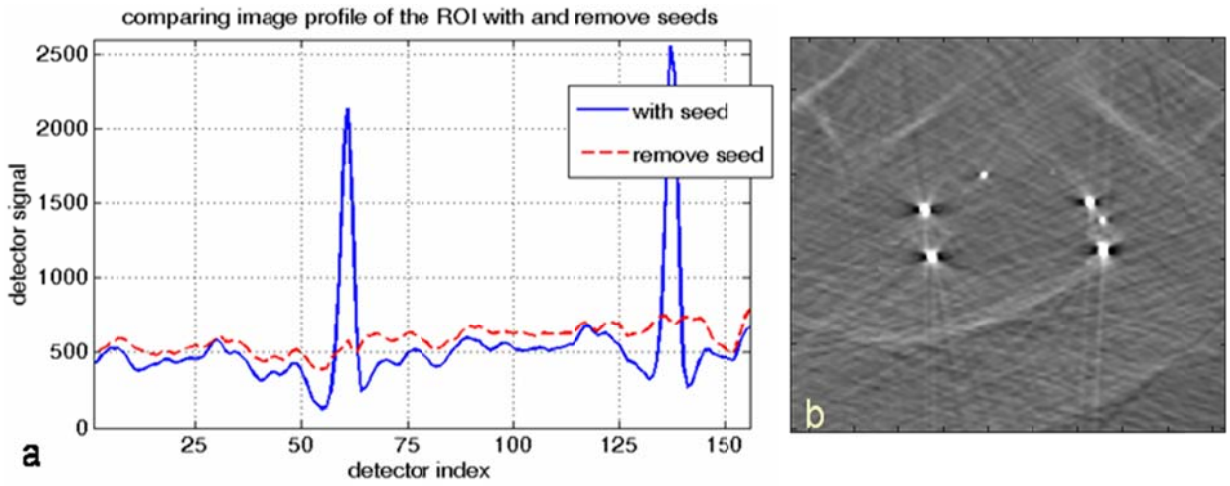


Fig.12. Comparison of image-intensity profiles along horizontal red lines in Figure 7, showing 4.5-fold reduction of streaks after correction, (b) uncorrected minus corrected difference image, clearly illustrating global effects of metal streaking artifacts.

The image profiles and a difference image on a single central slice are shown in Figure 12 (a) and (b). The streaking artifact is reduced by a factor of 4.5 and artifact spatial extend. Our preliminary results indicate that this method can be used to mitigate metal streaking artifacts specific to the brachytherapy seed implant geometry. By reducing streak and associated noise propagation artifacts, significant clinical value can be added to brachytherapy CBCT imaging. Improving the auto-segmentation method particularly in the lateral views and applying scatter subtraction with beam-hardening correction will improve the CBCT image quality for the intra/postoperative brachytherapy patient's images.

Our 5-parameter model (see section C) can be extended from CBCT sinogram projections to fan-beam CT sinogram to estimate the seed pose. *After obtaining the elongated metal seed features, one can interpolate the sinogram over seed only regions and reconstruct images with removed seed*. IFPM has a potential to replace seed localization method based on post-reconstructed 3D CT images and become the new industry standard.

## C RECONSTRUCTIONS OF SEED ORIENTATION AND POSITION VIA GENERALIZED IFPM ALGORITHM –line seed model

Point-seed model (paper I) does not reproduce the alignment (orientation) of highly elongated line seeds. For the highly elongated line seeds such as Model 6711 $^{125}$I, there is sufficient information in the projections to constrain not only the seed locations but also the two additional degrees of freedom per seed that describe their orientations in the 3D space. The point-seed matching IFPM algorithm[75-76] was generalized (gIFPM) to reconstruct individual seed orientations as well as positions. This extended 5-parameter line-seed model finds the set of seed pose parameters that minimizes the pixel-by-pixel SSQD between computed and measured auto-segmented projections of implanted seeds. The gIFPM starts with an initial approximation to the seed configuration, e.g., TRUS pre-planned seed arrangement, and then iteratively refines the 3D seed poses and imaging viewpoint parameters[75-76] until the SSQD converges. Then the $(x, y, z, \theta, \varphi)$ coordinates of each seed are independently adjusted in an iterative search process until the computed images optimally match the measured images.

The rationales for extending our 3-parameter point-seed to 5-parameter line-seed model are as follows,

a) Our previous work (paper I) demonstrated that the point-seed model can not accurately estimate the centroids of un-processed elongated line seeds because of the requirement that computed projections produce seed shadows that closely approximate the shape and size of the actual seed binary images. gIFPM is better because it does not require an extra image processing step to isolate each individual seed and will be more accurate than IFPM because it is working with more information in the 2D projections.

b) As currently practiced, conventional seed localization methods only attempt to find the center of the elongated line seeds (i.e., point source approximation) for dose calculation. Resolving overlapping seed clusters in the implant is another major difficulty of the conventional methods. By directly measuring the individual 3D pose of each implanted brachytherapy seed, more accurate Monte Carlo-based dose calculations (or 2D TG-43 dose calculations[47]) can be employed to include the effect of 2D anisotropy and interseed attenuation on the resultant dose distribution.

c) Digital extraction and removal of elongated line seed features (*metal object boundary and its orientation*) from measured 2D sinogram projections is worthwhile for reducing metal streaking artifacts by re-projecting each metal seed boundary onto the sinogram so that the missing information can be recovered from the surrounding soft-tissue image texture by 2D interpolation. By reducing streak and associated noise propagation artifacts, significant clinical value can be added to brachytherapy CBCT imaging.

The main aim of this study was to generalize and experimentally validate a novel algorithm for reconstructing the 3D pose of implanted brachytherapy seeds from a set of a few measured 2D CBCT x-ray projections. Numerical simulations of clinically realistic brachytherapy seed configurations were performed to demonstrate the proof of principle. A precision-machined multi-configuration brachytherapy seed phantom was designed and fabricated to experimentally validate this algorithm. This phantom supports precise specification of seed position and orientation of up to 100 seeds at known values for computed implant geometries. The details of this research are accepted for publication in *Medical Physics,* which is included as paper II.[77]

## C.1 Characteristics of gIFPM algorithm and the objective function

The general characteristics of the line-seed model (paper II) are highlighted below.

a) An initial estimate of the seed configuration is obtained from the clinical pre-treatment TRUS volume studies of the actual patient as described in paper I.

b) In practice, the Bresenham line drawing algorithm[46] is used to represent each seed by a finite set of equally-spaced points between two end points, $\mathbf{r}_1$ and $\mathbf{r}_2$ of the seed in the 3D space as shown in Figure 13.

c) The similarity metric (objective function) and the gradients of the similarity with respect to three positional $(x, y, z)$ and two orientation $(\theta, \varphi)$ coordinates of each seed can be computed analytically.

d) Provided that the 2D seed images can be segmented, it is not necessary to calculate complete DRRs of the estimated seed configuration via attenuation ray tracing through the patient's anatomy –it is sufficient to project line segments modeling the 3D structure of each seed along the rays from x-ray source to detector. This avoids the time-consuming task of computing complete DRRs.

e) Our IFPM approach does not require transforming cylindrical seed images into point-like landmarks. Instead, we match elongated line-seed features in the 2D images including overlapping seed clusters. This avoids a major difficulty encountered by BP methods: resolving seed clusters and isolating each seed centroid before reconstruction.

f) Reconstruction accuracy of overlapping seed clusters and highly migrated seeds can be improved by adapting a two-step blurring scheme, in which the output of the 1st step convergence is used as an input for the 2nd step with reduced Gaussian blurring (paper I and II). The optimal values of $\sigma_1$ and $\sigma_2$ were obtained from trial and error for each seed configuration.

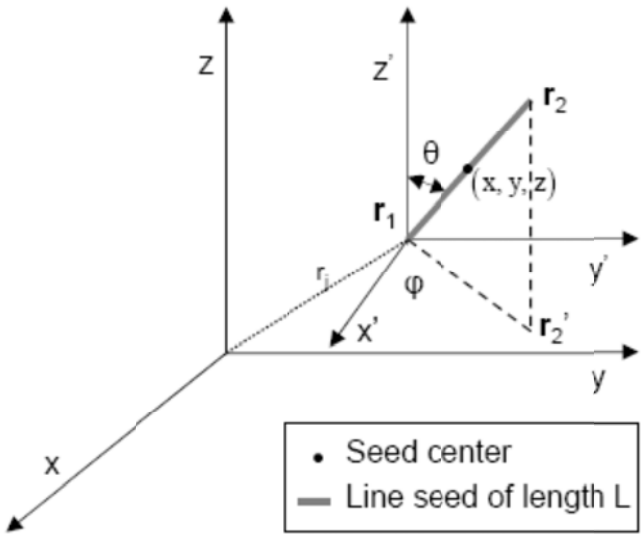


Fig.13. Elongated line seed of length, L is characterized by the seed center (black dot) positions, $(\mathrm{x}, \mathrm{y}, \mathrm{z})$ and orientation coordinates, $(\theta, \varphi)$ angle-pair in the world coordinates frame; where, z is the axis of implantation.

*Similarity metric and gradient search*

The metric sum-of-squared-differences (SSQD), which describes the "similarity" between all grayscale images, $I_c\left(u,v \mid \{\mathbf{r}_k, \mathbf{\Omega}_k\}, \sigma, \gamma\right)$ of a candidate set of the seed poses $\{\mathbf{r}_k, \mathbf{\Omega}_k\}$ and the corresponding experimentally acquired or "measured" images, $I_m\left(u,v \mid \sigma, \gamma\right)$ at nominal gantry angle γ, is given by (paper II),

$$SSQD\left(\{\mathbf{r}_k, \mathbf{\Omega}_k\} \mid \sigma, \gamma\right) = \sum_{\gamma} \sum_{u,v} \left[ I_c\left(u,v \mid \{\mathbf{r}_k, \mathbf{\Omega}_k\}, \sigma, \gamma\right) - I_m\left(u,v \mid \sigma, \gamma\right) \right]^2 \tag{2}$$

where, $\mathbf{\Omega}_k = \left(\sin\theta\cos\varphi, \sin\theta\sin\varphi, \cos\theta\right)_k$ is the direction cosine vector which is related to the original pose angular variables $(\theta, \varphi)_k$ for each seed k in the 3D space and $(\mathrm{u}, \mathrm{v})$ is the 2D detector plane. The nonlinear gradient of the similarity, SSQD with respect to three positional and two orientations degrees of freedom were analytically computed, for example, with respect to x coordinate,

$$\partial(SSQD)/\partial x_k = 2\sum_{\gamma}\left( \sum_{u,v}\left[ I_c\left(u,v \mid \{\mathbf{r}_k, \mathbf{\Omega}_k\}, \sigma, \gamma\right) - I_m\left(u,v \mid \sigma, \gamma\right) \right] \partial I_c\left(u,v \mid \{\mathbf{r}_k, \mathbf{\Omega}_k\}, \sigma, \gamma\right)/\partial x_k \right) \tag{3}$$

Since, the brachytherapy line seed has rotational symmetry around the axis of rotation; we computed one derivative per seed per degree of freedom with respect to the each seed center coordinates. Because the image grayscale intensities are represented entirely by the Gaussian blurring function, the grayscale image gradient, $\partial I_c\left(u,v\,|\,\{\mathbf{r}_k,\boldsymbol{\Omega}_k\},\sigma,\gamma\right)\big/\partial x_k$ for each seed was calculated analytically from the computed image for that degree of freedom. Similarly, we computed the first derivatives of SSQD with respect to the other spatial and angular coordinates. Detailed derivations of the gradient calculation can be found in the appendix (paper II). See algorithm workflow in appendix 1.

The perturbation to each degree of freedom was computed from the gradient of SSQD with respect to that degree of freedom. Since, the brachytherapy line-seed has rotational symmetry around the axis of rotation; we computed one derivative per seed per degree of freedom with respect to each seed center coordinates. The steepest-descent search process with a parabolic approximation uses the gradient to iteratively refine the 3D seed pose and imaging viewpoint parameters until the iterative process converges (typically 6 to 20 iterations). At least two, but preferably three or more pairs of computed and measured projection image datasets with corresponding imaging geometry are required for one reconstruction process.

### C.2 Validation via simulated implant geometries

Simulated line-seed implants were created by obtaining clinical pre-plan seed configurations based upon pre-treatment TRUS volume studies of actual patients, which gave the *x*, *y*, and *z* coordinates of each seed centroids within the planning target volume. These coordinates are transferred to the CT coordinates system and then modified to obtain extended line seeds ($L$ = 4.5 mm and 0.8 mm diameter) in 3D space and assigned $\theta = 0$, $\varphi = 0$ for each seed as shown in Figure 9, where, *z* –needle direction. More realistic synthetic measured projections (3 to 10) were created by randomly sampling centroid locations, from uniform ±2.0 mm distributions in each direction. Similarly, θ and φ-values were sampled from the uniform [$-\pi/6$, $\pi/6$] and [$-\pi/2$, $\pi/2$] distributions, respectively.

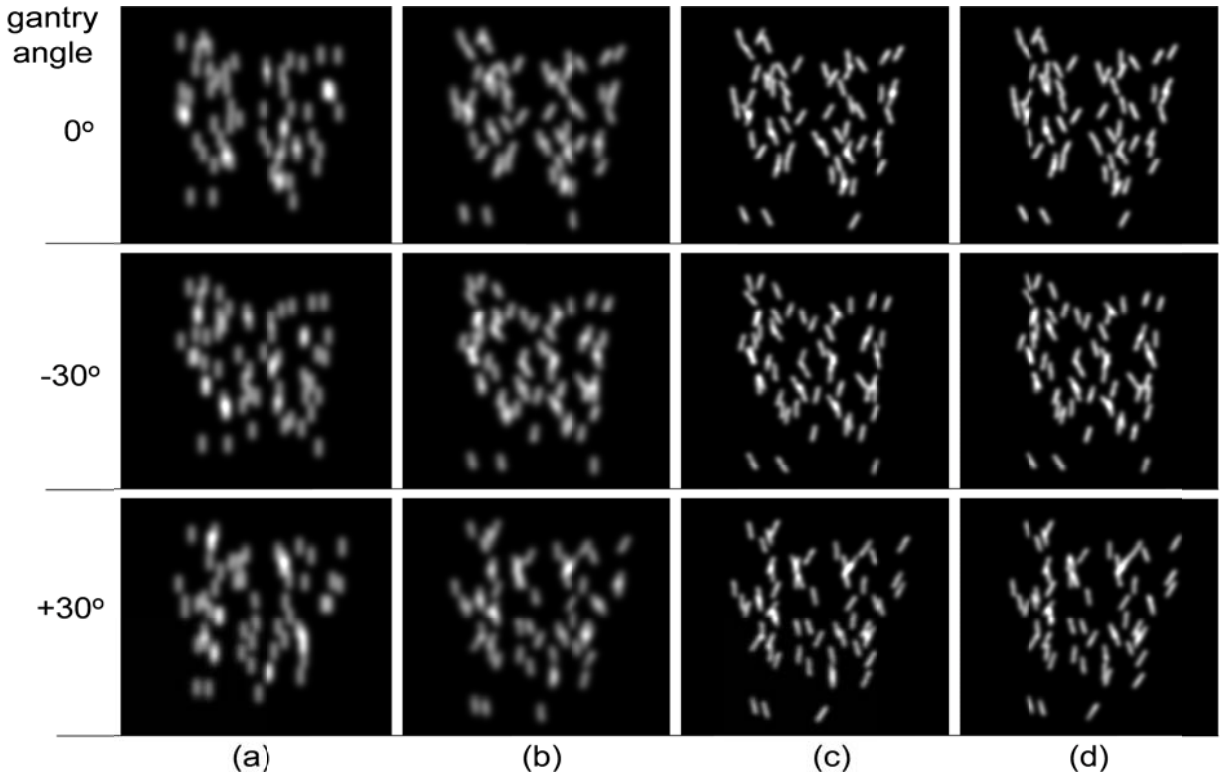


Fig.14. An illustration of the convergence process for a 60 seed simulated implant, (a) initial estimated seed configuration with "straight seeds" derived from a patient pre-plan, (b) computed images after convergence with $\sigma_1$ = 2.8 mm, (c) computed images after convergence with $\sigma_2$ = 1.8 mm and using poses (b) as the initial configuration; and (d) the true/synthetic measured images, where the rows represent different gantry angles. The gIFPM algorithm was able to reproduce orientation of each individual seed including overlapping clustered and highly migrated seeds.

Using these perturbed seed configurations, three synthetic measured projection images were computed for different CBCT gantry angles. The perturbed seed distribution represented the true configurations which we wished to determine. The source to detector distance was 150 cm and source to object distance was 100 cm with magnification factor of 3/2. The images were 288 × 288 pixels square and had a resolution of 0.388 mm/pixel. These images were submitted to the seed reconstruction process. When iteration starts with the initial estimate of the seed configuration for each trial it finds the new estimate of the 3D pose and the imaging viewpoint parameters, such as gantry angles until the computed projections match the measured ones.

Figure 14 shows an example of the iterative matching process for a simulated implant consisting of 60 seeds. The three projections have gantry angles of 0°, ±30°. The initial seed configuration was obtained from a patient's pre-planned implant geometry assuming the seed

axes to be parallel to the gantry axis. Comparison of the final computed images 14 (c) to the measured images (d) shows excellent agreement, including reproducing overlapping seed clusters which appear as brighter and/or extended seed group image features (paper II). The gIFPM algorithm successfully found seeds that were placed as far as 5 mm from their pre-planned positions. This case required 11 iterations in the 1st step (Gaussian width, $\sigma_1$ = 2.8 mm) with computation time of about 12 min/iteration and 4 iterations in the second step ($\sigma_2$ = 1.8 mm), with computation time of about 16 min/iteration on a 1 GHz processor (computation time depended upon number of seeds used in the implants, i.e., the number of free parameters to optimize in each iteration).

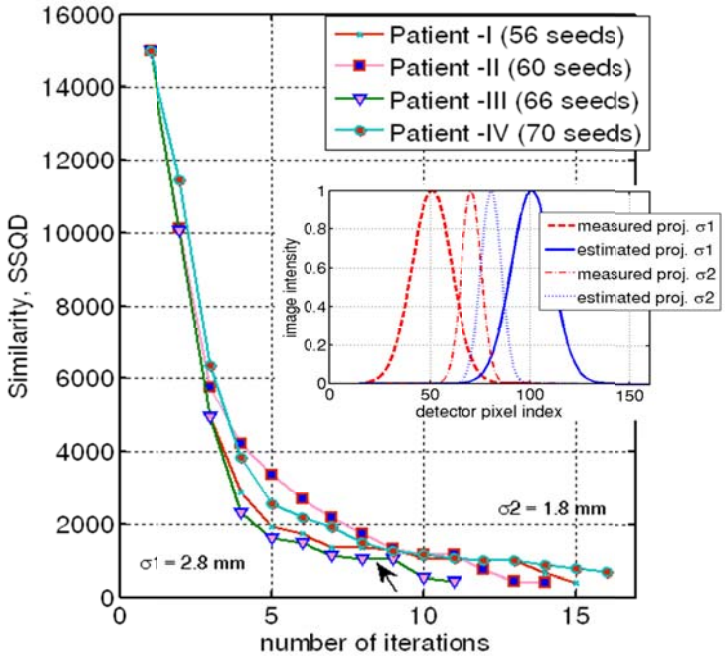


Fig.15. The similarity metric score vs. iteration number for the two step gIFPM algorithm for the four simulated patient cases: 56, 60, 66, and 70 seed configurations. The transition from larger to smaller blurring for the 66 seed configuration is shown by the black arrow. The one-dimensional image-intensity profiles in the inset illustrate the difference in capture range for the two blurring levels.

Figure 15 shows the convergence of the objective function score for the four simulated patient implants, where the black arrow indicates the plateau regions of the similarity when switching from first step to second step iterations. Similar transitions can be seen for the other patient cases convergence histories. Several experiments were performed to test the accuracy and robustness of the gIFPM algorithm, including arranging the seed geometry to simulate seed clusters and overlaps of increasing complexity in more than one or more projections (e.g., 2, 3 or seeds overlapping in one or more than one projection, etc.). Figures 14 and 16 illustrate

successful resolution of more than 4 seed clusters consisting of up to 5 seeds in the cluster on more than one projection. We found that gIFPM could accurately determine seed poses with clusters consisting of as many as five seeds. Table II summarizes the accuracy of gIFPM reconstructions for four simulated implants derived from patient cases. In all cases, the RMS seed position error was less than 0.7 mm and the maximum error did not exceed 1.5 mm. The RMS orientation errors were found to be about $5^o$ for the both angular coordinates.

**Table II.** Accuracy of gIFPM reconstructed poses for 4 simulated implants derived from patient pre-plans. The root-mean-square (RMS) value and standard deviation for the positional and orientation coordinates are reported. The maximum displacement (Max. error) of the seed position is also reported.

| Patient # (No. of seeds) | Gantry angles ($^o$) | Total no. of iterations | gIFPM vs. true seed pose | | | |
|---|---|---|---|---|---|---|
| | | | RMS error in seed position (mm) | Max. error (mm) | RMS error in seed orientation ($^o$) | |
| | | | | | $\theta$ | $\varphi$ |
| I (56) | 0<br>+20<br>-20 | 15 | 0.63 ± 0.45 | 1.32 | 4.4 ± 3.2 | 5.3 ± 3.1 |
| II (60) | 0<br>-30<br>+30 | 14 | 0.53 ± 0.43 | 1.19 | 3.9 ± 2.7 | 4.4 ± 3.8 |
| III (66)* | 0<br>-20<br>+20 | 11 | 0.68 ± 0.54 | 1.46 | 5.2 ± 5.7 | 5.8 ± 5.3 |
| IV (70) | 0<br>+30<br>-30 | 16 | 0.65 ± 0.52 | 1.38 | 6.0 ± 2.8 | 6.2 ± 3.2 |

* Two extra seeds in the pre-plan

Figure 16 illustrates the convergence process for Table II Case III in which ambiguities are created by incomplete (two seeds missing from the true implant but present in estimate) and excessive (one additional seed-like artifact in the measured projections with no counterpart in the computed images) data. The difference images in Figure 16 (d) shows that in both cases the two-step iterative convergence process closely reproduces the measured seed projections (paper II). However, the gIFPM algorithm converged robustly to an optimal solution of the seed configuration that was only slightly perturbed in the region adjacent to the additional or missing seed images. Since difference images readily identify the additional and/or missing seeds, gIFPM could be rerun with a modified initial configuration having the correct number seeds and/or seed-like objects which would slightly improve reconstruction accuracy.

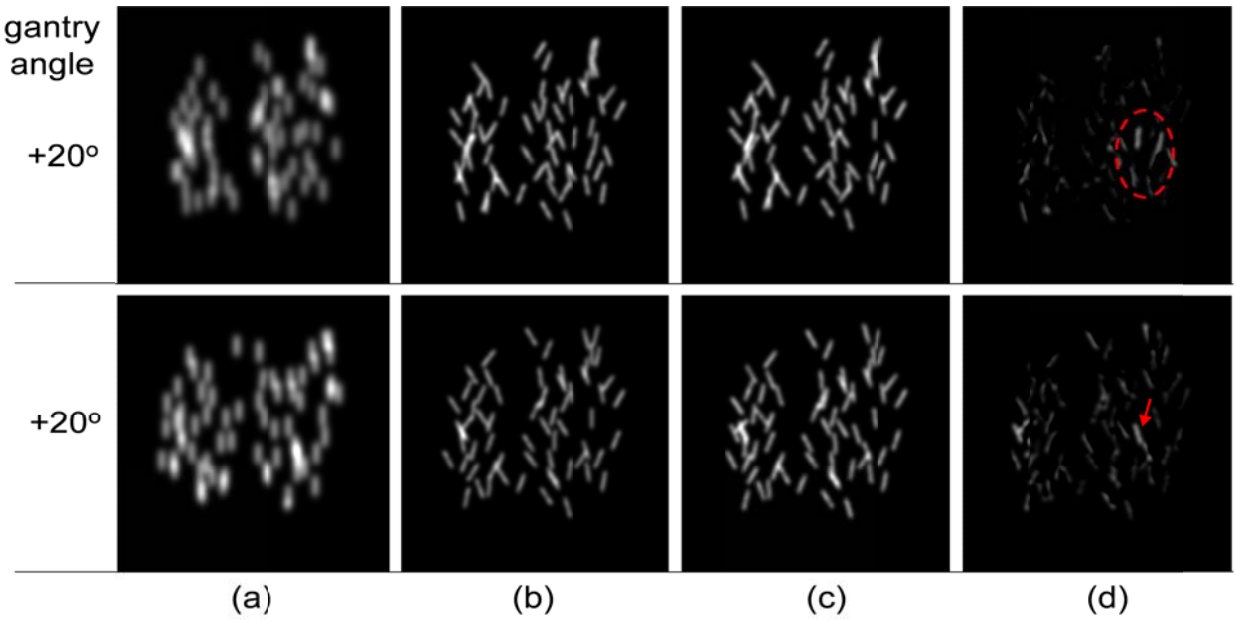


Fig.16. Illustration of gIFPM seed reconstruction for simulated case III in Table I for a single projection. In the first row (+20°), 66 seeds are present in the simulated implant derived from the preplan but 68 are assumed in the initial seed configuration, (a) with seed axes parallel to the gantry axis. In the second row (+20°), 66 seeds are present both in the initial estimated configuration and in the simulated implant along with an additional seed-like artifact which is present in the measured images, (a) initial estimate of the seed configuration, (b) computed images at final convergence, (c) the synthetic measured images corresponding to the "true" seed configuration, and (d) difference between images (b) and (c). The red arrow and ellipse in (d) indicates the extra seed(s) found by gIFPM at convergence.

## C.3 Validation via physical phantoms –integration to clinical practice

*Brachytherapy phantom design –a multi-configuration prostate seed phantom*

An in-house precision-machined phantom that realizes clinically realistic Model-6711 seed prostate implants with known positions (±0.1 mm accuracy) in each direction and orientations (±1$^{o}$ for θ and φ angles) was built [see Figure 17 (a) and (b)]. As the acrylic plates are interchangeable individual seed poses are adjustable and many different seed configurations can be realized. In this study, three clinically realistic brachytherapy seed configurations containing totals of 50, 72 and 76 seed datasets were realized on the phantom. For the 50 seed case, decayed Model 6711 $^{125}$I seeds obtained from Oncura Inc. were used. In that case, we modeled only 3 mm radio-graphically visible radio-opaque marker. For the remaining cases, machined stainless steel cylinders (4.5 mm long by 0.8 mm in diameter) were used.

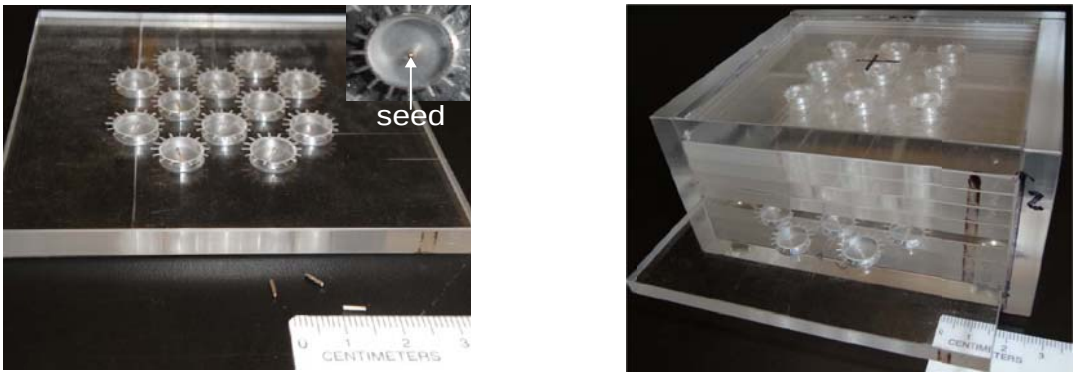


(a) (b)

Fig.17. Close-up photographs, (a) an acrylic slab of the phantom containing Model 6711 $^{125}$I seeds; where the polar angle θ is defined as the angle between implant axis and the major axis of the seed. It was assigned across the slab at different orientation for each seed (see inset). The azimuthal angle, φ was assigned by using the adjustable reference grid drawn for each seed in known orientation, and (b) multi-configuration precision-machined phantom assembly with all 8 replaceable slabs. This phantom was used to create different seed configurations to test the gIFPM algorithm seed localization accuracy in the clinical setting (see paper II for more detailed).

*Acquisition and processing of measured radiographic projections*

To experimentally validate this algorithm, the phantom was imaged on a Varian ACUITY imaging system which is used for performing image-guided brachytherapy insertions in our dedicated brachytherapy suite. CBCT images of the phantom were acquired for a complete gantry rotation around the phantom capturing approximately 660 projections through 360$^o$ using a Varian 4030CB flat panel detector. Three to ten radiographic projections at 5$^o$ to 10$^o$ angular intervals were selected from the full set CBCT x-ray projections between ±30$^o$ gantry angles. The choice of perspectives was based on maximizing visibility of the implanted seeds in the projections and avoiding excessively small parallaxes.

The image post-processing was performed as described earlier (see B.1 for more detailed) except the gIFPM method does not require transforming cylindrical seed images into point-like landmarks. Instead, we matched elongated line-seed features in the 2D images including overlapping seed clusters. This avoids a major difficulty encountered by back-projection methods: resolving seed clusters and isolating each seed centroid before reconstruction. The binary images were then convolved with the same 2D Gaussian blurring function that was used for the computed projection to create diffuse elongated seed lines with a known intensity distribution. This produces smoothly-varying grayscale image gradients that can be calculated

analytically in the computed projections to guide towards minimization of the objective function, SSQD and speed up the convergence of the matching process. An example case of image post-processing is shown in Figure 18.

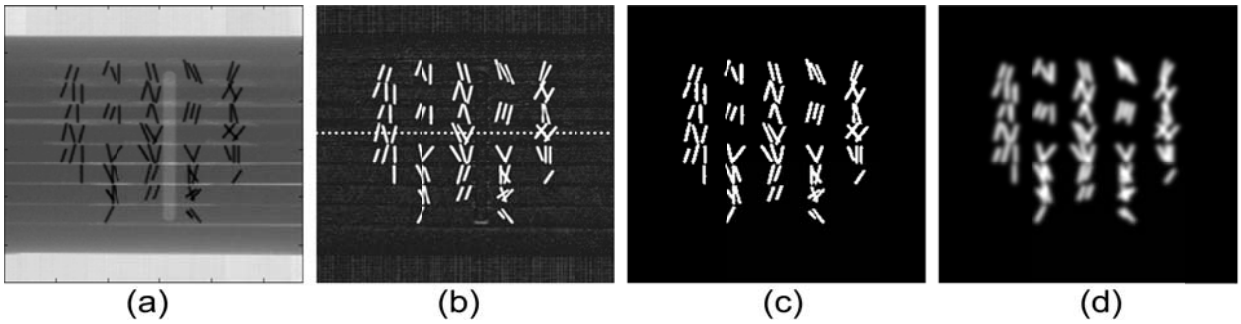


Fig.18. An example case of the image post-processing of the projection images obtained from the Varian 4030CB digital simulator, (a) raw projection image, (b) filtered image, (c) binary seed only bitmap image, and (d) blurred grayscale image using the gIFPM algorithm for 76 seed phantom datasets.

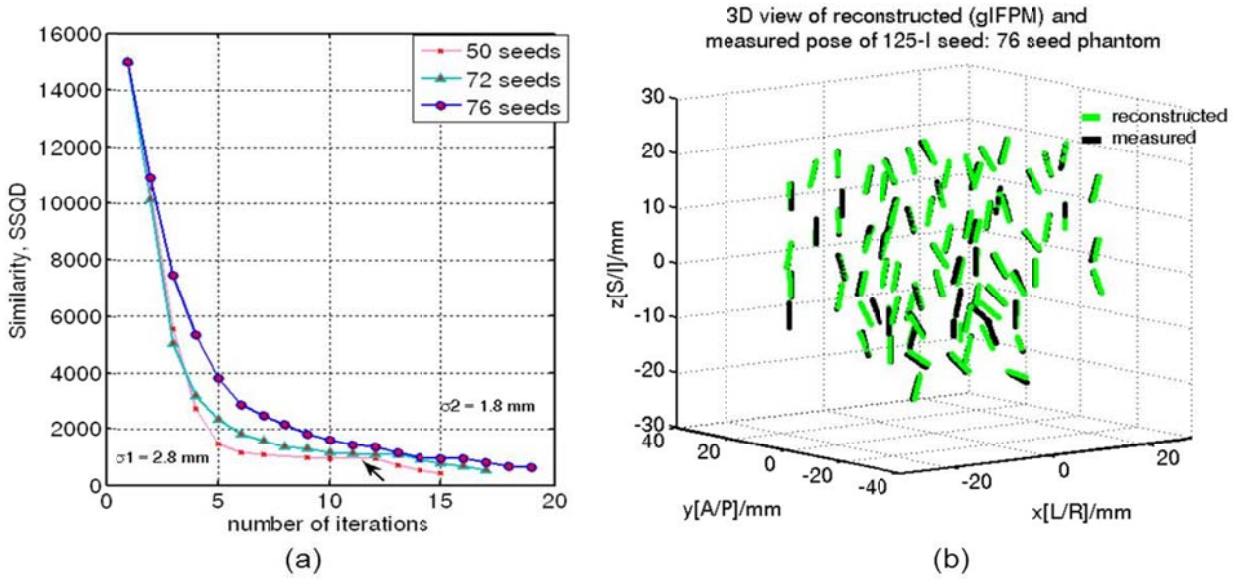


Fig.19. (a) Similarity metric score vs. iteration number for the two-step gIFPM algorithm for the three example physical phantom seed configurations. The transition from larger to smaller blurring filter for the 50 seed configuration is highlighted by the black arrow, and (b) superposition of measured seed images (black line seeds) with automatically detected seed poses (green line seeds) for 76 seed phantom datasets.

Figure 19 (a) shows the convergence of the objective function for the three example seed configurations derived from the same phantom, where the black arrow indicates the plateau region where the algorithm transition from the larger to smaller Gaussian width. Figure 19 (b) shows seed-by-seed superposition of the reconstructed (green) and measured (black) showing

near coincidence achieved by 3D-to-2D image registration and seed reconstruction in a unified method.

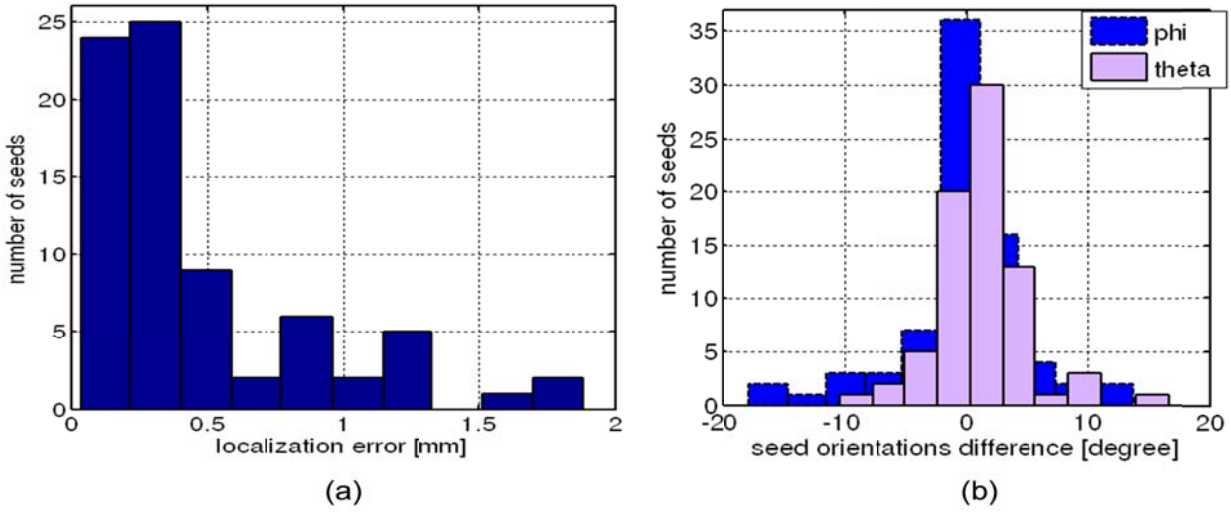


Fig.20. Histograms of the seed localization error for the 76 seed phantom datasets, (a) positional, and (b) orientations error.

The seed reconstruction error was computed by directly comparing the computed seed coordinates with the known seed poses obtained from the precision-machined phantoms. We performed ad hoc post-reconstruction matching by finding, for each ground truth 3D seed pose, the nearest reconstructed seed pose that minimizes the 3D Euclidean distance and angular variables between computed (gIFPM) and physically measured seed pose. For the 76 seed phantom case, from one-to-one correspondence between the two sets of seed coordinates the RMS error was (0.78 ± 0.57) mm. The $\theta$ and $\varphi$ angle distributions when using three projections were found to be (5.7 ± 4.9)° and (6.0 ± 4.1)°, respectively. The seed reconstruction error is reported in the histograms in Figure 20 (a) where it shows that 97% of the reconstructed seed positions are within 1.5 mm from the measured seed locations, (b) shows that greater than 95% of the reconstructed seed orientations are within $8^{o}$ from the measured seed orientations. This case required 15 iterations in the 1st step (Gaussian width, $\sigma_1 = 2.8$ mm) with computation time of about 18 min/iteration and 4 iterations in the second step ($\sigma_2 = 1.8$ mm) with computation time of about 22 min/iteration or more on a 1 GHz processor. Table III summarizes the accuracy of gIFPM reconstructions for three measured implants derived from the same phantom. With 6 projections these errors reduced by approximately a factor of $\sqrt{2}$ at the cost of doubling computation time.

**Table III.** Accuracy of seed poses deduced by the gIFPM algorithm for three seed configurations realized by our physical phantom and imaged on the VCU ACUITY system. The root-mean-square (RMS) value and standard deviation for the positional and orientation coordinates are reported while using 3 vs. 6 experimentally acquired projections. The maximum displacement (Max. error) of the seed position is also reported.

| No. of seeds | No. of projections | Total no. of iterations | gIFPM vs. true seed pose | | | |
|---|---|---|---|---|---|---|
| | | | RMS error in seed position (mm) | Max. error (mm) | RMS error in orientation ($^o$) | |
| | | | | | $\theta$ | $\varphi$ |
| 76** | 3 | 19 | 0.78 ± 0.57 | 1.88 | 5.7 ± 4.9 | 6.0 ± 4.1 |
| | 6 | 21 | 0.67 ± 0.47 | 1.56 | 4.6 ± 3.6 | 4.5 ± 3.3 |
| 72** | 3 | 17 | 0.72 ± 0.48 | 1.74 | 5.0 ± 3.8 | 5.7 ± 3.3 |
| | 6 | 18 | 0.56 ± 0.52 | 1.37 | 3.8 ± 2.9 | 4.2 ± 3.7 |
| 50* | 3 | 15 | 0.75 ± 0.46 | 1.78 | 4.9 ± 3.3 | 5.3 ± 3.8 |
| | 6 | 16 | 0.59 ± 0.42 | 1.44 | 3.2 ± 2.8 | 4.3 ± 2.9 |

** Line seed made up of stainless steel (4.5 mm long and 0.8 mm in diameter)
* Actual Model 6711 $^{125}$I dummy seed (3.0 mm × 0.5 mm radio-opaque marker)

An example of the reconstructed seed configurations projected onto imaging planes is presented in Figure 21. For all non-clustered computed seed images, we empirically calculated the seed centroids (center of mass of each seed region) and orientation angles (angle between the x-axis and the major axis of each seed) in each 2D image plane and compared with those obtained from the measured seed images at convergence. The residual 2D registration errors were 0.69 ± 0.55 mm (+5 degree), 0.83 ± 0.56 mm (-20 degree), and 0.79 ± 0.58 mm (+20 degree) for nearest-neighbor displacement and 5.4 ± 3.9° (+5 degree), 6.9 ± 6.2° (-20 degree), and 6.7 ± 5.1° (+20 degree), respectively for polar angle (paper II). This indicated very good agreement between measured and computed seed images.

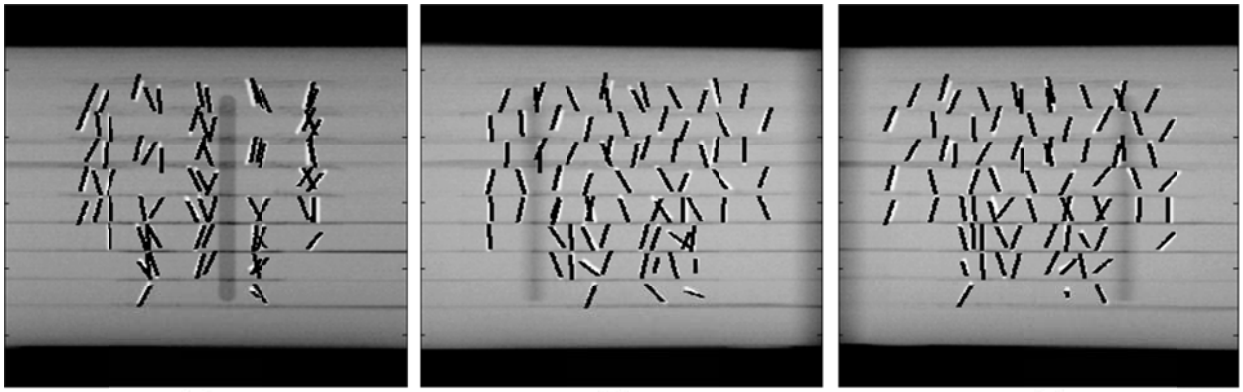


Fig.21. Superposition of measured (white) and computed (black) line seed images projected on the detector planes for gantry angles of (a) $+5^{o}$, (b) $-20^{o}$, and (c) $+20^{o}$ for 76 seed phantom configuration. While many computed seeds coincided exactly with the measured ones, a few still reveal small discrepancies.

A novel algorithm for accurately recovering 3D pose of implanted brachytherapy seeds from as few as 3 projections was developed. The generalized IFPM algorithm provides better than 0.7mm/$6^{o}$ accuracy in reconstructing the 3D pose of brachytherapy seeds when tested on 50 to 76 seed phantom datasets using CBCT x-ray projections. The test trials converged in 10 to 20 iterations when using two-step blurring and always arrived at the global minimum. By comparing overall image content rather than individual seed poses, the gIFPM method does not face a correspondence problem between seed identities in the several images as standard BP methods. It corrects for uncertainties in the measured projection geometry by adjusting the imaging system viewpoint.

As of now, subtracting the measured images from the computed images at convergence, one can locate extra-seed(s) in the implant. As future work, one could consider automatically correcting over- and under-counted seed(s) in the implant and re-running the reconstruction process to obtain the optimal match. More extensive investigation of the initial estimate of the seed configurations using TRUS pre-plan geometry along with the post-implant seed arrangement of the model 6711 $^{125}$I seed patient' need to be performed to further validate this algorithm. This iterative pose search method has not been fully optimized for speed. Improving the computation efficiency will involve not only the code development but also investigation of other gradient search algorithms (such as conjugate gradient, Newton's method, etc.) which is also an area of future development.

The results presented in this part of the research demonstrate that the gIFPM algorithm works well for seeds with radio-opaque markers having an aspect ratio equal to 6:1or larger (characteristic of the Model 6711 $^{125}$I source). Other $^{125}$I brachytherapy seeds satisfying this constraint include the selectSeed[49], (Amersham 6733 seed, IsoAid Advantage, DraxImage LS-1, Source Tech Medical STM1251)[50], Model symmetra[51], Model 9011[52], and Best Model 2301[53] sources allowing gIFPM estimate individual seed orientations as well as locations. Extension of this IFPM approach to localize larger metal objects in the brachytherapy treatment, for example ICB applicators (tandem and colpostats) of arbitrary-shaped, is being investigated as further generalization of this method (paper III). *By incorporating five degrees of freedom search capability, the IFPM approach (which does not require matching of corresponding images on each projection) can be easily extended to localization of cylindrically symmetric objects* (e.g. implanted fiducial markers or brachytherapy needles, whose aspect ratios are 6:1 or larger).

*Innovation/Impact*

gIFPM is a novel approach which is able to accurately reconstruct individual seed orientation as well as position, thereby permitting more accurate Monte Carlo-based or 2D TG-43 report[47] dose calculations to be performed. In addition, generalized IFPM is more robust and tolerant of missing data than BP methods and has the potential to make intraoperative dose reconstruction more feasible. Post-implant dosimetry performed four weeks after implant may now be supplemented by intraoperative dose reconstruction via CBCT to provide more immediate dosimetric feedback and assessment via gIFPM seed localization from 2D radiographic projections.

Another potential application could be improvement of CBCT image quality for the intra/postoperative brachytherapy patient's images. Accurate identification of the metal seed boundary and its orientation in the sinogram projections is very useful for suppressing metal streaking artifacts by re-projecting each metal seed boundary onto the sinogram so that the missing soft-tissue information can be recovered by interpolation from the surrounding soft-tissue image texture (see section B.4 for more detailed). Reconstruction of CBCT images with corrected (i.e., removed seeds) sinogram projections can then be performed.

# D LOCALIZING INTRACAVITARY BRACHYTHERAPY APPLICAOTRS VIA GENERALIZED IFPM ALGORITHM –applicator models

The IFPM algorithm[75-77] was further generalized to localize 3D pose of non-cylindrically symmetric rigid objects, such as intracavitary brachytherapy (ICB) applicators. Because of the non-rotational symmetry of the arbitrarily-shaped ICB applicators, we must extend our 5-parameter pose-search approach to 6-parameter applicator models which is needed to completely characterize the ICB applicators. Starting with an initial estimate of the applicator poses, this 6-parameter expanded applicator-model finds the set of applicator pose parameters that minimizes the pixel-by-pixel sum of the square intensity difference (SSQD) between blurred computed and measured auto-segmented projections of the applicators. Then the three positional $(x, y, z)$ and three orientations $(\alpha, \beta, \gamma)$ coordinates of each applicator model are independently adjusted in an iterative search process until the computed projections optimally match the measured images. See algorithm workflow in appendix 2.

The main aim of this study was to present a novel method for localizing the 3D pose of radio-opaque objects of known but arbitrarily shape from a small set of 2D x-ray projections, in support of intraoperative brachytherapy planning. The applicator model is a mesh of discrete points derived from a complex combinatorial geometric (CCG) modeling[58] of the actual applicator. Numerical simulations of clinically realistic ICB configurations were performed to demonstrate the proof of concept. Actual intrauterine tandem and bilateral colpostats images obtained from the ACUITY imaging system in our brachytherapy imaging suite were used to experimentally validate this algorithm. The details of this research are accepted for publication in *Medical Physics,* which is included as paper III.[78]

## D.1 Description of Fletcher-Weeks applicator

A low dose-rate (LDR) manual afterloading system using $^{137}Cs$ sources loaded into Weeks[57] CT-compatible Fletcher-Suit applicator [see Figure 22] was used in this study. The applicators consist of thin-walled central tandem and aluminum colpostats. It contains retractable tungsten-alloy shields. The main purpose of using retractable shields is two-fold. First, it reduces

the dose delivered to bladder and rectum (photons emitted by the source toward the rectum and bladder are obliquely filtered) and second, it produces relatively artifact-free CT images showing the implant location relative to the pelvic soft-tissue structures (only the thin-walled aluminum applicator casing was present in the CT studies). During an intracavitary procedure, the applicators as shown in Figure 22 without radioactive sources or tungsten shields are inserted in the patient. After imaging the applicator system, the radioactive sources along with tungsten shields are afterloaded into the applicator through the channels in the colpostats and tandem handles and treats the patient until the prescribed dose is delivered.

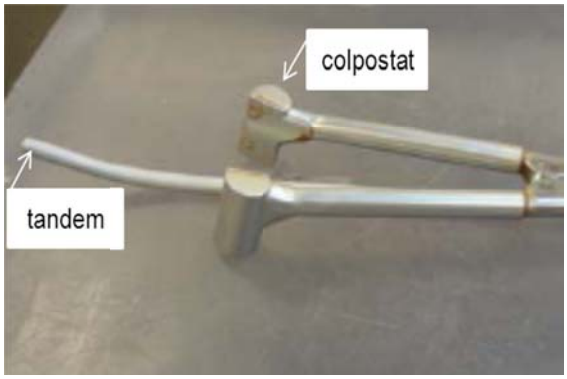


Fig.22. ICB applicator system used to treat locally advanced cervical cancer

## D.2 Origin and features of PTRAN geometric modeling system

The PTRAN Monte Carlo photon-transport code[58, 60, 61] was used to model arbitrary-shape ICB applicators. The code, initially created for dosimetry applications in brachytherapy, was adapted to the problem of computing kilovoltage radiographic projections of the ICB applicators. The photon transport model includes photoelectric absorption with production of fluorescent photons, Compton scattering including electron binding effects, coherent scattering and production of bremsstrahlung radiations. Many different estimators and post-processing options are supported. Given a completed geometric model, the code package supports point and segment classification as well as advanced ray-racing through the applicator components.

The volume based CCG modeling code[58] was used to obtain the initial estimate of the 3D applicator models (i.e., mathematical representation of the applicator models including internal structure as well as outer surface). PTRAN uses set theoretic definitions of region boundary,

interior, and exterior, and complex regions as set-theoretic unions, intersections and differences of the complex regions (i.e., mathematically defined geometric objects). Each component of the complex applicator region in a 3D model was characterized by its position, orientation, shape and size (paper III). These parameters were extracted from the micrometer measurements and orthogonal radiographs of the complicated applicators.[60, 61] Such complex modeling of the applicator geometry is essential to obtain partial transmission through the applicator components and to obtain more accurate Monte Carlo dose distributions.

## D.3 Geometric modeling of Fletcher-Weeks applicator

A model of the CBCT projection geometry is made and positioned at *M* different locations and orientations specified by translation and rotation matrices for each projection. A phantom made up of uniform elliptical water sphere of volume 1100 $mm^3$ was modeled. After successful modeling of the applicator components in the 3D space as described above, 2D projection images were computed using CBCT projection geometry. As shown in Figures 23 (a), (b), and 24 (a), (b), (c) detailed 2D images of the 3D geometric models of each applicator component can be computed by applying advanced ray-tracing routine. The source-to-detector distance was 150 cm and the source-to-isocenter distance was 100 cm. The detector was 40 cm × 30 cm with a 1024 ×768 image size and pixel resolution of 0.388 mm each.

(a) (b)

Fig.23. CBCT projection images obtained from the PTRAN Monte Carlo ray-tracing routine, (a) central intrauterine tandem (with 42.44$^o$ curvature), and (b) left colpostat model, where the grayscale image background represent uniform elliptical water cylinder. The black line segments in the tandem clearly show the stepping source position at different dwell time. The line source position is also shown in the left colpostat. The image intensity values represent an arbitrary integer number assigned to each material component in the model (paper III).


Fig.24. Computed CBCT projection images of the bilateral colpostats and central intrauterine tandem, reproducing clinical LDR treatment arrangement when using merge code.[60] Any angle projection around 360$^{o}$ gantry rotation can be acquired, for example, in this case, (a) projection with -30$^{o}$, (b) projection with 0$^{o}$, and (c) projection with +30$^{o}$ gantry angle, respectively.

The PTRAN Monte Carlo-based ray-tracing approach successfully obtained partial transmission through the applicator components. However, as it is now, the major downside is the large computation time (several minutes) required to compute one single projection of the applicator geometry. Projection computation efficiency can be improved either using graphic processor unit (GPU) or some other fast DRR calculation scheme. For now, in order to overcome this difficulty, we have represented the entire applicator geometry by a fine mesh of discrete points (i.e., mathematical representation of the entire applicator) uniformly distributed over an Aluminum shell of an actual applicator that were derived from PTRAN voxelized geometric modeling. The voxelized applicator model was then integrated into the geometric forward projector (see algorithm workflow in appendix 2) for computing updated DRRs and iteratively matched with the measured projections.

### D.4 Adapting 5-parameter model objective function to 6-parameter pose search

Our generalized IFPM algorithm described in paper II can not accurately localize ICB applicators of arbitrary-shape. This is because of the non-cylindrical symmetry about the axis of rotation of the complex shape of the large ICB applicators. To solve this problem, we have further generalized our 5-parameter line-seed pose-search algorithm to 6-parameter applicator models to completely localize the ICB applicators in 3D space. The new generalized IFPM

algorithm requires six pose parameters to fully describe each of the N applicators $k = 1, \cdots, N$ (typically N = 3 for a tandem and bilateral colpostats) in the world coordinate system (WCS) which takes the isocenter of the imaging system as its origin and has X, Y, Z directions defined by the x axis is left-right, the y axis is anterior-posterior, and the z axis is superior-inferior direction, for a patient in supine position with feet pointing away from the gantry stand. For the *k-th* applicator model $\left(t_x, t_y, t_z, \alpha, \beta, \gamma\right)_k$ where, $\mathbf{t}_k = \left(t_x, t_y, t_z\right)_k$, denotes the WCS coordinates of the origin of *k-th* applicator's local coordinate system and the three Euler angles $\mathbf{\Theta}_k = \left(\alpha, \beta, \gamma\right)_k$ describe its orientation of this local coordinate system in WCS relative to CBCT isocenter around the *x*, *y*, *z* axes, respectively. Each applicator model is described by a fine mesh of $Q_k$ points: $\left\{\mathbf{r}\right\}_k = \left\{\mathbf{r}_{ik} \mid \mathbf{r}_{ik} \in A_k, i = 1, \cdots, Q_k\right\}$ derived from the CCG applicator model when $\mathbf{\Theta}_k = 0$ and $\mathbf{t}_k = 0$ as described above. Typically, a mesh of 1 × 1 × 1 $mm^3$ was used.

A model of the CBCT projection geometry was made and positioned at *M* locations and orientations (gantry angles for ACUITY) specified by translation and rotation matrices for each image viewpoint. In the extrinsic detector model, the orientation of each isocentric projection in the world coordinate frame was defined by the angles $\left(\varphi, \psi, \eta\right)$ which describe rotations of the detector image plane around the *x*, *y*, *z* axes, respectively. After this, the mathematical representations of the actual applicator models were positioned at a simulator couch relative to the CBCT isocenter (aligning along the *z*-direction) by defining its translations and rotations. The detector model was parameterized by describing its magnification, image center, image size and pixel resolution. The source to isocenter and isocenter to the detector distances were denoted by S and D, respectively. The parameterized 3D applicator model was then forward projected (geometric projection) on the 2D detector planes using CBCT projection geometry and updated iteratively to match with the measured projection images.

In this approach, each applicator model moves (rotates and translates) independent to the others in the 3D space, computes new projections at different gantry angles and then iteratively match with the measured projections until the SSQD converges. In this way, the voxelized 3D

geometric model of arbitrary shape is integrated into the forward projection matching method for computing the 2D projection images of the 3D ICB applicators geometry, iteratively (paper III).

*Similarity metric and gradient search*

The overall similarity metric, SSQD is the total of the pixel-by-pixel sum of the squared intensity differences for all *M* blurred computed, $I_c\left(u,v\,|\,\{\mathbf{r}_k,\boldsymbol{\Theta}_k\},\sigma,\eta\right)$ and the experimentally acquired (measured) $I_m\left(u,v\,|\,\sigma,\eta\right)$ applicator image pairs (paper III),

$$SSQD\left(\{\mathbf{r}_k,\boldsymbol{\Theta}_k\}\,|\,\sigma,\eta\right)=\sum_{\eta}\sum_{u,v}\left[I_c\left(u,v\,|\,\{\mathbf{r}_k,\boldsymbol{\Theta}_k\},\sigma,\eta\right)-I_m\left(u,v\,|\,\sigma,\eta\right)\right]^2 \tag{4}$$

The initial pose parameters $\{\mathbf{r}_k,\boldsymbol{\Theta}_k\}$ of each applicator were iterated by simultaneously adjusting 3D applicator pose while projecting computed updated image $I_c\left(u,v\,|\,\{\mathbf{r}_k,\boldsymbol{\Theta}_k\},\sigma,\eta\right)$ for each gantry angle $\eta$ and re-evaluating the objective function, Equation (4). The pose updates were calculated from the first derivatives of SSQD with respect to each degree of freedom. The Gaussian blurring used in the projection images provides analytical grayscale image gradient that extended away from the applicator components. The blurring creates a "source attractive" potential well around each applicator that extended its tail beyond the applicator itself. It had the effects of attracting applicators to each other between the measured and computed projection images and accelerating the convergence of the iterative minimization search.

The nonlinear gradient of the similarity, SSQD with respect to 3 positional and 3 orientations degrees of freedom were computed analytically; for example, with respect to *x*-coordinate,

$$\partial\left(SSQD\right)/\partial x_{i,k}=2\sum_{\eta}\left(\sum_{u,v}\left[I_c\left(u,v\,|\,\{\mathbf{r}_k,\boldsymbol{\Theta}_k\},\sigma,\eta\right)-I_m\left(u,v\,|\,\sigma,\eta\right)\right]\partial I_c\left(u,v\,|\,\{\mathbf{r}_k,\boldsymbol{\Theta}_k\},\sigma,\eta\right)/\partial x_{i,k}\right) \tag{5}$$

and similarly for the remaining pose coordinates. The grayscale image gradients, $\left(i.e.,\ \partial I_c\left(u,v\,|\,\{\mathbf{r}_k,\boldsymbol{\Theta}_k\},\sigma,\eta\right)/\partial x_{i,k}\ \text{and so on}\right)$ with respect to (x, y, z) positions and (α, β, γ) orientations coordinates were computed from the blurred computed images for each applicator model and obtained the best (mean) gradients. That is, to provide a single derivative with respect

to each degree of freedom for updating $\{\mathbf{r}_k, \boldsymbol{\Theta}_k\}$, $\partial I_c(u,v)/\partial x_k$ was averaged over all pixels $(u,v)$ contained within the shadow of the *k-th* arbitrary-shape applicator model (i.e., $\overline{\partial I_c(u,v)/\partial x_k}$ and so on). The applicator components such as a tandem and bilateral colpostats were treated as an individual rigid object, making sure that each applicator had 6 degrees of freedom in 3D space. Detailed derivations of gradient calculation can be found in the appendix (paper III). The same steepest-descent gradient search method as described in section C.1 was used for updating the pose parameters in the iterative matching process.

## D.5 Validation via simulated applicators geometries

*Intrauterine tandem localization*

The numerical simulation studies have been performed to demonstrate the reproducibility of the known 3D pose of the intrauterine tandem. The 3D model of the intrauterine tandem was obtained from the PTRAN CCG modeling when $\boldsymbol{\Theta}_k = 0$ and $\mathbf{t}_k = 0$ described in the previous section. After obtaining the 3D model of the applicator, user specified pose parameters for each applicator component relative to CBCT isocenter and the models were aligned along the z-direction. This was the true pose of the applicator model which we wished to determine. Using this applicator model, three true/ synthetic measured projection images were computed using the CBCT projection geometry at different gantry angles. The projected applicator on the imaging plane was masked to create the binary bitmap images, making sure image intensity = 0 in the background and intensity = 1 over the area of the projected applicator. The 3D applicator model was shifted by a displacement ±2.5 mm in each coordinate axis and rotated ±8$^o$ around each rotation axis. This was our initial estimate. Both the true/ synthetic measured and computed images were blurred using 2D Gaussian blurring function with a known intensity distribution. This produces smoothly-varying grayscale image gradient that can be calculated analytically in the computed projections to guide towards minimization of the objective function. The source to detector distance was 150 cm and source to object distance was 100 cm with magnification factor of 3/2. The images were 576 × 576 pixels square and had a pixel resolution of 0.388 mm.

The true/synthetic measured images were submitted to the applicator reconstruction process. When iteration starts with the initial estimate of the applicator model for each trial it finds the new estimate of the 3D pose parameters until the computed projections match the measured ones.

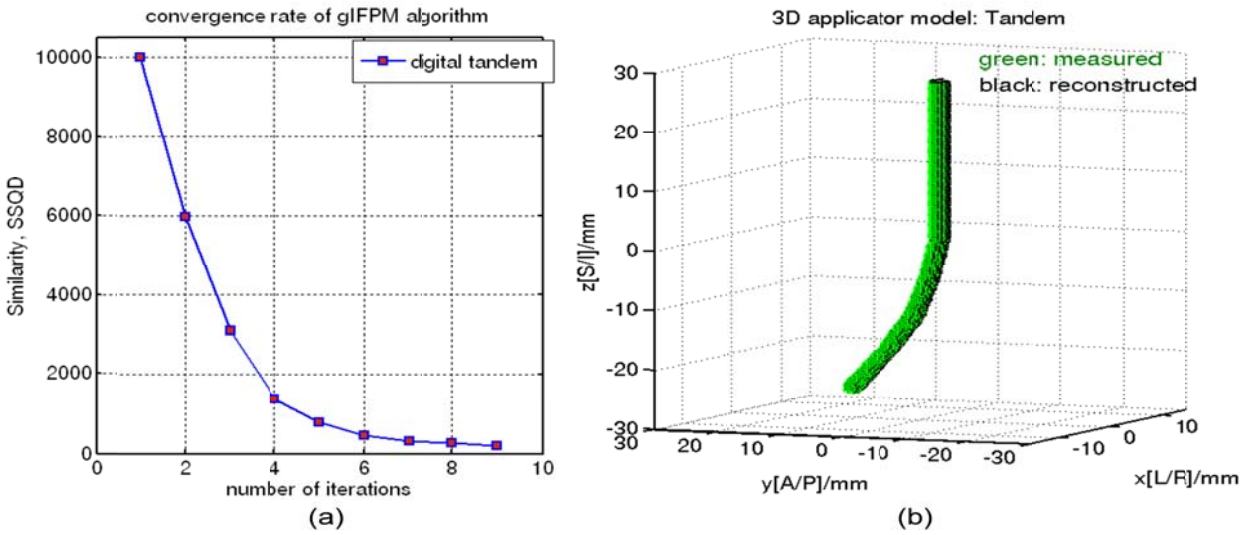


Fig.25. The similarity metric score vs. iteration number of gIFPM algorithm for a synthetic measured digital-tandem datasets, (b) point-by-point superposition of the reconstructed tandem (black) with synthetic measured tandem (green); showing near coincidence achieved by 3D-to-2D applicator registration.

In Figure 25 we show convergence rate history for the digital-tandem for one of the trial. In this case the convergence was reached in 9 iterations with a total computation time of 40 second on a 1 GHz processor. All test trials converged in 8 to 12 iterations. The voxel-by-voxel coordinates of the reconstructed tandem (black) were overlaid with the true/synthetic measured tandem (green), demonstrating the overlap achieved by the applicator localization method. The mean positional and angular error was found to be (0.28, 0.3, 0.37) mm, and (0.9, 0.8, 1.0)$^{o}$, respectively (paper III).

*Combined applicators –Intrauterine tandem and bilateral colpostats*

The 3D models of the applicator components (tandem, right and left colpostats) were obtained from the PTRAN combinatorial geometric modeling as described earlier. The tandem and colpostats were placed so the tandem bi-sects the colpostats on the lateral view. The tandem fell midway between the colpostats and parallel to the body axis on AP view. The separations between colpostats were 25 mm, 35 mm and 45 mm for each trial, respectively. This was the true

pose of the applicator models which we wished to determine. Using these applicator models, three true/ synthetic measured projection images were computed using the CBCT projection geometry at different gantry angles.

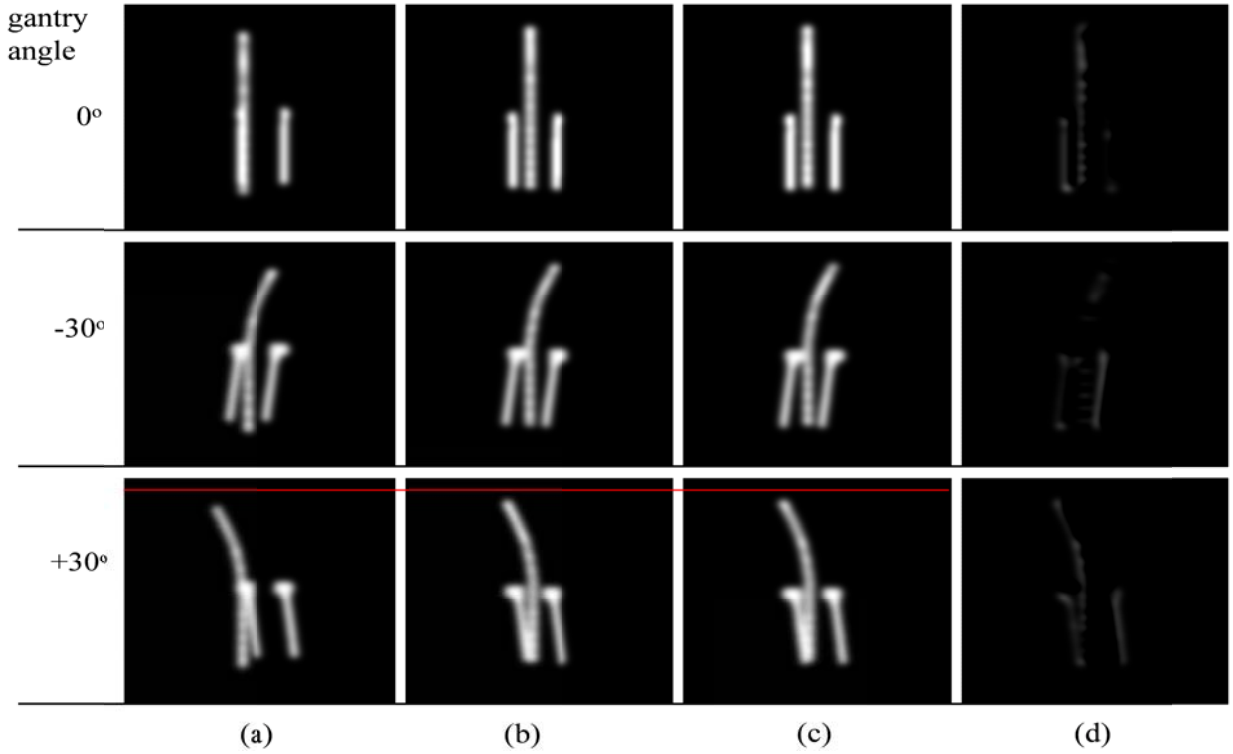


Fig.26. An illustration of the iterative convergence process for a simulated implant consisting of tandem and bilateral colpostats for a 25 mm colpostats separation. Column (a) initial estimate of the applicator configuration, (b) computed images at convergence, (c) the true/synthetic measured images, and (d) the difference between (b) and (c), where the rows represents different gantry angles. The red line in the 3rd row indicates that the reference of the initial estimate with respect to the measured images in part (c). The generalized IFPM algorithm was able to reproduce each applicator pose, as well as overlapping components.

The projected applicators on the imaging plane were masked to create the binary bitmap images. Each 3D applicator model was shifted by a displacement ±2.5 mm in each coordinate axis and rotated ±8° around each rotation axis. This was our initial estimate of the applicator configurations. Both the true/ synthetic measured and computed images were blurred using 2D Gaussian blurring as described above. For each trial, the iteration took the initial estimate of applicator poses and then the 3D pose parameters of each applicator model were independently adjusted until the computed projections matched with the measured ones.

Figure 26 shows an example of the iterative matching process for a simulated implant consisting of full ICB applicators (intrauterine tandem and bilateral colpostats). The three

projections have gantry angles of 0°, ±30°. The small difference in Figure 26 (d) shows very good agreement between the measured and computed binary images at convergence, including reproducing overlapping applicator components. Figure 27 shows convergence rate histories for the combined applicator geometries. All test trials converged in 10 to 12 iterations with a total computation time of about 1 minute on a 1 GHz processor.

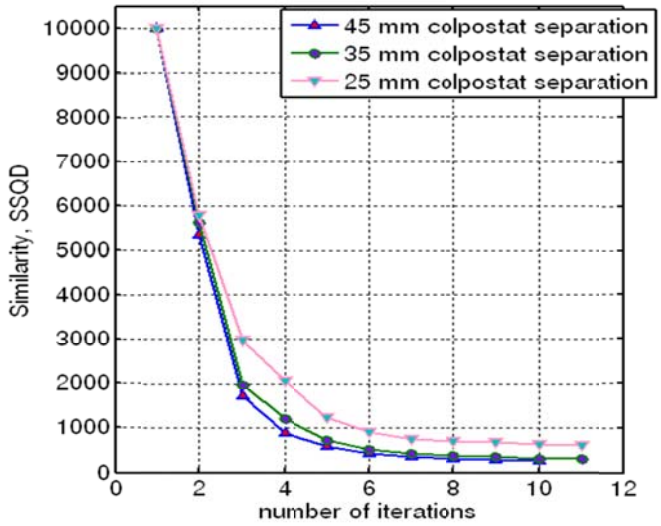


Fig.27. Convergence matching rate of generalized IFPM algorithm for the three simulated full ICB applicator configurations.

The comparison is summarized for all three simulated cases in Table IV. In all trials the difference errors were less than 1 mm and 2° for each of the positional and angular coordinates, respectively (paper III).

**Table IV.** Accuracy of gIFPM reconstructed poses for 3 simulated full applicator system configurations. The difference for the each applicator component position and orientation coordinates is reported.

| Separation between the colpostats (mm) | Image viewpoint used (°) | Applicator components | gIFPM vs. true applicator pose | | | | | |
|---|---|---|---|---|---|---|---|---|
| | | | Difference in applicator position (mm) | | | Difference in applicator orientation (°) | | |
| | | | Δx | Δy | Δz | Δα | Δβ | Δγ |
| 25 | 0, -30, +30 | Tandem | 0.41 | 0.59 | -0.38 | -0.98 | 0.78 | 1.86 |
| | | R. colpostats | 0.18 | -0.56 | 0.48 | 2.03 | 1.71 | -0.89 |
| | | L. colpostats | -0.38 | -0.48 | 0.61 | -0.85 | 2.04 | 1.95 |
| 35 | 0, +20, -20 | Tandem | 0.15 | -0.37 | 0.46 | 0.89 | 0.95 | -0.86 |
| | | R. colpostats | -0.32 | -0.15 | 0.36 | 1.56 | -0.74 | 1.62 |
| | | L. colpostats | -0.28 | 0.54 | -0.51 | -0.87 | 1.42 | 0.73 |
| 45 | 0, -30, +30 | Tandem | -0.18 | 0.27 | 0.34 | -0.86 | -0.64 | -0.72 |
| | | R. colpostats | 0.14 | 0.18 | -0.35 | 0.46 | 0.58 | 0.65 |
| | | L. colpostats | -0.20 | 0.34 | 0.52 | 0.87 | 1.06 | -0.56 |

Several experiments were performed using different gantry angle combinations as well as different initial starting configurations of the applicators in the course of this study. Theoretically, one should expect SSQD = 0 at the convergence, i.e., all computed applicators images should exactly match with those measured. However, from Figure 27, for the combined-applicators geometries, it is evident that the SSQD did not exactly converge to zero (i.e. less than 3% difference between measured and computed applicator images), showing less than optimal convergence (i.e., trapping in local minima). That means if the initial estimate of the applicators configuration is far apart from the measured configuration there is a chance of less than optimal matching. Finite width of the detector pixel size may also affect the convergence rate of gIFPM algorithm (in principle the larger the pixel size, the less than optimal the convergence).

## D.6 Validation via actual applicators geometry –integration to clinical practice

*Acquisition and processing of radiographic projections*

The projection images of the actual applicators (tandem and bilateral colpostats) were obtained from the ACUITY CBCT digital-simulator used for image-guided brachytherapy procedures in our institute. The detector was 40 cm × 30 cm with a 1024 × 768 image size and pixel resolution of 0.388mm/pixel. The image post-processing involved a) cropping the images to 576 × 576 pixels square; b) normalizing the image intensity by finding its maximum and minimum values in the image; c) morphological top-hat-filtering to suppress the background, and d) automatic thresholding using the 3-standard deviation value of the pixel intensity histogram to create binary applicator only images in each projection in order to separate the applicators from the background. This produced binary bitmap images with intensity = 0 in the background and intensity = 1 over the area of the projected applicator. One example case of some of the major steps of the image post-processing is shown in Figure 28. The binary images were then convolved with a 2D Gaussian blurring function to use by gIFPM algorithm.

The initial estimates of the applicators configurations were derived as described in section D.5 above. For each trial, the separations between the colpostats were 30 mm, 40 mm, and 50 mm, respectively.

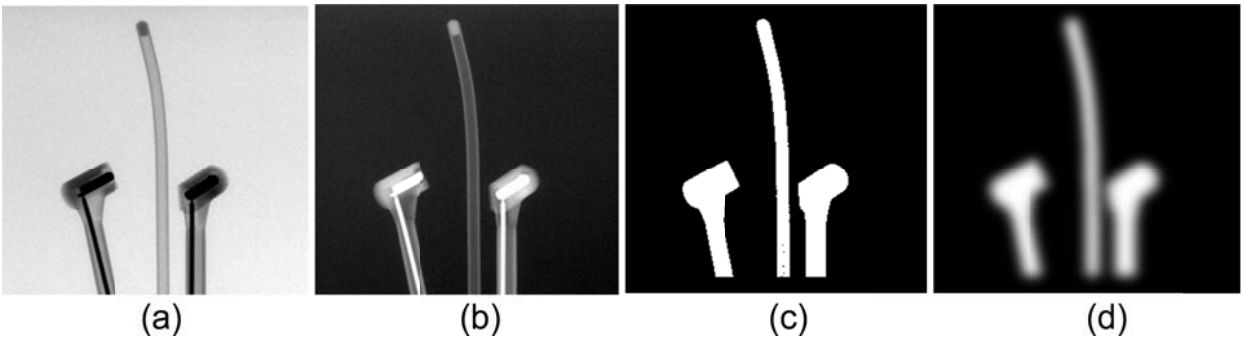


Fig.28. One image viewpoint showing the image post-processing steps of the experimentally measured applicator components, a) original raw image, b) filtered image, c) applicator only binary image and d) blurred applicators image with known intensity distribution used by generalized IFPM algorithm.

For the measured applicator images, there were no ground truth applicator coordinates. The applicator registration error was computed by re-projecting the gIFPM applicator poses at convergence onto the 2D image planes, overlying the computed and measured applicator projections, and calculating the nearest-neighbor positional difference between the measured and computed applicator positions in each image plane. An example of the automatically reconstructed applicator poses projected on the measured digital simulator images is presented in Figure 29.

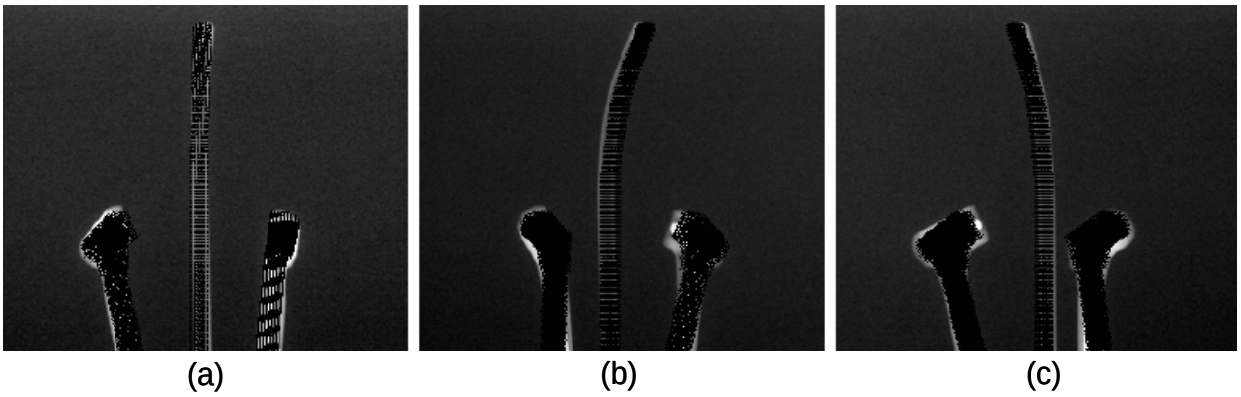


Fig.29. Superposition of experimentally acquired binary images (white) with automatically reconstructed applicators positions (black) projected onto the detector planes, (a) $0^o$ gantry angle, (b) $-30^o$ gantry angle, and (c) $+30^o$ gantry angle, respectively when using 40 mm colpostats separation. The residual 2D registration error was less than 1 mm for the intrauterine tandem and about 1.5 mm for the bilateral colpostats on each image plane.

From these images, we empirically calculated the residual 2D registration error between the computed and experimentally measured applicators image pairs at convergence (paper III). The

center of mass difference between measured and computed tandem for the entire tandem was used, while the center of mass difference between the measured and computed source center location for the bilateral colpostats was estimated.

**Table V.** The residual 2D registration error between computed and measured applicator projection in terms of 2D radial difference in each image plane. The center of mass difference between measured and computed tandem of the entire tandem at convergence is reported, whereas the center of mass of the difference between the measured and computed source position at convergence is empirically calculated for the right- and left colpostats.

| Separation between the measured colpostats (mm) | Applicator components | gIFPM vs. measured applicator position at convergence: residual 2D registration error (mm) | | |
|---|---|---|---|---|
| | | gantry = $0^o$ | gantry = $-30^o$ | gantry = $+30^o$ |
| 30 | Tandem | 0.88 | 1.12 | 1.16 |
| | R. colpostats | 0.93 | 1.88 | 1.57 |
| | L. colpostats | 1.25 | 1.75 | 1.93 |
| 40 | Tandem | 0.67 | 0.89 | 0.78 |
| | R. colpostats | 1.14 | 1.46 | 1.81 |
| | L. colpostats | 0.96 | 1.67 | 1.66 |
| 50 | Tandem | 0.58 | 0.91 | 0.75 |
| | R. colpostats | 0.87 | 1.46 | 1.42 |
| | L. colpostats | 0.72 | 1.58 | 1.54 |

Table V shows the residual 2D registration errors between the measured and computed applicator components in each image plane. In all cases, the majority of the 2D radial difference of the applicator registration error was about 1.5 mm or less and no error exceeded 2.0 mm in the detector plane. This indicated good agreement between measured and computed applicators projections. Several experiments were performed to test the accuracy and robustness of the gIFPM algorithm, starting with different initial estimates and gantry angle combinations. This novel algorithm is accurate, fast and completely automatic to localize radio-opaque applicators of arbitrary shape from measured 2D x-ray projections and has a potential for intraoperative brachytherapy planning.

To improve the accuracy of the applicator localization validation study, one could consider designing a precision-machined pelvic phantom that houses ICB applicators and test the gIFPM performance against a more rigorous ground truth. It is observed that the computed applicator poses at convergence vary to some extent (see section D.5 for detailed explanation), depending on the initial starting configuration, indicating less than optimal convergence, i.e., trapping in local minima. The dependence of convergence rate and accuracy on the initial

estimate needs more extensive investigation. Our current gIFPM implementation is limited to estimating the 3D applicator pose. Incorporating geometric uncertainties such as gantry angle inaccuracy and detector displacement and orientation into the estimation model is an area of future development. Clinically, applicator rotation errors can be as large as 45 degrees for bad implant or antiverted uterus. The maximum discrepancy between initial and actual pose of the applicator that allows gIFPM to correct pose parameters is under investigation.

*Innovation/Impact*

A novel, accurate, fast and completely automatic method to localize radio-opaque ICB applicators of arbitrary shape from measured 2D x-ray projections is presented, in support of intraoperative brachytherapy dose reconstruction and adaptive replanning. By accurately localizing entire applicator attenuation maps, it has a potential to perform more accurate Monte Carlo based dose calculations and suppress metal streaking artifacts in the CBCT images.

## E SUMMARY AND CONCLUSIONS

IFPM has been shown to be a robust and more accurate tool for localizing a broad range of rigid objects from the measured 2D projections, ranging from small symmetrical spherical seeds to large and complex objects without any rotational symmetry axes in 3D space. Unlike standard back-projection methods, IFPM avoids the need to match corresponding seed images on the projections. It can accommodate incomplete data by iteratively recreating overlapping seeds in the computed projections. By using high resolution 2D projections to localize 3D pose of elongated line-seed and applicator, it can overcome the major difficulties of CT-based method including streaking artifacts and slice thickness limitations. Also, it has some flexibility in the detector model calibration to optimize the gantry angle uncertainties to obtain the best possible projection match.

In paper I it has been shown that starting with a clinically-realistic initial estimate of the seed configuration (TRUS pre-plan), the two-step IFPM algorithm can accurately reconstruct the

brachytherapy seed configuration in the post-implant (week four) patient when using 2D measured projections.

For elongated line seeds (such as Model 6711 $^{125}$I seed, which has a 3 mm × 0.5 mm cylindrical radio-opaque marker), there are two additional degrees of freedom for each seed that describe their orientations in 3D space. The IFPM method described in paper I can not accurately localize seeds centers with un-processed highly elongated radiographic markers. This is because the disk-shaped binary seed image model assumed by the forward projector within the algorithm does not reproduce the binary images produced by cylindrical seeds in shape and size, which can vary from a small disk to highly elongated rectangles depending on seed orientation. To overcome this difficulty, we have introduced generalized IFPM algorithm (5-parameter model) that allows reconstruction of seed positions as well as orientations. Numerical simulations of clinically-realistic brachytherapy seed configurations were performed to demonstrate the proof of concept of this algorithm (paper II). An analytical solution was found for both the similarity metric (objective function) and the gradients of the similarity with respect to all five degrees of freedom of each seed. To rigorously test the accuracy of this new algorithm, a novel precision-machined prostate seed implant phantom, capable of realizing multiple seed configurations of up to 100 seeds to be set with an accuracy of 0.1 mm was developed.

The accuracy of the novel generalized IFPM method using a multi-configuration phantom was about 0.7 mm/6$^{o}$. Considerable improvement in accuracy is obtained as compared to the VariSeed planning, when the seed orientation is taken into account. In paper II, the robust performance of the generalized IFPM in the presence of overlapping seed clusters, highly migrated seeds, missing seed count and errors in accounting the radiographic projection geometry have been shown. By accurately reconstructing the individual seed orientation as well as position, more accurate Monte Carlo-based or 2D TG-43 dose calculation can be performed.

By obtaining the accurate 3D model of the ICB applicators from an external combinatorial geometric modeling code, the IFPM algorithm was further generalized to accurately localize non-cylindrically symmetric objects of arbitrary shape and was applied to ICB applicator pose estimation from a small (3 to 10) set of 2D x-ray projections, in support of

intraoperative brachytherapy planning (paper III). Because of the non-cylindrical symmetry about the axis of rotation, extension from 5-parameter to 6-parameter pose-search algorithm was essential to completely localize arbitrarily-shaped ICB applicators. Using the IFPM approach, we obtained the analytical solution for the similarity metric (objective function) and the gradients (3 positional and 3 orientations) of the similarity with respect to each degree of freedom for each applicator model in the configuration. Unlike conventional approach, this is a fully automated process. It does not require lateral films, which avoids the image quality issues of conventional methods. The novel generalized IFPM algorithm was experimentally validated using the both synthetic-measured and actual-measured images of intrauterine tandem and bilateral colpostats arrangement (paper III). The mean registration error was less than 1 mm for the intrauterine tandem and about 1.5 mm for the bilateral colpostats when compared against the measured projections.

In contrast to conventional single-source-dose-superposition algorithm, the Monte Carlo-based method can be accounted for interseed attenuation, 2D anisotropy, and intra/inter applicator shielding. By accurately localizing radioactive sources as well as full 3D poses of brachytherapy seeds/ICB applicators, the effect of interseed attenuation, 2D anisotropy and inter/intra applicator attenuation can be included in the resultant Monte Carlo or other dose calculations. In combination with advanced image reconstruction algorithms, accurate 3D localization of metal attenuation maps in the patient could contribute to mitigation of metal streaking artifacts on CT/CBCT images. The fully automatic IFPM method is accurate, robust, and capable of completing a reconstruction in a few minutes and is a highly promising tool for implementing in the clinical practice for fusion-based intraoperative brachytherapy planning.

## F FUTURE RESEARCH DIRECTIONS AND POTENTIAL CLINICAL IMPACT

*Explore projection matching using un-segmented images*

Because of the poor imaging contrast of the implanted seeds in the TRUS images, utilization of the x-ray projections is essential, in support of the intraoperative brachytherapy planning. Image registration, seed/applicator, and implanted fiducial marker matching is

essential for image-guided brachytherapy procedures. The results of this thesis have shown that the 3D pose of the implanted brachytherapy seed/applicator can be localized accurately using measured 2D x-ray projections. Thus the clinical implementation of this algorithm is to develop a novel iterative method using un-segmented grayscale images (matching raw projection images, intraoperatively). As a result, partial transmission through the implanted seed/applicator could be accounted. It is a difficult problem to accurately isolate (segment) bone and plastic applicator images when they overlap one another. The grayscale image matching could avoid one of the major problems of segmenting and thresholding fully plastic applicators[79] and brachytherapy seeds having low Z material components. By computing x-ray projections that analytically describe seed/applicator geometry, voxel-based patient anatomical information, DRRs; and matching those DRRs with measured projections could avoid several difficulties including image processing. The computed images should contain at least bony structures and soft-tissue information along with the brachytherapy seed configurations or applicator geometry in the images.

*Potential improvement of Monte Carlo-based or TG - 43 dose calculation*

The $^{125}$I and $^{103}$Pd seeds exhibit considerable anisotropy in their dose distributions due to their internal geometry. The "self-attenuation" by the material along the seed's major axis is the main cause for the seed anisotropy. Our method exploits the individual 3D pose of the implanted brachytherapy seed that can be measured automatically in the clinical setting. After computing 3D pose parameters, it is easy to calculate the more accurate dose that is delivered (by incorporating 2D anisotropy and interseed attenuation) to the patients by using TG-43 report[47] 2D line-seed formalism or Monte Carlo-based dose calculation.[87, 88]

Similar argument can be employed to ICB treatment of cervix. Monte Carlo studies have shown that applicator shielding reduces doses up to 25% when the dose distributions from the bilateral colpostats and intrauterine tandem are included.[59-60] By localizing the applicator internal structure as well as radioactive sources, the effect of intra- and inter-applicators attenuation map can be included in the resultant Monte Carlo or other dose calculation.

*Improve geometric targeting accuracy*

Unlike EBRT, brachytherapy has no well-defined method to evaluate geometric targeting uncertainties (systematic and random errors) –so that meaningful PTV margins can be rationally estimated. IFPM[75-78] can contribute in improving targeting accuracy by using both the accurate modeling of seed/applicator geometry and high spatial resolution projections in the OR intraoperatively, rather than streak-limited CT images for seed and applicator localization. TRUS can be used to localize soft tissues boundaries. It could allow for the identification of under-dosed regions, remedial seed or applicator placement and update the dose distribution, thus making sure that the entire tumor volume receives the prescribed dose while minimizing the dose to the normal-tissues (i.e., rectum and bladder). In the matching process (rigid or non-rigid image registration –3D/2D free-form deformation), IFPM uses natural features in the images (e.g., seeds or applicators themselves, rather than artificial calibration landmarks to constrain the optimization parameters) which could ultimately improve the geometric targeting accuracy as well as studying random and systematic source positioning errors. It could also improve post-implant seed/applicator localization by replacing reconstructed CT-based seed localization by extending 5 and 6-parameter models IFPM approach to multi-slice spiral CT sinogram as well as planar projections. In addition, to improve targeting accuracy, IFPM could facilitate studies to further investigate and quantify inter- and intrafractional targeting uncertainties (because of intrafractional source movement) in the implant by using rigid/non-rigid image registration of the implanted seeds/applicators themselves.

*Improve CBCT image quality for brachytherapy planning*

Applying conventional filtered back-projection algorithms to projection data acquired in the presence of bulky ICB shielded applicators or permanent prostate seed implants results in severe streaking artifacts on CBCT images. The resulting streaking artifacts make segmentation of soft-tissues difficult and introduce large error in dose calculations. For the small foreign metal objects such as seeds, sinogram interpolation (see section B.3 for more detailed) indicates the improvement of CBCT image quality. In addition, scatter subtraction and beam-hardening corrections will further improve the CBCT image quality.

By working with higher resolution 2D projection images (sinograms), IFPM avoids the major difficulties of CT-based localization, such as limited spatial resolution due to slice thickness limitation and ambiguities created by metal streaking artifacts. This ultimately improves the accuracy of seed/applicator localization in the 3D space. *Accurate modeling of the brachytherapy seed and applicator internal structure, material components as well as external geometry will allow us to accurately estimate the partial transmission through the applicator component (i.e. incomplete data) in the sinogram region and may be accounted to improve the CBCT image quality.* Because the interpolation method does not work well for large metal object such as ICB applicators, this problem can be addressed through restoration of tissue-induced sinogram information obscured by metal objects using images acquired *priori* to applicator insertion (pre-operative metal-free images). Accurate knowledge of seed/applicator pose minimizes region in sinogram space that has to be restored and maximizes useful soft-tissue information in sinogram.

Since the x-rays traversing through metal objects are attenuated much more strongly; far fewer photons arrive at the detectors (i.e., inadequate primary photon count rates behind metal objects). As a result, the non-linear effects such as background scatter, beam hardening and stochastic noise due to photon starvation become significant, in the image reconstruction process. Another approach to include the non-linear effects in the image formation process is to use iterative statistical image reconstruction methods.[73-74, 94] An evaluation of novel algorithms such as AM iterative reconstruction for reconstructing CT images from incomplete sinogram date could be performed.[95] However, this approach require a *priori* knowledge of the implanted metal object including its pose, shape, and attenuation map is essential when using AM image reconstruction to mitigate metal streaking artifacts. IFPM could provide the full 3D attenuation map of the implanted metal objects as a potential input for the AM image reconstruction to suppress the metal streaking artifacts. Extension of this method to broader classes of foreign metal objects (such as stirrups, retractors, and table supports, including parameters to describe flex or internal motion within the applicators, partial transmission objects) are potential avenues for future development.

ACKNOWLEDGEMENTS

I wish to express my sincere gratitude to:

Dr. Jeffrey F Williamson, Professor and Chair, my advisor, who has truly been a source of inspiration. He introduced me in to this project and generously guided me throughout this work and shared his complex mathematical concepts and ideas in many long, stimulating discussions and constructive criticisms.

My co-advisor, Dr. Martin J Murphy, Associate Professor, who provided me a platform to pursue this research. He also guided me throughout the course of study, particularly in problem solving, validating new formulae and implementing them. I am constantly benefited from his broad mathematical knowledge and continuous support.

Dr. Dorin A Todor, Associate Professor, who shared his clinical expertise to tackle some difficult problems. Dr. Elisabeth Weiss, Associate Professor, and Dr. Yuichi Motai, Assistant Professor for their continuous support and motivation during this research work.

Dr. Mihaela Rosu, Assistant Professor, though she was not part of my committee, who motivated and inspired me by providing her valuable time and listening to my problems and actively participating in the discussions to tackle the difficult problems.

Virginia Gilbert, Senior Medical Dosimetrist, for her continuous support in collecting data.

Dr. Dimitrios Lazos of Beth Israel Medical Center, NY and Andrew Sampson of VCU, for their valuable help in combinatorial geometric modeling.

Dr. Jun Lu, Dr. John Ford, Jim Ververs and Josh Evans of VCU, for their valuable time to listen to my problems in several useful discussions.

Mike Grieve and Tom Becker for their contribution to phantom construction.

Deanna Pace of VCU, for proof reading the thesis document.

All colleagues in the Department of Radiation Oncology, School of Medicine, VCU who in all respects have facilitated my research work.

My wife Sabita Pokhrel, without her support and encouragement, I would never have made it through the five years of my education at VCU.

My Family and friends in Nepal, for their encouragement and love as I pursued such a long journey.

Varian Medical System and the National Institutes of Health (P01 CA 116602) for their support to perform this research.

APPENDIX 1

Summary of the algorithm workflow of the elongated seed pose reconstruction

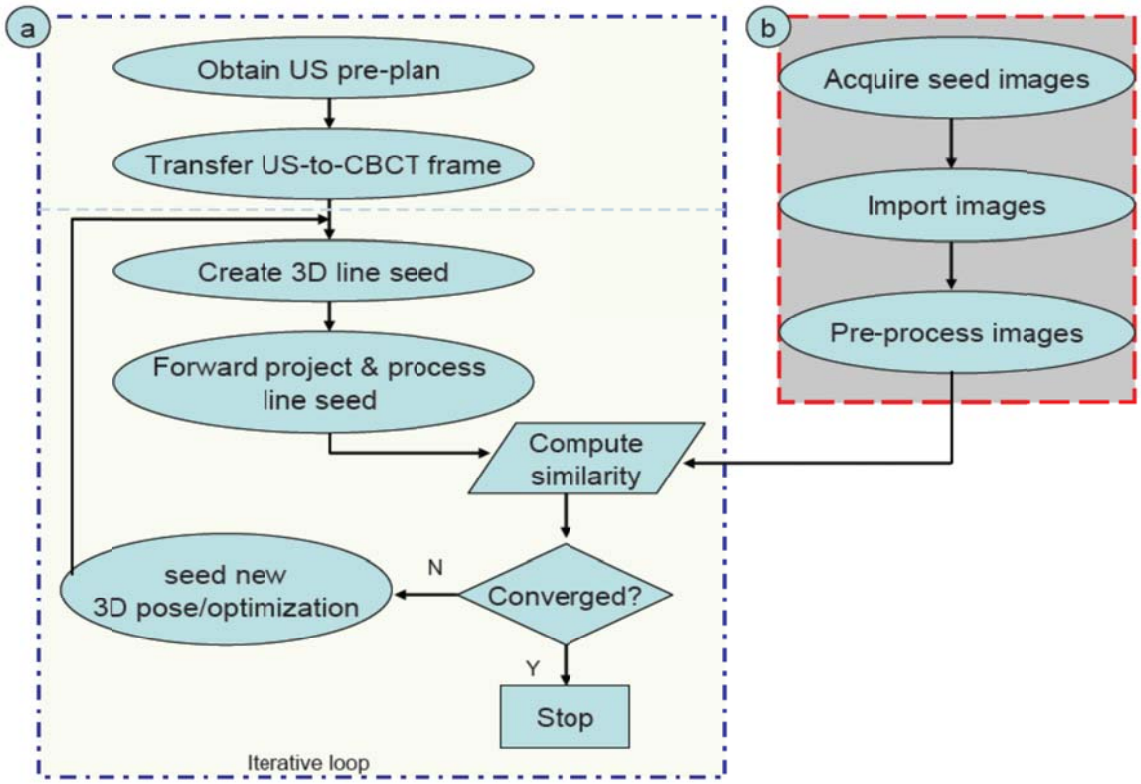


The above flow diagram shows the algorithm workflow of the line seed pose reconstruction process. First part of the diagram (a) represented the initial estimate of seed configuration derived from TRUS pre-plan data which was transferred to the CBCT reference frame. Part (b) of the flow diagram is about the measured elongated line seed images obtained from the clinic. These images are the actual measured images we are trying to match. Second part of the diagram (a) is an iterative loop of the main code. In this process, once we obtained the initial estimate of the seed configurations from TRUS pre-plan datasets, transformed the seed centroid positions to the line seed-model, computed the gradient of the similarity metric with respect all five degrees of freedom for each seed and used that gradient information to the steepest-descent gradient search method to adjust the individual seed pose parameters by iteratively computing the updated DRRs and matched with the measured images.

APPENDIX 2

Summary of the algorithm workflow of the ICB applicators localization

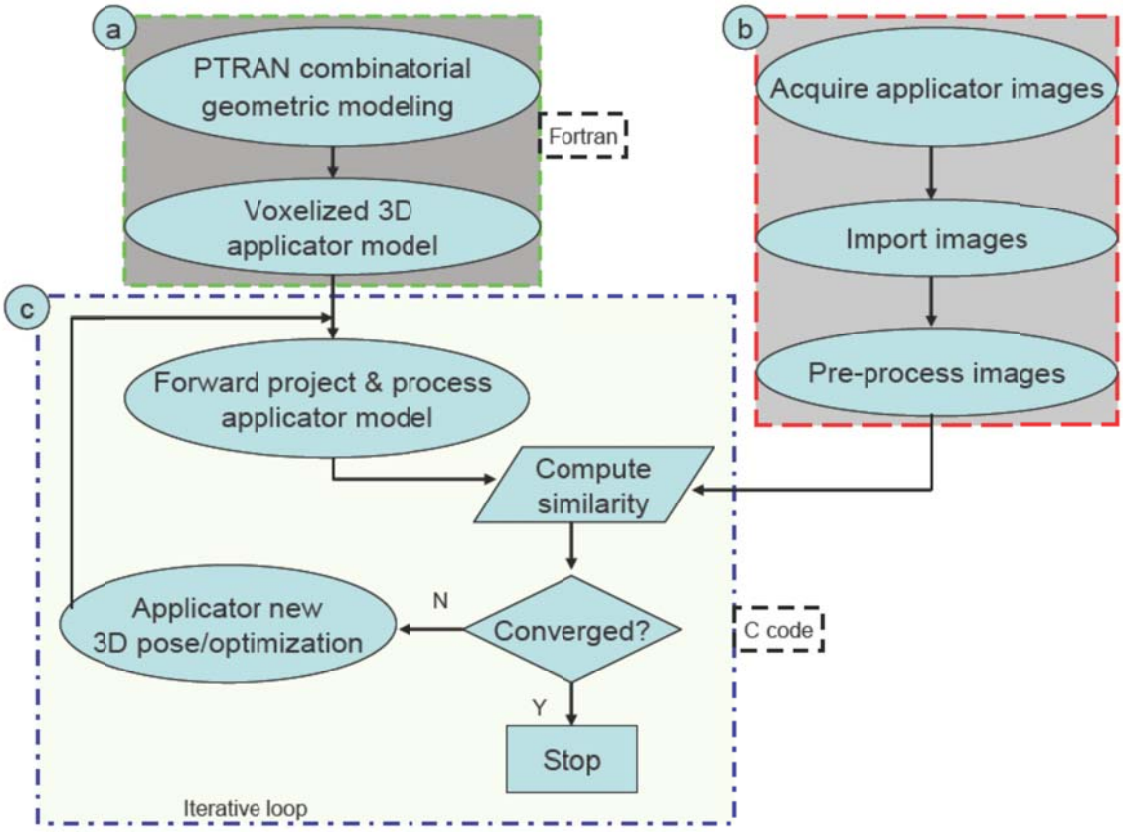


The above flow diagram illustrates the algorithm workflow of the arbitrary-shaped ICB applicator localization process, iteratively. The initial estimate of the applicator models were derived from voxel-based CCG modeling of the applicator geometry which is represented in part (a). Part (b) of the diagram shows the measured applicator images obtained from the clinic. These are the target images which we wish to match. Block (c) of the flow diagram is an iterative loop of the main code. In this process, we need to obtain the initial estimate of the arbitrary-shaped applicator models only once. Then the analytical gradient of the similarity metric with respect to all six degrees of freedom for each applicator model is computed. The gradient information is used to adjust the pose parameters into the steepest-descent method and iteratively match the updated computed applicator model with the measured ones.

REFERENCES

[1]J. F. Williamson, "Brachytherapy technology and physics practice since 1950: a half-century of progress," Phys. Med. Biol. 51, R304-25 (2006)

[2]A. Inciura, L. Jarusevicus, K. Vaiciunas, and E. Juozaityte, "Review on the effectiveness of prostate brachytherapy (*abstract*)," Medicina 45, 660-71 (2009)

[3]N. N. Stone and R. G. Stock, "Permanent seed implantation for localized adenocarcinoma of the prostate (*abstract*)," Urology Reports 3, 201-06 (2002)

[4]Y. Yu, L. L. Anderson, Z. Li, D. E. Mellenberg, R. Nath, M. C. Schell, F. M. Waterman, A. Wu, and J. C. Blasko, "Permanent prostate seed implant brachytherapy: Report of American Association of Physicists in Medicine Task Group Vo. 64," Med. Phys. 26, 2054-76 (1999)

[5]S Nag, J. P. Ciezki, R. Cormack *et al*., "Intraoperative planning and evaluation of permanent prostate brachytherapy: Report of the American brachytherapy society," Int. J. Radiat. Oncol Biol. Phys. 51, 1422-30 (2001)

[6]B. H. Han, K. Wallner, G. Merrick, W. Butler, S. Sutilef, and J. Sylvester, "Prostate brachytherapy seed identification on post-implant TRUS images," Med. Phys. 30, 898-900 (2003)

[7]L. Gong, P. S. Cho, B. H. Han, K. E. Waller, S. G. Sutlief, S. D. Pathak, D. R. Haynor, and Y. Kim, "Ultrasonography and fluoroscopic fusion for prostate brachytherapy dosimetry," Int. J. Radiat. Oncol., Biol., Phys. 54, 1322-30 (2003)

[8]J. N. Roy, K. E. Wallner, P. J. Harrington, C. C. Line, and L. L. Anderson, "A CT-based evaluation method for permanent implants: Applications to prostate," Int. J. Radiat. Oncol Biol. Phys. 26, 163-69 (1993)

[9]W. S. Bice, D. F. Dubois, J. J. Prete, and B. R. Prestidge, "Source localization from axial image sets by iterative relaxation of nearest neighbor criterion," Med. Phys. 26, 1919-24 (1994)

[10]V. Feygelman, B. K. Noriega, R. M. Sanders, and J. L. Friedland, "A spreadsheet techniques for dosimetry of transperineal implants," Med. Phys. 22, 79-100 (1995)

[11]D. H. Brinkmann and R. W. Kline, "Automated seed localization from CT datasets of the prostate," Med. Phys. 25, 1667-72 (1998)

[12]N. Yue, Z. Chen, J. E. Bond, Y. H. Son, and R. Nath, "Combined use of transverse and scout computed tomography scans to localize radioactive seeds in an interstitial brachytherapy implant," Med. Phys. 26, 502-05 (1999)

[13]Z Li, I. A. Nalcacioglu, S. Ranka *et al*., "An algorithm for automatic, computed-tomography-based source localization after prostate implant," Med. Phys. 28, 1410-15 (2001)

[14]H. Liu, G. Cheng, Y. Yu, R. Brasacchio, D. Rubens, J. Strang, L. Liao, and E. Messing, "Automatic localization of implanted seeds from post-implant CT images," Phys. Med. Biol. 48, 1191-03 (2003)

[15]C. Rasch, I. Barillot, P. Remeijer, A. Touw, M. van Herk, and J. V. Lebesque, "Definition of the prostate in CT and MRI: a multi-observer study," Int. J. Radiat. Oncol Biol. Phys. 43, 57-66 (1999)

[16]International Commission on Radiation Units and measurement, report No. 38 Dose and volume specifications for reporting intracavitary therapy in gynecology, (1985)

[17]R. L. Siddon and L. M. Chin, "Two-film brachytherapy reconstruction algorithm," Med. Phys. 12, 77-83 (1995)

[18]H. I. Amols and I. I. Rosen, "A three-film technique for reconstruction of radioactive seed implants," Med. Phys. 8, 210-14 (1981)

[19]D. D Jackson, "An automated method for localizing radioactive seeds in implant dosimetry," Me. Phys. 10, 370-72 (1983)

[20]P. J. Biggs and M. D. Kelley, "Geometric reconstruction of seed implants using a three-film technique," Med. Phys. 10, 701-04 (1983)

[21]M. D. Altschuler, P. A. Findlay, and R. D. Epperson, "Rapid accurate, three-dimensional location of multiple seeds in implant radiotherapy treatment planning," Phys. Med. Biol. 28, 1305-18 (1983)

[22]M. S. Rosenthal and R. Nath, "An automatic seed identification technique for interstitial implants using three isocentric radiographs," Med. Phys. 10, 475-79 (1983)

[23]M. D. Altschuler and A. Kassaee, "Automated matching of corresponding seed images of three simulator radiographs to allow 3D triangulation of implanted seeds," Phys. Med. Biol. 42, 293-302 (1997)

[24]D. Tubic, A. Zaccarin, J. Pouliot, and L. Beaulieu, "Automated seed detection and three-dimensional reconstruction-I. Seed localization from fluoroscopic images or radiographs," Med. Phys. 28, 2265-27 (2001)

[25]D. Tubic, A. Zaccarin, L. Beaulieu, and J. Pouliot, "Automated seed detection and three-dimensional reconstruction-II Reconstruction of permanent prostate implants using simulated annealing," Med. Phys. 28, 2272-79 (2001)

[26]A. Y. C. Fung, "C-Arm imaging for brachytherapy source reconstruction: Geometrical accuracy," Med. Phys. 29, 724-26 (2002)

[27]D. A. Todor, G. N. Cohen, H. I. Amols, and M. Zaider, "Operator-free, film-based 3D seed reconstruction in brachytherapy," Phys. Med. Biol. 47, 2031-48 (2002)

[28]D. A. Todor, M. Zaider, G. N. Cohen, M. F. Worman, and M. J. Zelefsky, "Intraoperative dynamic dosimetry for prostate implants," Phys. Med. Biol. 48, 1153-71 (2003)

[29]E. K. Lee and M. Zaider, "Intraoperative dynamic dose optimization in permanent prostate implants," Int. J. Radiat. Oncol Biol. Phys. 56, 854-61 (2003)

[30]L. Liu, D. A. Bassano, S. C. Prasad et al., "On the use of C-arm fluoroscopy for treatment planning in high dose rate brachytherapy," Med. Phys. 30, 2297-302 (2003)

[31]M. Zhang, M. Zaider, M Worman, and G. Cohen, "On the question of 3D seed reconstruction in prostate brachytherapy: the determination of x-ray source and film locations," Phys. Med. Biol. 49, N335-45 (2004)

[32]S. Narayanan, P. S. Cho, and R. J Marks II, "Fast cross-projection algorithm for reconstruction of seeds in prostate brachytherapy," Med. Phys. 29, 1572-79 (2002)

[33]S. Narayanan, P. S. Cho, and R. J Marks II, "Three-dimensional seed reconstruction from an incomplete data set for prostate brachytherapy," Phys. Med. Biol. 49, 3483-94 (2004)

[34]Y. Su, B. J. Davis, M. G. Herman, and R. A. Robb, "Prostate brachytherapy seed localization by analysis of multiple projections: Identifying and addressing the seed overlap problem," Med. Phys. 31, 1277-87 (2004)

[35]S T Lam, P. S. Cho, R. J. Mark, and S. Narayanan, "Three-dimensional seed reconstruction for prostate brachytherapy using Hough trajectories," Phys. Med. Biol. 49, 557-69 (2004)

[36]S T Lam, P. S. Cho, R. J. Mark, and S. Narayanan, "Detection and correction of patient movement in prostate brachytherapy seed reconstruction," Phys. Med. Biol. 50, 2071-87 (2005)

[37]A. K. Jain, Y. Zhou, T. Mustufa *et al*., "Matching and reconstruction of brachytherapy seeds using the Hungarian algorithm (MARSHAL)," Med. Phys. 32, 3475-92 (2005)

[38]F. A. Siebert, A Srivastav, L Kliemann *et al*., "Three-dimensional reconstruction of seed implants by randomized rounding and visual evaluation," Med. Phys. 34, 967-75 (2007)

[39]R. E. Wallace and J. J. Fan, "Dosimetric characterization of a new design $^{103}$palladium brachytherapy source," Med. Phys. 26, 2465-70 (1999)

[40]A. S. Meigooni, S. A. Dini, S. B. Awan, K. Dou, R. A. Koona, "Theoretical and experimental determination of dosimetric characteristics for ADVANTAGE™ Pd-103 Brachytherapy source," Applied Radiation and Isotopes 64, 881-87 (2006)

[41]A. S. Meigooni, Z. Bharucha, M. Yoe-Sein, and K. Sowards, "Dosimetric Characteristics of the Best® double-wall 103Pd brachytherapy source", Med. Phys. 28, 2568-75 (2001)

[42]J. Lee, C. Labat, A. K. Jain, D. Y. Song, E. C. Burdette, G. Fichtinger, and J. L. Prince, "Optimal matching for prostate brachytherapy seed localization with dimension reduction," Medical Image Computing and Computer-Assisted Intervention: MICCAI 12, 59-66 (2009)

[43]M. Brunet-Benkhoucha, F. Verhaegen, S. Lassalle, D. B. Nadeau, B. Reniers, D. Donath, D. Taussky, and J.-F. Carrier, "Clinical implementation of a digital tomosynthesis-based seed reconstruction algorithm for intraoperative postimplant dose evaluation in low dose rate prostate brachytherapy," Med. Phys. 36, 5235-44 (2009)

[44]J. F. Corbett, J. J. Jezioranski, J Crook, T. Tran, and I. W. T. Yeung, "The effect of seed orientation deviations on the quality of $^{125}$I prostate implants," Phys. Med. Biol. 44, 2785-2800 (2001)

[45]P. Lindsay, J. Battista, and J. V. Dyk, "The effect of seed anisotropy on brachytherapy dose calculations using $^{125}$I and $^{103}$Pd," Med. Phys. 28, 336-45 (2001)

[46]A. S. Glassner, "GRAPHIS GEMS", UK: Academic Press Limited, 98-104 (1990)

[47]M. J. Rivard, B. M. Coursey, L. A. DeWerd, W. F. Hanson, M. S. Huq, G. S. Ibbott, M. G. Mitch, R. Nath, and J. F. Williamson, "Update of AAPM Task Group No. 43 Report: A revised AAPM protocol for brachytherapy dose calculations Dose distributions," Med. Phys. 31, 633-74 (2004)

[48]S. C. Prasad, D. A. Bassano, and P. I. Fear, "Dose distributions for $^{125}$I implants due to anisotropic radiation emission and unknown seed orientation," Med. Phys. 14, 296-98 (1987)

[49]P. Karaiskos, P. Papagiannnis, L. Sakelliou, G. Anagnostopopulos, and D. Baltas, "Monte Carlo dosimetry of the selectSeed $^{125}$I interstitial brachytherapy seed," Med. Phys. 28, 1753-60 (2001)

[50]M. J. Rivard, W. M. Butler, L. A. DeWerd, M. S. Huq, G. S. Ibbott, A. S. Megiooni, C. S. Melhus, M. G. Mitch, R. Nath, and J. F. Williamson, "Supplement to the 2004 update of the AAPM Task Group No. 43 Report," Med. Phys. 34, 2187-05 (2007)

[51]H. Hedtjarn, G. A. Carlsson, and J. F. Williamson, "Monte Carlo-aided dosimetry of the symmetra model I25.S06 $^{125}$I, intestinal brachytherapy seed" Med. Phys. 27, 1076-85 (2000)

[52]M. J. Rivard, "Monte Carlo radiation dose simulations and dosimetric comparison of the model 6711 and 9011 $^{125}$I brachytherapy sources," Med. Phys. 36, 486-91 (2009)

[53]K. T. Sowards and A. S. Meigooni, "A Monte Carlo evaluation of the dosimetric characteristics of the Best Model 2301 125I brachytherapy source," Applied Radiation and Isotopes 57, 327-33 (2002)

[54]S Nag, C. Chao, B. Erickson *et al*., "The American brachytherapy society recommendations for low-dose-rate brachytherapy for carcinoma of the cervix," Int. J. Radiat. Oncol Biol. Phys. 52, 33-48 (2002)

[55]C. A. Pelizzari and G. T. Y. Chen, "A new method for localization of sources in Fletcher-Suit tandems," Int. J. Radiat. Oncol. Biol., Phys.15 (1988)

[56]W. L. Saylor and M. Dillard, "Dosimetry of 137Cs sources with the Fletcher-Suit gynecological applicator," Med. Phys. 3, 117-19 (1976)

[57]K. J. Weeks and G. S. Montana, "Three-dimensional applicator system for carcinoma of the uterine cervix," Int. J. Radiat. Oncol. Biol., Phys.37, 455-63 (1988)

[58]Z. Li and J. F. Williamson, "Volume-based geometric modeling for radiation transport calculations," Med. Phys. 19, 667-77 (1992)

[59]M. J. Price, K. A. Gifford, J. l. Horton *et al*., "Monte Carlo model for a prototype CT-compatible, anatomically adaptive, shielded intracavitary brachytherapy applicator for the treatment of cervical cancer," Med. Phys. 36, 4147-55 (2009)

[60]J. Markman, J. F. Williamson, J. F. Dempsey, and D. A. Low, "On the validity of the superposition principle in dose calculations for intracavitary implants with shielded vaginal colpostats," Med. Phys. 28, 147-55 (2001)

[61]F. A. Lerma and J. F. Williamson, "Accurate localization of intracavitary brachytherapy applicators from 3D CT imaging studies," Med. Phys. 29, 325-33 (2002)

[62]K. J. Weeks, "Monte Carlo dose calculations for a new ovoid shield system for carcinoma of the uterine cervix," Med. Phys. 25, 2288-92 (1998)

[63]K. A. Gifford, F. Mourtada, S. H. Cho *et al*., "Monte Carlo calculations of the dose distribution around a commercial gynecologic tandem applicator," Radiother. Oncol. 77, 210-15 (2005)

[64]N. R. Datta, R. Basu, K. J. Das, *et al*., "Problems and uncertainties with multiple point A's during multiple high-dose-rate intracavitary brachytherapy in carcinoma of the cervix," Clini. Oncol., 16, 129-37 (2004)

[65]L. A. Feldkamp, L. C. Davis, and J. W. Kress, "Practical cone-beam algorithm," Journal of the Optical Society of America A," Optics, Image Science, and Vision 16, 612-19 (1984)

[66]K. A. Gifford, J. L. Horton, Jr., C. E. Pelloski, *et al*., "A three-dimensional computed tomography-assisted Monte Carlo evaluation of ovoid shielding on the dose to the bladder and rectum in intracavitary radiotherapy for cervical cancer," Int. J. Radiat. Oncol. Biol., Phys. 63, 615-21 (2005)

[67]C. C. Ling, M. C. Schell, K. R. Working *et al*., "CT assisted assessment of bladder and rectum dose in gynecological implants," Int. J. Radiat. Oncol. Biol., Phys. 13, 1577-82 (1987)

[68]G. H. Golver and N. J. Pelc, "An algorithm for the reduction of metal clip artifacts in CT reconstruction," Med. Phys. 8, 799-807 (1981)

[69]W. A. Kalender, R. Hebel, and J. Ebersberger, "Reduction of CT Artifacts Caused by Metallic Implants," Radiology, 164, 576-77 (1987)

[70]J. Hsieh, "Adaptive streak artifacts reduction in computed tomography resulting from excessive x-ray photon noise", Med. Phys. 25, 2139-47 (1998)

[71]D. J. Moseley, J. H. Siewerdsen, and D. A. Jaffary, "High-contrast object localization and removal in cone-beam CT," Proc. of SPIE Vol.5745, 40-50 (2005)

[72]A. Docef, M. Murphy, P. Keall *et al*., "Deformed CT reconstruction from limited projections," Proc. of CARS Vol. 1281, 104-8 (2005)

[73]R. J. Murphy, S. Yan, J. A. O'Sullivan, D. L. Snyder, B. R. Whiting, D. G. Politte, G. Lasio, and J. F. Williamson, "Pose estimation of known objects during transmission tomographic image reconstruction," IEEE transactions on medical imaging, vol. 25, no. 10 (2006)

[74]J. F. Williamson, B. R. Whiting, J. Benac, R. J. Murphy, G. J. Blaine, J. A. O'Sullivan, D. G. Politte, and D. L. Snyder, "Prospects for quantitative computed tomography imaging in the presence of foreign metal bodies using statistical image reconstruction," Med. Phys. 29, 2404-18 (2002)

[75]M. J. Murphy and D. A. Todor, "Demonstration of a forward iterative method to reconstruct brachytherapy seed configurations from x-ray projections," Phys. Med. Biol. 50, 2715-37 (2005)

[76]D. Pokhrel, M. J. Murphy, D. A. Todor, E. Weiss, and J. F. Williamson, "Clinical application and validation of an iterative forward projection matching algorithm for permanent brachytherapy seed localization from conebeam-CT x-ray projections," Med. Phys. 37 (9), 5092-5101 (2010)

[77]D. Pokhrel, M. J. Murphy, D. A. Todor, E. Weiss, and J. F. Williamson, "Reconstruction of brachytherapy seed positions and orientations from cone-beam CT x-ray projections via a novel iterative forward projection matching," accepted for publication in Med. Phys. (September 2010)

[78]D. Pokhrel, M. J. Murphy, D. A. Todor, E. Weiss, and J. F. Williamson, "Localizing intracavitary brachytherapy applicators from cone-beam CT x-ray projections via a novel iterative forward projection matching algorithm," accepted for publication in Med. Phys. (October 2010)

[79]S. L. Schoeppel, B. A. Frass, M. P. Hopkins *et al*., "A CT-compatible version of the Fletcher system intracavitary applicator: clinical application and 3-dimentional treatment planning," Int. J. Radiat. Oncol. Biol., Phys. 17, 1103-09, (1989)

[80]N. Milickovic, S. Giannouli, D. Balats *et al*., "Catheter autoreconstruction in computed tomography based brachytherapy treatment planning," Med. Phys. 27, 1047-57 (2000)

[81]S. Li, C. A. Pelizzari, C. Reft, H. G. Sutton, and G. T. Y. Chen, "Computer-aided geometric reconstruction of Fletcher-Suit source positions," Med. Phys. 21, 1123-30 (1994)

[82]S. Haack, S. K. Nielsen, J. C. Lindegaard *et al*., "Applicator reconstruction in MRI 3D image-based dose planning of brachytherapy for cervical cancer," Radiother. Oncol. 91, 187-93 (2009)

[83]A. C. Leeuw, M. A. Moerland, C. Nomden *et al*., "Applicator reconstruction and applicator shifts in 3D MR-based PDR brachytherapy of cervical cancer," Radiother. Oncol. 93, 341-46 (2009)

[84]J. P. Calatayud, F. Kuipers, F. Ballester *et al*., "Exclusive MRI-based tandem and colpostats reconstruction in gynecological brachytherapy treatment planning," Radiother. Oncol. 91, 181-86 (2009)

[85]J. H. Siewerdsen and D. A. Jaffray, "Cone-beam computed tomography with a flat-panel imager: magnitude and effects of x-ray scatter," Med. Phys. 28, 220-31 (2001)

[86]R. Sibson, "A brief description of natural neighbor interpolation (Chapter 2) Interpreting Multivariate Data," John Wiley, 21-36 (1981)

[87]H. Afsharpour, M. D'Amours, Benoite Cote *et al*., "A Monte Carlo study on the effect of seed design on the interseed attenuation in permanent prostate implants," Med. Phys. 35, 3671-81 (2008)

[88]O. Chibani, J. F. Williamson, and D. Todor, "Dosimetric effects of seed anisotropy and interseed attenuation for $^{103}$Pd and $^{125}$I prostate implants," Med. Phys. 32, 2557-66 (2005)

[89]J-F Carrier, L. Beaulieu, F. Therriault-Proulx, and R. Roy, "Impact of interseed attenuation and tissue composition for permanent prostate implants," Med. Phys. 33, 595-04 (2006)

[90]G. Leclerc, M.-C. Lavallee, D. Tubic, J. Metivier, E. Vigneault, and L. Beaulieu, "Idealized line source configuration for permanent 125I prostate implants," Radiother. Oncol. 72, 213-20 (2004)

[91]D. Tubic and L. Beaulieu, "Sliding slice: A novel approach for high accuracy and automatic 3D localization of seeds from CT scans," Med. Phys. 32, 163-74 (2006)

[92]W. L. Smith, C. Lewis, G. Bauman, G. Rodrigues, D. D'Souza, R. Ash, D. Ho, V. Venkatesan, D. Downey, and A. Fenster, "Prostate volume contouring: a 3D analysis of segmentation using 3DTRUS, CT, and MR," Int. J. Radiat. Oncol., Biol., Phys. 67, 1238-47 (2007)

[93]H. Westendorp, C. J. Hoekstra, A. van't Riet, A. W. Minken, and J. J. Immerzeel, "Intraoperative adaptive brachytherapy of iodine-125 prostate implants guided by C-arm cone-beam computed tomography-based dosimetry," Brachytherapy 6, 231-37 (2007)

[94]J. A. Fessler, "Statistical Image Reconstruction Methods for Transmission Tomography," *in Handbook of Medical Imaging, Medical Image Processing and Analysis*, edited by M. Sonka and J. M. Fitzpatrick, SPIE, Vol. 2, 1-70 (2000)

[95]D. L. Snyder, J. A. O'Sullivan, R. Murphy, D. G. Politte, B. R. Whiting, and J. F. Williamson, "Image reconstruction for transmission tomography when projection data are incomplete," Phys. Med. Biol. 51, 5603-19 (2006)

[96]R. R. Liu, S. Rudin, and D. R. Bednarek, "Super-global distortion correction for a rotational C-arm x-ray image intensifier," Med. Phys. 26, 1802-10 (1999)

**Paper I**

**Paper II**

**Paper III**

## Paper I

**Clinical application and validation of an iterative forward projection matching algorithm for permanent brachytherapy seed localization from conebeam-CT x-ray projections**

Damodar Pokhrel

Martin J Murphy

Dorin Todor

Elisabeth Weiss

Jeffrey F Williamson

Medical Physics, 37 (9), 5092-5101 (2010)

# Clinical application and validation of an iterative forward projection matching algorithm for permanent brachytherapy seed localization from conebeam-CT x-ray projections

Damodar Pokhrel, Martin J. Murphy, Dorin A. Todor,
Elisabeth Weiss, and Jeffrey F. Williamson[a)]
*Department of Radiation Oncology, School of Medicine, Virginia Commonwealth University, Richmond, Virginia 23298*

(Received 7 May 2010; revised 29 July 2010; accepted for publication 30 July 2010; published 31 August 2010)

**Purpose:** To experimentally validate a new algorithm for reconstructing the 3D positions of implanted brachytherapy seeds from postoperatively acquired 2D conebeam-CT (CBCT) projection images.
**Methods:** The iterative forward projection matching (IFPM) algorithm finds the 3D seed geometry that minimizes the sum of the squared intensity differences between computed projections of an initial estimate of the seed configuration and radiographic projections of the implant. In-house machined phantoms, containing arrays of 12 and 72 seeds, respectively, are used to validate this method. Also, four $^{103}$Pd postimplant patients are scanned using an ACUITY digital simulator. Three to ten x-ray images are selected from the CBCT projection set and processed to create binary seed-only images. To quantify IFPM accuracy, the reconstructed seed positions are forward projected and overlaid on the measured seed images to find the nearest-neighbor distance between measured and computed seed positions for each image pair. Also, the estimated 3D seed coordinates are compared to known seed positions in the phantom and clinically obtained VariSeed planning coordinates for the patient data.
**Results:** For the phantom study, seed localization error is $(0.58 \pm 0.33)$ mm. For all four patient cases, the mean registration error is better than 1 mm while compared against the measured seed projections. IFPM converges in 20–28 iterations, with a computation time of about 1.9–2.8 min/iteration on a 1 GHz processor.
**Conclusions:** The IFPM algorithm avoids the need to match corresponding seeds in each projection as required by standard back-projection methods. The authors' results demonstrate ~1 mm accuracy in reconstructing the 3D positions of brachytherapy seeds from the measured 2D projections. This algorithm also successfully localizes overlapping clustered and highly migrated seeds in the implant. © *2010 American Association of Physicists in Medicine*. [DOI: 10.1118/1.3480962]

Key words: brachytherapy, localization, iterative forward projection matching, conebeam-CT, x-ray projections

## I. INTRODUCTION

In the past decade, permanent implantation of radioactive $^{125}$I or $^{103}$Pd seeds into the prostate has become a common treatment option for patients with organ-confined prostate cancer.[1] Current clinical practice involves creating an ultrasound-based preimplant plan about a week before treatment. A postimplant dose evaluation is then performed using 3D CT images acquired at week four, following the implantation to document the delivered dose. However, as presently practiced, this process does not allow for intervention during the implant procedure to improve the actual treatment.

Recent advances in imaging and treatment delivery technology now provide the opportunity to perform intraoperative dose reconstruction to further optimize the implant. A key step in intraoperative planning is identifying the locations of all seeds with respect to the underlying anatomy. In principle, one can use in-room fan-beam CT (FBCT) for this purpose. Reconstruction of seed coordinates from postimplant 3D CT images is already routinely applied in clinical practice.[2,3] However, in addition to poor soft-tissue contrast and large (up to 8 mm when compared to axial magnetic resonance images) prostate contouring errors,[4] FBCT suffers from streaking artifacts arising from the implanted metal seeds, overlapping seed clustering, and resolution limited by the slice thickness. Also, intraoperative FBCT installations in brachytherapy suites are uncommon.

A more common approach to seed localization is back-projection of seed positions in 2D x-ray projections using two-film[5] and three-film[6–11] techniques. The reconstructed implant geometry is then fused to intraoperatively acquired ultrasound images, upon which dose planning can be performed. However, in back-projection methods, corresponding seeds in each projection must be identified and matched.[12–19] This problem is not always soluble because of seed clustering and overlapping, resulting in inaccurate seed localization due to mismatched or missing seeds. Patient mo-

tion and uncertainty in imaging device positioning during image acquisition can further confound seed localization when using back-projection methods.

With the introduction of dedicated conebeam-CT (CBCT) imaging systems for seed placement, we can combine the advantages of a rigidly mounted intraoperative imaging system, seed reconstruction from 2D projection radiographs, and reconstruction of 3D anatomy in the same coordinate system from a full set of projections. However, even with the resulting improvements in the calibration and stability of the imaging geometry, reconstruction via back-projection remains problematic.

This study assesses the robustness and accuracy of a promising new reconstruction method, the "iterative forward projection matching" (IFPM) algorithm, which was introduced by Murphy and Todor[20] for reconstructing 3D coordinates of implanted seeds from 2D radiographic projections. The IFPM method was designed to avoid the problems of back-projection localization methods, such as the need to determine the seed correspondences between different projections, the ambiguities presented by clustered or missing seeds in the projections, and uncertainties in the projection geometry such as gantry angle inaccuracy and possible patient motion between image acquisitions. It accomplishes this by iteratively adapting an initial estimate of the 3D seed configuration until the agreement between the acquired projections of the implanted seeds and the computed projection images of the estimated seed configuration is maximized. By matching the projection of the full seed configuration rather than individual seed projections, IFPM intrinsically accommodates incomplete and ambiguous data by recreating the overlapping seeds in the matching computed images. The algorithm also allows the imaging viewpoints (projections) for the digitally reconstructed radiographs (DRRs) to be adjustable parameters to accommodate gantry angle uncertainties up to 8° with respect to the first projection. This is a particularly useful feature if the images have been acquired using a mobile C-arm. In this study, we experimentally validate IFPM using a dummy seed (nonradioactive) containing phantoms and demonstrate its ability to reconstruct clinical patient implants.

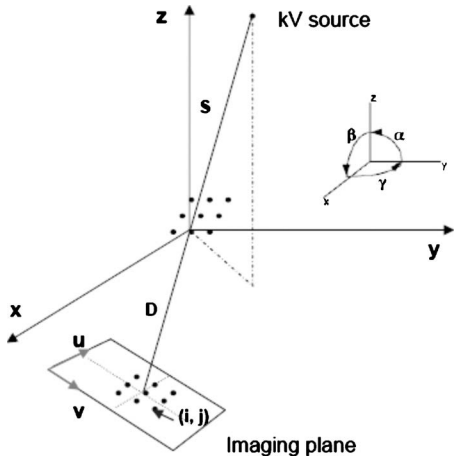


FIG. 1. The perspective projection geometry for the imaging system. The 3D seed configuration is in the world coordinate system, which is defined by three translational and three rotational coordinates relative to the CBCT isocenter. The image receptor plane is defined by the imaging viewpoint angles $(\alpha,\beta,\gamma)$, where $S$ and $D$ denote the constant values between the source to isocenter and detector to isocenter distances, respectively. The imaging axis rotates by angle $\alpha$ around the x axis. The pixel index $(i,j)$ denotes the projected seed in the 2D imaging plane $(u,v)$.

## II. MATERIALS AND METHODS

### II.A. IFPM algorithm

The IFPM algorithm[20] works with a set of $M$ 2D projection images of the actual seed configuration in the patient. The imaging geometry for the $M$ projections is measured to obtain the detector model.[20] The IFPM algorithm starts with an initial estimate of the seed configuration. The (x,y,z) coordinates of the center of each seed are free parameters. The initial estimate of the 3D seed configuration is forward projected onto each 2D detector plane via a detector model simulating that of the acquired projection to produce $M$ computed projection images of the seeds that emulate the acquired images. The computed projections are compared to the actual projections by calculating the pixel-by-pixel squared intensity differences (SSQD) of the image intensities. The (x,y,z) coordinates of each seed are then independently adjusted in an iterative process until the computed projections optimally match the acquired images (i.e., when the total SSQD for the $M$ image pairs has been minimized).

The world coordinate frame is defined by three translational variables (x,y,z), where the x, y, and z axes are left/right lateral, anterior/posterior, and superior/inferior directions, respectively, relative to the CBCT isocenter for a supine patient with the head toward the gantry base. Figure 1 shows a schematic of the perspective projection geometry used to create each of the $M$ projection images of the seed configuration. In the world frame, the 3D seed configuration of $N$ total seeds is defined by $\{\boldsymbol{r}_k\}, k=(1,N)$. In the extrinsic detector model, the orientation of each isocentric projection in the world coordinate frame is defined by the angles $(\alpha,\beta,\gamma)$, which describe rotations of the detector image plane around the x, y, and z axes, respectively. In practice, $\alpha\approx 90°$, $\beta\approx 0°$, and $\gamma$ is the gantry angle for each $M$ image viewpoint. However, the complete extrinsic detector model allows for a precise calibration of the imaging plane orientation $(\alpha,\beta,\gamma)$ at each gantry angle to allow for tilting and/or twisting of the image plane due to gantry flex and other mechanical imperfections. The intrinsic detector model is parametrized by describing its magnification, image center, image size, and pixel resolution. $S$ and $D$ denote the constant values between the source to isocenter and detector to isocenter distances, respectively, and $(u,v)$ is the 2D detector plane.

As mentioned earlier, IFPM not only adjusts the individual seed positions until the computed and measured projections match, but can also simultaneously adjust each x-ray projection, with six degrees of freedom relative to the first projection (i.e., the reference projection, which is fixed) to

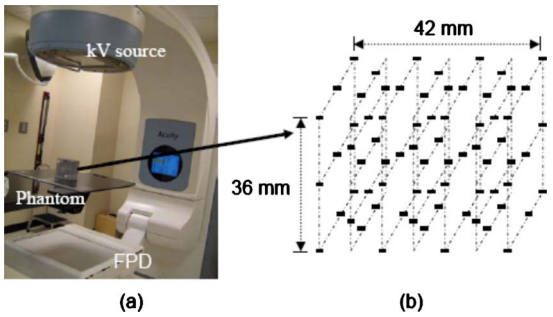


FIG. 2. (a) The ACUITY imaging system in the brachytherapy imaging suite and a phantom setup. (b) Schematic of the geometrical configuration of a precision-machined phantom containing 72 dummy seeds arranged as four nine-seed slabs alternating with three 12-seed slabs in a rectangular grid. This phantom was used to test the IFPM seed localization accuracy. The centers of the seeds were coplanar and perpendicular to the plane of the slabs.

account for uncertainties in the detector model calibration (i.e., the uncertainties in the relative imaging viewpoints).

To avoid the time-consuming task of computing complete DRRs of the simulated seed configuration via attenuation ray-tracing through the patient's anatomy, it is sufficient for IFPM to project the centers of the seeds in the model configuration along the rays from x-ray source to the detector. This produces binary 2D images of the centers of the seeds. The center of each projected seed on the detector plane is dilated to represent a small disk of uniform brightness of thickness $t$, which is approximately equal to a Theragenics Model 200 $^{103}$Pd seed (Theragenics Corporation, Buford, GA) radiographic marker, so that the unblurred projections of each binary seed image are approximately equal to the measured projections in shape and size. The acquired images are then filtered to highlight the seeds, also yielding a set of binary images. Both sets of binary images are then convolved with a Gaussian blurring function to produce grayscale images in which the seeds appear as fuzzy spots. The blurring process produces smoothly varying grayscale image gradients that facilitate gradient-driven minimization of the SSQD. The algorithm then computes the gradient of the SSQD with respect to each seed's three degrees of freedom to drive the iterative minimization process. It also computes the gradient of the SSQD with respect to the degrees of freedom, e.g., $(\alpha,\beta,\gamma)$, in the detector model to adjust the imaging geometry for an optimal match.

### II.B. Image acquisition details and autosegmentation of the seeds

Both the phantom and patient validation tests reported here use projection images obtained with the Varian ACUITY intraoperative imaging system (Varian Inc., Palo Alto, CA), which is used for image-guided brachytherapy procedures in our dedicated brachytherapy suite. This imaging system can be operated in CBCT, fluoroscopic, and/or radiographic modes. Figure 2(a) shows the phantom setup in the ACUITY system and Fig. 2(b) shows the geometric configuration of the 72-seed phantom used in this study (see Sec. II D 1 for more details).

The projection images are acquired with the Varian 4030CB flat panel detector. This detector is $40\times30$ cm$^2$ with a $1024\times768$ image size, pixel size of 0.388 mm/pixel, and 16-bit depth. The ACUITY imaging geometry has a 100 cm source to isocenter distance and a 150 cm source to detector distance, giving a magnification factor of 3/2. Approximately 660 CBCT images are obtained for a complete 360° gantry rotation. Subsets of three to ten images each are used for the IFPM tests.

For the model 6711 $^{125}$I dummy seeds (Medi-Physics Inc., Arlington Heights, IL) used in the phantom study, the radio-opaque components include $3\times0.5$ mm$^2$ cylindrical silver markers that are represented by their center locations. This requires postprocessing of the acquired projection images to find and highlight the marker projections. The postprocessing involves (a) cropping the images to a $256\times256$ pixel square region of interest, (b) normalizing the image intensity by finding its maximum and minimum values in the image, (c) morphological top-hat filtering to suppress the background, and (d) automatic thresholding using the three standard deviation value of the pixel intensity histogram to create a binary marker for each seed in each projection in order to separate the seeds from the background. This produces binary bitmap images with intensity=0 in the background and intensity=1 over the area of each projected seed marker. The center locations of each seed projection image in the 2D detector plane are obtained by computing the center of mass for each radio-opaque marker. The binary images are then convolved with a 2D Gaussian blurring function to create diffuse seed spots with a known intensity distribution. This produces smoothly varying image gradients that can be computed analytically in the test projections to guide the objective function minimization and speed up the convergence of the matching process.

For the patient study (see Sec. II D 2 for more details), image processing is identical to that applied to the phantom implant projections, except that we retain the binary image of the entire radio-opaque marker ($1.09\times0.5$ mm$^2$) in the model 200 $^{103}$Pd seed, which avoids resolving seed clusters in the 2D measured projections.

### II.C. Algorithm details

#### *II.C.1. Initial seed configuration estimates and computed projection images*

For the phantom study, the initial seed configuration $\{\boldsymbol{r}_k\}$ is chosen as follows, where $k=(1,N)$ is the seed number and $N$ is the total number of seeds. For each seed k, the known 3D seed coordinates $\{\boldsymbol{r}_{k,0}\}$ are randomly perturbed by adding a displacement $\boldsymbol{d}_k$, such that $\boldsymbol{r}_k=\boldsymbol{r}_{k,0}+\boldsymbol{d}_k$, where $\boldsymbol{d}_k$ is randomly sampled from a uniform distribution $[-2$ mm, 2 mm$]$ in each of the three orthogonal directions, resulting in a mean displacement of 1.98 mm. To construct the computed projec-

tion images at each iteration, the initial configuration $\{\boldsymbol{r}_k\}$ is rotated and translated to each imaging viewpoint and then projected on the $(u,v)$ imaging plane.

For each patient case, $\{\boldsymbol{r}_k\}$ is derived from the pretreatment transrectal ultrasound (TRUS) volume study, which gives x, y, and z coordinates of each seed centroid in an image coordinate system that is fixed to the TRUS planning target volume structure. Since the 2D measured projection images used by IFPM are taken in the CBCT reference frame, we transform the seed centroid TRUS coordinates to the CBCT coordinate system by using rotation, translation, and scaling. The reference frames of both imaging systems are orthogonal, right-handed coordinate systems. Therefore, the translation is performed by aligning the isocenters (centroids) of the two imaging systems and the rotation is obtained by finding the conventional x, y, and z coordinates of the ultrasound imaging system used in our clinic and transforming them to the known CBCT imaging coordinate system. As with the phantom study, the transformed 3D seed configuration (ultrasound-to-CBCT reference frame) is rotated and translated for each imaging viewpoint and then projected on the imaging plane.

For each imaging gantry position $\gamma$, each seed's position projected onto the imaging plane $(u,v)$, where it is represented by a small disk of uniform brightness of thickness $t$, which is approximately equal to a model 200 $^{103}$Pd seed radiographic marker. This produces a binary bitmap image of the seed projections. These images are then convolved with the same 2D Gaussian blurring filter (with standard deviation $\sigma$) that is used for the measured projections to produce grayscale images and denoted by $I_c(u,v|\{\boldsymbol{r}_k\},\sigma,\gamma)$, where $u$ and $v$ are pixel indices along the 2D imaging plane.

The purpose of blurring the projected seed disks with a Gaussian is to create grayscale images with smoothly varying gradients that extend beyond the seed's projected cross section. This facilitates the use of a gradient-driven iterative solution. If the binary bitmap images were used directly, there would be large areas with no gradient to guide the iterative search. The blurring can be thought of as creating a potential well around each seed that attracts neighboring seeds and accelerates convergence. Increasing the width of the Gaussian increases the capture range (i.e., the maximum distance over which seeds in the two images can be drawn together).

#### II.C.2. Similarity measure and gradient search

The metric used to assess the overall similarity of the images is computed by combining the pixel-by-pixel SSQD for all computed $I_c(u,v|\{\boldsymbol{r}_k\},\sigma,\gamma)$ and measured $I_m(u,v|\sigma,\gamma)$ seed image pairs.

$$\mathrm{SSQD}(\{\boldsymbol{r}_k\}|\sigma,\gamma)=\sum_{\gamma}\sum_{u,v}[I_c(u,v|\{\boldsymbol{r}_k\},\sigma,\gamma)-I_m(u,v|\sigma,\gamma)]^2, \quad (1)$$

where $(u,v)$ are pixel indices in the 2D image plane and $\gamma$ is the gantry angle. The seed positions $\{\boldsymbol{r}_k\}$ and the initial imaging viewpoint parameters except for the first projection (i.e., the reference viewpoint) are iterated simultaneously by a steepest descent search algorithm. Unlike the reference viewpoint, which is not allowed to vary, other imaging viewpoints are defined relative to the first projection in terms of rotation and translation. Because the image grayscale intensities are described entirely by the Gaussian blurring function, the gradients of SSQD with respect to all of the free parameters can be calculated analytically.[20] Since the brachytherapy seed marker represented by a small disk in this study has rotational symmetry, we use seed center coordinates to calculate one derivative per seed per degree of freedom.

After computing the analytical gradients to adjust all free parameters, the process iteratively refines the 3D seed positions and projection orientations $(\alpha,\beta,\gamma)$, until the agreement between the computed and measured seed projections is maximized. To iteratively adjust the free parameters that minimize SSQD, we use a nonlinear gradient search method that combines the steepest descent gradient search with a parabolic approximation of the SSQD surface around the global minimum.[20] The computed and measured projections must have the same imaging geometry, image size, and pixel resolution. At least two, but preferably three or more, pairs of computed and measured projection image data sets with corresponding imaging geometry are required for one reconstruction process. The $3N$ seed positions plus six $(M-1)$ degrees of freedom of the imaging viewpoints are the freely moveable parameters in each iteration, where $M$ is the total number of projections.

#### II.C.3. Two-step adaptive Gaussian blurring

From the phantom studies, it is observed that the computed seed locations at convergence vary somewhat (i.e., trapping in local minima). That means if the initial estimate of the seed configuration is far apart from the measured configuration, there is a chance of less than optimal matching. To improve the accuracy of the patient study, we apply a two-step adaptive blurring scheme: We use a larger 2D Gaussian spreading (i.e., $\sigma_1$) to achieve initial convergence and then recompute the images using a smaller Gaussian blurring filter (i.e., $\sigma_2$), using the optimal $\sigma_1$ seed configuration as initial conditions for the $\sigma_2$ search. The two-step Gaussian blurring strategy uses more diffuse seed spots (i.e., increases the capture range) in the configuration at the beginning to draw the computed and measured seeds into close proximity and then increases the sharpness of the seed spots to get the optimal match near convergence. The optimal values of two-step blurring, $\sigma_1$ and $\sigma_2$, are obtained from trial and error for each patient seed configuration and are between 3.8 and 3.0 mm, and 2.6 and 2.0 mm, respectively.

### II.D. Algorithm validation

#### II.D.1. Brachytherapy phantom design

Two different in-house brachytherapy phantoms were designed and fabricated using acrylic plates with dummy seeds in known configurations. In the acrylic plates, a matrix of parallel holes was drilled such that each hole is of 0.9 mm diameter so that seeds can be placed in the holes. The model

6711 $^{125}$I seeds are each 4.5 mm long and 0.8 mm in diameter. The seeds were arranged in rectilinear layers separated by 6 mm, with 8–12 mm interseed spacing within a plate. After loading the seeds, the plates were mounted tightly together with screws. Both phantoms were $10\times10\times7$ cm$^3$. The first phantom contains 12 seeds. The second phantom contains 72 seeds, a more clinically realistic brachytherapy phantom. For the 72-seed phantom, the seeds were arranged by four nine-seed slabs alternating with three 12-seed slabs in a rectangular grid as shown in Fig. 2(b).

To evaluate the positional accuracy, the known 3D seed centroids obtained from the machined phantoms were compared to the corresponding reconstructed IFPM seed centroids. Accurate comparisons of the seed positions can be made since the absolute positions of the seeds in the phantom are known within the machining precision of 0.2 mm.

### II.D.2. Patient data acquisition

Following the phantom tests, the IFPM algorithm was applied to the more difficult problem of brachytherapy seed reconstruction for actual patients, using images acquired 1 month after the permanent seed implants. The four selected patients (I–IV) all had been treated for low risk stage I prostate adenocarcinoma and were imaged postoperatively, i.e., approximately 4 weeks postimplant using a Varian ACUITY digital simulator equipped with a CBCT imaging system. The preloaded permanent seed implants consisted of 67, 62, 81, and 60 model 200 $^{103}$Pd interstitial sources, respectively. The 660 CBCT projections were acquired in a 360° gantry rotation using the Varian 4030CB imager in full-fan/half-fan mode. The images were acquired at 125 kVp, 80 mA, and 25 ms per projection. For those postoperative scans, the patients were positioned head first and supine with legs down.

To make up the measured projection data set, we selected three to ten x-ray images from the CBCT projection data sets acquired from the ACUITY digital simulator. The choice of perspectives was based on visibility of the large number of seeds on the projection images and also to avoid imprecision caused by excessively small parallaxes. For the patients I, III, and IV, the images were selected at 8°–12° angular intervals over a ±40° range of gantry angles. Since patient II was scanned in half-fan mode, the images were selected at the same angular interval as the other patients but over ±160° (i.e., posterior/anterior view) range of gantry angles. The images were postprocessed as described in Sec. II B. One example case of the image postprocessing and seed detection for a patient is presented in Fig. 3. The binary seed images are then convolved with a 2D Gaussian blurring function. Three to six pairs of selected gantry angle projection images were used in each seed reconstruction process.

### II.D.3. Assessment of seed registration/ reconstruction error

For the phantom study, the seed reconstruction error was computed by directly comparing the computed seed coordinates with the physically measured (with machined uncertainty of ±0.2 mm) seed coordinates. For the patient data sets, there are no ground truth seed coordinates. Assessment of seed reconstruction error was performed in two ways. First, seed registration error is calculated by reprojecting the IFPM seed coordinates at convergence onto the 2D image planes, overlaying the computed and measured seed projection and calculating the nearest-neighbor distance between the measured and computed seed positions in each image plane, making sure that no measured seed projection was matched to more than one computed image. In the second approach, we compared the IFPM 3D coordinates from the reconstructed CBCT image sets to those obtained by the VariSeed planning system. For each candidate IFPM seed position, we find the VariSeed source position that minimized the 3D distance between the IFPM and VariSeed coordinates. The seed reconstruction error was quantified by computing the vector and scalar displacement between the IFPM and VariSeed coordinates. In the VariSeed planning system, the resultant seed centroids have limited accuracy because of slice thickness limitations, metal streaking artifacts, and problems of resolving seed clusters. These uncertainties are included in our estimation of the accuracy of the IFPM solution for the seed positions.

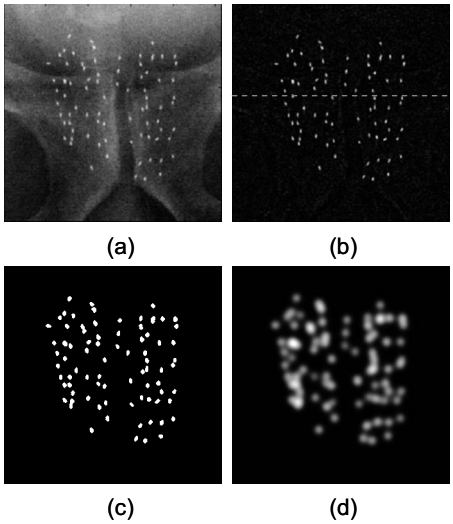


FIG. 3. An example case of the image postprocessing of the projection images obtained from the Varian 4030CB digital simulator. (a) Raw projection image, (b) filtered image, (c) seed-only image, and (d) blurred image using the IFPM algorithm for patient III (81 implanted Theragenics model 200 $^{103}$Pd seeds).

## III. RESULTS

### III.A. Validation test with phantoms

The phantom study is the best way to test the accuracy of the IFPM algorithm since the reconstructed seed positions can be compared to the measured precision-machined seed positions. Figure 4 shows the convergence of the objective function Eq. (1) as defined in Sec. II C 2, for the 12-seed and 72-seed phantom data sets. In these cases, we used a one-step ($\sigma$=2.4 mm) convergence process. For the 72-seed phantom case, the root-mean-square (RMS) error, in terms of 3D distance between IFPM and benchmark coordinates, was found

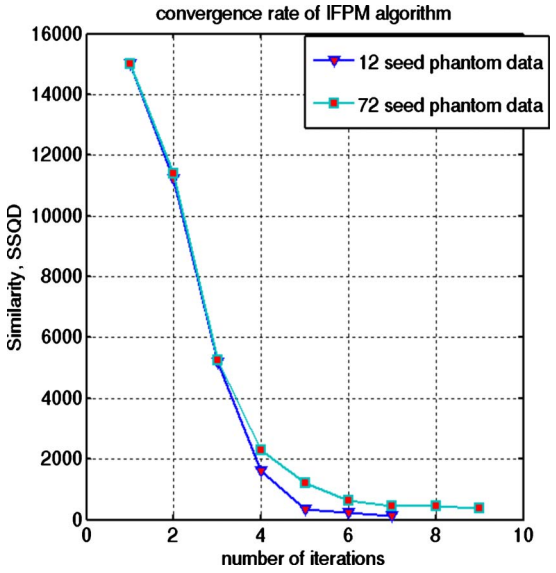


FIG. 4. The convergence rate of the IFPM algorithm for the two example cases: 12-seed and 72-seed phantom data sets.

to be $(0.58 \pm 0.33)$ mm. For the 12-seed phantom case, the RMS error was even smaller $(0.43 \pm 0.24)$ mm. The distribution of seed reconstruction errors is shown in Fig. 5 where we show that greater than 96% of the reconstructed seed positions are within 1 mm from the measured seed positions (72-seed phantom). The reconstructed values of relative $(\alpha, \beta, \gamma)$ deviated from their nominal values with respect to 0° gantry angle (i.e., reference viewpoint) by 0.08°, 0.06°, and 0.7° for −20° gantry angle and 0.09°, 0.03°, and 0.6° for +20° gantry angle. Experiments showed that relative viewpoints uncertainties as large as ±8° could be accommodated.

All test trials for 12-seed phantom data sets converge in four to six iterations with a total computation time of 2.8–4 min and for 72-seed phantom data sets the objective function converges on eight to ten iterations with a total computation time of 30–53 min on a 1 GHz processor (running time depends on number of seeds used in the implants, i.e., the number of free parameters to optimize). Several experiments

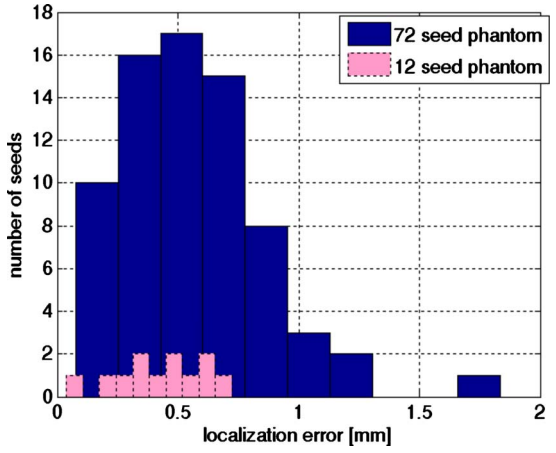


FIG. 5. Histograms of the seed positional error for the 12-seed and 72-seed phantom study.

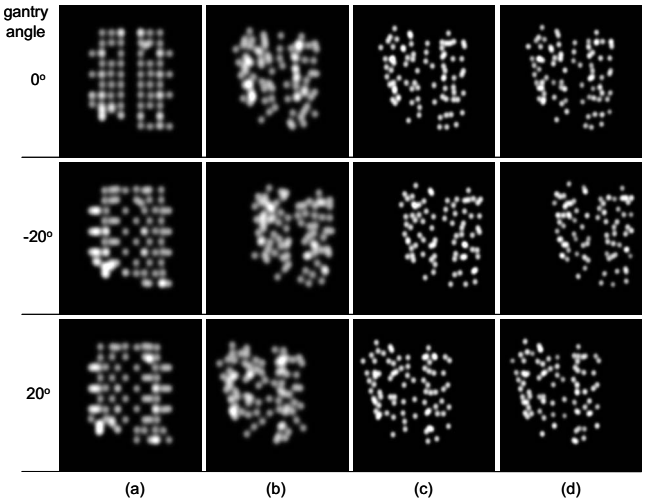


FIG. 6. An illustration of the iterative sequence morphing of the convergence process. (a) Initial estimate of the seed configuration, (b) computed images after first step of convergence, (c) computed images after second step of convergence, and (d) the measured images at different gantry angle for patient III. Despite large differences between the preplanned seed geometry (based on a TRUS volume study acquired about a week before the implant) and that observed 4 weeks after the implant, IFPM was able to accurately reproduce the desired seed configuration.

were performed using different gantry angle combinations as well as different initial starting configurations in the course of this study. Theoretically, one should expect SSQD=0 at the convergence, i.e., all computed seed images exactly match with those measured. However, from Fig. 4, for the 72-seed phantom data sets, it is evident that the SSQD does not exactly converge to zero (i.e., less than 3% difference between measured and computed seed images), showing less than optimal convergence. To improve the accuracy of the reconstructed seed positions in the patient study, we used a two-step blurring scheme as described earlier.

### III.B. Patient study

For each of the four postimplant prostate patient data sets, we followed the two-stage iterative process as described in Sec. II C 3. Figure 6 illustrates the convergence process for the 81-seed implant performed on patient III. Three projections, at 0° and ±20° gantry angle, were used. Column (a) shows the initial seed configuration estimate derived from the TRUS-based preplan while column (d) shows the projections acquired four weeks after the procedure. Columns (b) and (c) show projections of the converged seed configurations for the initial $(\sigma_1)$ and final $(\sigma_2)$ Gaussian blurring models. Comparison of (c) and (d) shows good agreement, including successful replication of overlapping seed clusters, which appear as brighter or elongated seed features in the images. For this case, the first stage (Gaussian width $\sigma_1=3.6$ mm) required 23 iterations with a computation time of about 2.4 min/iteration and five iterations in the second stage ($\sigma_2=2.4$ mm), with a computation time of about 2.8 min/iteration on a 1 GHz processor. Figure 7 shows the two-stage convergence rate of the objective function for the four example patient cases. An example of the reconstructed seed

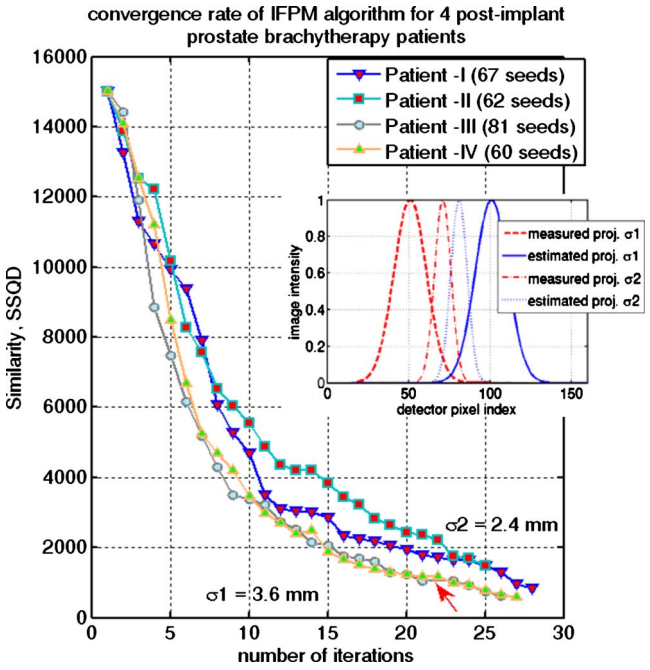


FIG. 7. The similarity metric convergence for the two-step IFPM algorithm for the four patient cases. The arrow in the button of the figure indicates the transition from larger to smaller Gaussian spread for patient III. The one-dimensional image-intensity profiles in the inset illustrate the capture ranges of the two-step filtering operations.

positions projected on the digital simulator images is presented in Figs. 8(a)–8(c). The distribution of nearest-neighbor distances between the computed and measured projected seed centroids is presented in Fig. 9. The RMS errors are $(0.78 \pm 0.56)$ (0°), $(0.89 \pm 0.49)$ (+20°), and $(0.82 \pm 0.54)$ mm (−20°), respectively. We see that most seed positions agree to within 1.5 mm and no error exceeds 2.5 mm in the detector plane.

For patient III, Fig. 10 shows the seed-by-seed vector displacement between IFPM and VariSeed seed coordinates. The mean values along the x, y, and z directions were found to be $(0.22 \pm 0.96)$, $(-0.24 \pm 0.97)$, and $(0.23 \pm 0.92)$ mm, respectively. The 3D RMS error was $(1.58 \pm 0.56)$ mm. The comparison is summarized for all four patients in Table I. Since we do not know the ground truth for the patient study, this seed localization error includes not only the error from the IFPM algorithm but also the error contributed by the

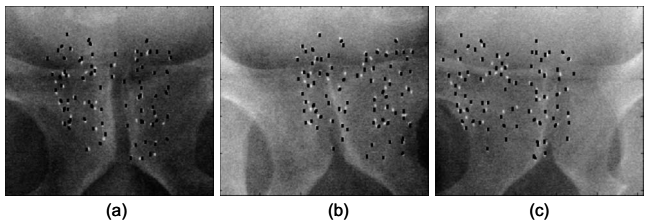


FIG. 8. Superposition of measured seed images (white seeds) with automatically detected seed positions (black markers) projected on the detector planes. (a) 0° gantry angle, (b) −20° gantry angle, and (c) +20° gantry angle for patient III. While many seeds coincided exactly, a few still exhibit significant discrepancies.

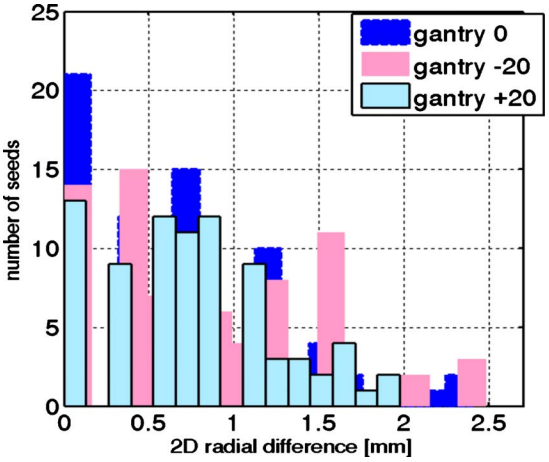


FIG. 9. Seed registration error calculated from the nearest-neighbor distance between measured and computed seed position on each detector plane for patient III. The RMS error was found to be $(0.78 \pm 0.56)$ (0°), $(0.89 \pm 0.49)$ (+20°), and $(0.82 \pm 0.54)$ mm (−20°) gantry angles, respectively.

VariSeed planning system. Table I also shows the residual 2D registration error between the measured and computed seed projections in each image plane. In all cases, the RMS value of the seed registration error is within 1 mm and the maximum seed displacement ($d_{max}$) did not exceed 2.5 mm. Increasing the number of projections from three to six reduces this error by a factor of $\sqrt{2}$ at the cost of doubling computation time.

In Fig. 11, we overlay measured seed images (white seeds) with automatically detected seed positions (black markers) projected on the detector planes for patient IV, who presented an example of incomplete data due to more seeds existing in the preplan than observed on postimplant projections (i.e., missing seeds). In this case, the clinical records (and preplan) showed that 60 $^{103}$Pd seeds were implanted, but only 59 seeds could be localized on the postimplant images acquired 4 weeks after the procedure. Thus the 3D model seed configuration had one more seed than was present in the computed images; gantry angle 0° is shown in Fig. 11(a), −20° is shown in Fig. 11(b), and +18° is shown in Fig. 11(c), respectively. The red circle indicates the projected position of the extra seed in the 3D preplan, which has

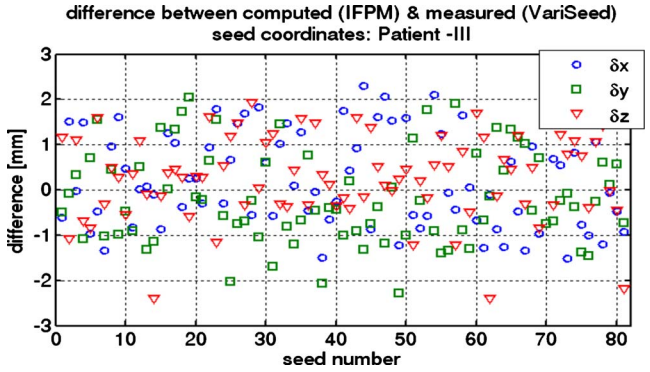


FIG. 10. Seed-by-seed vector difference between IFPM coordinates and those obtained from the VariSeed planning system for patient III data sets.

TABLE I. Summary of the comparisons of the seed positions deduced by the IFPM algorithm and by the VariSeed planning system for all example case patients. The mean value, standard deviation (sd) in each of the three directions, and overall 3D RMS error is reported. The seed registration error in the 2D image plane in terms of RMS value. The sd and the maximum displacement ($d_{max}$) of the seed is also presented.

| Patient no. | Image viewpoint used (deg) | Total no. of iterations | IFPM vs VariSeed (mm) $\bar{\delta x} \pm$ sd | IFPM vs VariSeed (mm) $\bar{\delta y} \pm$ sd | IFPM vs VariSeed (mm) $\bar{\delta z} \pm$ sd | 3D RMS error | 2D registration error in each image plane (mm) RMS error | 2D registration error in each image plane (mm) $d_{max}$ |
|---|---|---|---|---|---|---|---|---|
| I | 0 | 28 | 0.38 ± 0.97 | 0.20 ± 0.98 | 0.25 ± 0.87 | 1.64 ± 0.54 | 0.63 ± 0.86 | 1.96 |
| | +15 | | | | | | 0.74 ± 0.53 | |
| | −16 | | | | | | 0.78 ± 0.72 | |
| II | 180 | 25 | 0.35 ± 0.98 | 0.19 ± 1.08 | 0.26 ± 0.89 | 1.76 ± 0.59 | 0.82 ± 0.83 | 2.44 |
| | −160 | | | | | | 0.94 ± 0.74 | |
| | +165 | | | | | | 0.86 ± 0.92 | |
| III | 0 | 26 | 0.22 ± 0.96 | −0.24 ± 0.97 | 0.23 ± 0.92 | 1.58 ± 0.56 | 0.78 ± 0.56 | 2.35 |
| | −20 | | | | | | 0.89 ± 0.49 | |
| | +20 | | | | | | 0.82 ± 0.54 | |
| IV[a] | 0 | 27 | 0.37 ± 1.16 | −0.29 ± 1.04 | 0.28 ± 0.98 | 1.86 ± 0.68 | 0.83 ± 0.63 | 2.48 |
| | −20 | | | | | | 0.98 ± 1.22 | |
| | +18 | | | | | | 0.96 ± 0.82 | |

[a]Incomplete data case.

no counterpart in the measured images. The IFPM algorithm converged robustly to an accurate estimate of the seed configuration that was only slightly perturbed in the vicinity of the extra seed. Comparing measured and computed seed images shows that the two-step iterative convergence process closely reproduces the desired seed distribution. In the same case of patient IV, the IFPM algorithm was able to account for seeds that had migrated as far as 5 mm from their preplanned positions (which appear in the lower left corner of the postimplant images). Clusters of two to four overlapping seeds were also reproduced on the computed projections.

## IV. DISCUSSION

We have experimentally validated a novel iterative forward projection matching method to reconstruct 3D brachytherapy seed coordinates from measured 2D projection images. The iterative process does not require one to establish seed correspondences between the projection images. Also, it avoids the intraobserver and interobserver variability of seed finding that is often observed when using three-film methods.[5–11] It can correct for errors in the measured imaging geometry by iteratively adjusting the imaging gantry positions used in the iterative projection process.

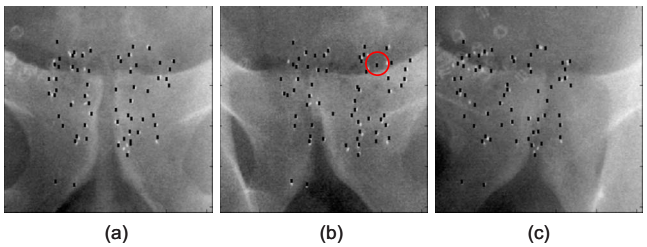


FIG. 11. Overlay of the measured seed images (white seeds) with automatically detected seed positions (black markers) projected on the detector planes for patient IV, who presents with incomplete data: 60 seeds are thought to be implanted but only 59 seeds are found on the week four postimplant dosimetry study. Gantry angle 0° is shown in (a), −20° is shown in (b), and +18° is shown in part (c). The circle in part (b) indicates the extra seed found by IFPM at convergence. The IFPM algorithm converged accurately, recreating the identified 59 seed positions, including overlapping clustered and highly migrated seeds.

Current clinical practice relies on reconstructed 3D CT images for reconstructing seed positions.[21,22] As reported in the literature[3,12] and found in our clinical experience with VariSeed planning, this method frequently finds more than the actual number of implanted seeds, as the same seed may appear in more than one slice. Also, the 3D CT method is hampered by metal streaking artifacts.

Because the spatial resolution of the seeds in the 2D image planes is superior to CT, IFPM has the potential to reconstruct 3D seed positions more accurately than the 3D CT method. By using CBCT projections, the IFPM method provides the potential for intraoperative brachytherapy planning. Several methods are available for reconstructing brachytherapy seeds from 2D projection images[12–19] but they are limited by the requirement that all seeds must be accurately identified in each projection. It is a difficult problem because the large number of implanted seeds in a relatively small prostate volume often results in seed clustering and overlaps in the projections. Lee *et al.*[26] have proposed a fluoroscopy based algorithm to solve the overlapping seed problem using dimensionality reduction. A brachytherapy seed reconstruction method based on digital tomosynthesis has recently been applied in clinical practice.[27] In one clinical experience, nearly 20% of the implanted seeds overlapped with other seeds in at least one projection.[19] Tubic *et al.*[12] have shown that their method can handle seed localization in small clusters of two or three overlapping seeds in the projection but fail to correctly reconstruct seeds in large clusters.

Our method reproduces overlapping seed clusters and highly migrated seeds in the postimplant data analysis by

finding the best solution that accounts for the data available. In our approach, individual seed identities do not matter; the algorithm works with the images of the complete seed configuration so it can easily accommodate incomplete data as well. For the case of patient IV, which showed a missing seed on the measured projection images (i.e., incomplete data), the algorithm converged to an accurate solution that was only slightly perturbed near the extraneous seed. Identification of the extra seed(s) in this way allows one to modify the initial 3D seed configuration and to correct the preplan before rerunning the reconstruction.

To improve the accuracy of the seed localization validation study, we plan to design a more precise prostate seed implant phantom and test IFPM performance against a more accurate ground truth. Also, more extensive investigation of the initial estimate of the seed configurations as well as a more optimal search of the blurring parameter will be performed to further validate this algorithm. Other geometric uncertainties such as detector in/out of plane motion and inaccuracy in the magnification factor are also an area of future investigation.

For elongated seeds (such as the model 6711 $^{125}$I seed, which has a 3 mm long by 0.5 mm diameter cylindrical marker), there are two additional degrees of freedom for each seed that describe their orientations in 3D space. The IFPM method described herein does not accurately localize seeds with highly elongated radiographic markers. This is because the disk-shaped binary seed image model assumed by the forward projector within the algorithm does not reproduce the binary images produced by cylindrical seeds in shape and size, which can vary from a small disk to highly elongated rectangles depending on seed orientation. The data presented here suggest that the IFPM algorithm works effectively for seeds with radio-opaque components having an aspect ratio no larger than the 2:1 ratio characteristic of the model 200 $^{103}$Pd source. Other currently available brachytherapy seeds satisfying this constraint include the Prospera (North America Scientific Inc., Chatsworth, CA) model MED3631,[23] IsoAid (IsoAid LLC, Port Richey, FL) Advantage™ model IAPd-103A,[24] and Best (Best Medical International, Inc., Springfield, VA) model 2335 sources.[25] Because sources with radio-opaque components with an aspect ratio larger than this dominate the market (i.e., model 6711 $^{125}$I seed), our next developmental priority is to model entire elongated line seeds, allowing IFPM to estimate individual seed orientations as well as locations. IFPM is also being extended to localization of larger metal objects, e.g., surgical needles and brachytherapy applicators (i.e., tandem and colpostats).

## V. CONCLUSIONS

In this paper, we described a clinically useful and refined implementation of the IFPM algorithm, which was described conceptually and tested on synthetic data sets by Murphy and Todor. Testing on phantoms demonstrates that seed localization error is $\pm 0.5$ mm or better on average, which is less than the estimated uncertainty of the seed centroid coordinates taken as the gold standard for validating accuracy. Application of the algorithm to four patient data sets demonstrates the potential for accurate implant reconstruction in clinical settings, with average 2D convergence errors less than 1 mm. The outcomes on these early test cases, while not comprehensive, suggest that IFPM performance is not negatively impacted by seed clusters or missing seeds. In its current form, clinical implementation of IFPM is limited to seed models containing internal radio-opaque markers with an aspect ratio of approximately 2:1 or less.

Postimplant imaging is currently done 4 weeks after implant but can potentially be done intraoperatively via CBCT to permit immediate postimplant dosimetry assessments. This requires a fast, automatic, and robust method to reconstruct the seed configuration at the time of implantation. The fully automatic IFPM algorithm is accurate, robust, and capable of completing a reconstruction in a few minutes using state-of-the-art workstations and is therefore a highly promising tool for implementing fusion-based intraoperative brachytherapy planning.

## ACKNOWLEDGMENTS

This work was supported in part by grants from Varian Medical Systems and the National Institutes of Health (Grant No. P01 CA 116602). The authors gratefully acknowledge Virginia Gilbert of Virginia Commonwealth University (VCU) for her continuous support in collecting patient data. The authors would like to thank Tom Becker for his contributions to phantom construction. The authors thank James Ververs of VCU for editing the manuscript.

[a]Author to whom correspondence should be addressed. Electronic addresses: jwilliamson@mcvh-vcu.edu and jfwilliamson@vcu.edu; Telephone: 804-828-8451.

[1]Y. Yu, L. L. Anderson, Z. Li, D. E. Mellenberg, R. Nath, M. C. Schell, F. M. Waterman, A. Wu, and J. C. Blasko, "Permanent prostate seed implant brachytherapy: Report of American Association of Physicists in Medicine Task Group No. 64," Med. Phys. **26**, 2054–2076 (1999).
[2]Z. Li, I. A. Nalcacioglu, S. Ranka, S. K. Sahini, J. R. Palta, W. Tome, and S. Kim, "An algorithm for automatic, computed-tomography-based source localization after prostate implant," Med. Phys. **28**, 1410–1415 (2001).
[3]D. H. Brinkmann and R. W. Kline, "Automated seed localization from CT datasets of the prostate," Med. Phys. **25**, 1667–1672 (1998).
[4]C. Rasch, I. Barillot, P. Remeijer, A. Touw, M. van Herk, and J. V. Lebesque, "Definition of the prostate in CT and MRI: A multi-observer study," Int. J. Radiat. Oncol., Biol., Phys. **43**, 57–66 (1999).
[5]R. L. Siddon and L. M. Chin, "Two-film brachytherapy reconstruction algorithm," Med. Phys. **12**, 77–83 (1984).
[6]H. I. Amols and I. I. Rosen, "A three-film technique for reconstruction of radioactive seed implants," Med. Phys. **8**, 210–214 (1981).
[7]D. D. Jackson, "An automated method for localizing radioactive seeds in implant dosimetry," Med. Phys. **10**, 370–372 (1983).
[8]P. J. Biggs and M. D. Kelley, "Geometric reconstruction of seed implants using a three-film technique," Med. Phys. **10**, 701–704 (1983).
[9]M. D. Altschuler, P. A. Findlay, and R. D. Epperson, "Rapid accurate, three-dimensional location of multiple seeds in implant radiotherapy treatment planning," Phys. Med. Biol. **28**, 1305–1318 (1983).
[10]M. S. Rosenthal and R. Nath, "An automatic seed identification technique for interstitial implants using three isocentric radiographs," Med. Phys. **10**, 475–479 (1983).
[11]M. D. Altschuler and A. Kassaee, "Automated matching of corresponding seed images of three simulator radiographs to allow 3D triangulation of implanted seeds," Phys. Med. Biol. **42**, 293–302 (1997).

[12]D. Tubic, A. Zaccarin, J. Pouliot, and L. Beaulieu, "Automated seed detection and three-dimensional reconstruction. I. Seed localization from fluoroscopic images or radiographs," Med. Phys. **28**, 2256–2271 (2001).
[13]D. Tubic, A. Zaccarin, L. Beaulieu, and J. Pouliot, "Automated seed detection and three-dimensional reconstruction. II. Reconstruction of permanent prostate implants using simulated annealing," Med. Phys. **28**, 2272–2279 (2001).
[14]A. Y. C. Fung, "C-arm imaging for brachytherapy source reconstruction: Geometrical accuracy," Med. Phys. **29**, 724–726 (2002).
[15]D. A. Todor, G. N. Cohen, H. I. Amols, and M. Zaider, "Operator-free, film-based 3D seed reconstruction in brachytherapy," Phys. Med. Biol. **47**, 2031–2048 (2002).
[16]D. A. Todor, M. Zaider, G. N. Cohen, M. F. Worman, and M. J. Zelefsky, "Intraoperative dynamic dosimetry for prostate implants," Phys. Med. Biol. **48**, 1153–1171 (2003).
[17]S. Narayanan, P. S. Cho, and R. J. Marks II, "Fast cross-projection algorithm for reconstruction of seeds in prostate brachytherapy," Med. Phys. **29**, 1572–1579 (2002).
[18]S. Narayanan, P. S. Cho, and R. J. Marks II, "Three-dimensional seed reconstruction from an incomplete data set for prostate brachytherapy," Phys. Med. Biol. **49**, 3483–3494 (2004).
[19]Y. Su, B. J. Davis, M. G. Herman, and R. A. Robb, "Prostate brachytherapy seed localization by analysis of multiple projections: Identifying and addressing the seed overlap problem," Med. Phys. **31**, 1277–1287 (2004).
[20]M. J. Murphy and D. A. Todor, "Demonstration of a forward iterative method to reconstruct brachytherapy seed configurations from x-ray projections," Phys. Med. Biol. **50**, 2715–2737 (2005).
[21]J. N. Roy, K. E. Wallner, P. J. Harrington, C. C. Line, and L. L. Anderson, "A CT-based evaluation method for permanent implants: Applications to prostate," Int. J. Radiat. Oncol., Biol., Phys. **26**, 163–169 (1993).
[22]W. S. Bice, D. F. Dubois, J. J. Prete, and B. R. Prestidge, "Source localization from axial image sets by iterative relaxation of nearest neighbor criterion," Med. Phys. **26**, 1919–1924 (1999).
[23]R. E. Wallace and J. J. Fan, "Dosimetric characterization of a new design $^{103}$palladium brachytherapy source," Med. Phys. **26**, 2465–2470 (1999).
[24]A. S. Meigooni, S. A. Dini, S. B. Awan, K. Dou, and R. A. Koona, "Theoretical and experimental determination of dosimetric characteristics for ADVANTAGE™ Pd-103 Brachytherapy source," Appl. Radiat. Isot. **64**, 881–887 (2006).
[25]A. S. Meigooni, Z. Bharucha, M. Yoe-Sein, and K. Sowards, "Dosimetric characteristics of the Best® double-wall 103Pd brachytherapy source," Med. Phys. **28**, 2568–2575 (2001).
[26]J. Lee, C. Labat, A. K. Jain, D. Y. Song, E. C. Burdette, G. Fichtinger, and J. L. Prince, "Optimal matching for prostate brachytherapy seed localization with dimension reduction," in Proceedings of the 12th International Conference on Medical Image Computing and Computer-Assisted Intervention (MICCAI), 2009, Vol. 5761, pp. 59–66.
[27]M. Brunet-Benkhoucha, F. Verhaegen, S. Lassalle, D. B. Nadeau, B. Reniers, D. Donath, D. Taussky, and J. F. Carrier, "Clinical implementation of a digital tomosynthesis-based seed reconstruction algorithm for intraoperative postimplant dose evaluation in low dose rate prostate brachytherapy," Med. Phys. **36**, 5235–5244 (2009).

**Paper II**

# Reconstruction of brachytherapy seed positions and orientations from cone-beam CT x-ray projections via a novel iterative forward projection matching method

Damodar Pokhrel

Martin J Murphy

Dorin Todor

Elisabeth Weiss

Jeffrey F Williamson

Accepted for publication in Medical Physics, September (2010)

**Reconstruction of brachytherapy seed positions and orientations from cone-beam CT x-ray projections via a novel iterative forward projection matching method**

Damodar Pokhrel, Martin J Murphy, Dorin A Todor, Elisabeth Weiss, and Jeffrey F Williamson
Department of Radiation Oncology, School of Medicine, Virginia Commonwealth University, Richmond, Virginia 23298

**Abstract**

**Purpose**: To generalize and experimentally validate a novel algorithm for reconstructing the 3D pose (position and orientation) of implanted brachytherapy seeds from a set of a few measured 2D cone-beam CT (CBCT) x-ray projections.

**Methods and materials**: The iterative forward projection matching (IFPM) algorithm was generalized to reconstruct the 3D pose, as well as centroid, of brachytherapy seeds from three to ten measured 2D projections. The gIFPM algorithm finds the set of seed poses that minimizes the sum-of-squared-difference (*SSQD*) of the pixel-by-pixel intensities between computed and measured auto-segmented radiographic projections of the implant. Numerical simulations of clinically realistic brachytherapy seed configurations were performed to demonstrate the proof of principle. An in-house machined brachytherapy phantom, which supports precise specification of seed position and orientation at known values for simulated implant geometries, was used to experimentally validate this algorithm. The phantom was scanned on an ACUITY CBCT digital simulator over a full 660 sinogram projections. Three to ten x-ray images were selected from the full set of CBCT sinogram projections and post-processed to create binary seed-only images.

**Results**: In the numerical simulations, seed reconstruction position and orientation errors were approximately 0.6 mm and 5°, respectively. The physical phantom measurements demonstrated an absolute positional accuracy of (0.78 ± 0.57) mm or less. The $\theta$ and $\varphi$-angle errors were found to be (5.7 ± 4.9)° and (6.0 ± 4.1)°, respectively or less when using three projections; with six projections results were slightly better. The mean registration error was better than 1 mm/ 6° while compared against the measured seed projections. Each test trial converged in 10 – 20 iterations with computation time of 12 – 18 min/iteration on a 1 GHz processor.

**Conclusion**: This work describes a novel, accurate, and completely automatic method for reconstructing seed orientations as well as centroids, from a small number of radiographic projections, in support of intraoperative planning and adaptive replanning. Unlike standard back-projection methods, gIFPM avoids the need to match corresponding seed images on the projections. This algorithm also successfully reconstructs overlapping clustered and highly migrated seeds in the implant. The accuracy of better than 1 mm and 6° demonstrates that gIFPM has the potential to support 2D Task Group 43 calculations in clinical practice.

Key words: Brachytherapy Seed Orientation, Localization, gIFPM, Cone-beam CT, X-ray projections.

## I. INTRODUCTION

Post-implant localization of brachytherapy seeds implanted in the prostate allows for validation against the planned seed poses (positions and orientations) as well as the opportunity to recalculate the actual delivered dose. Transrectal ultrasound (TRUS) guidance implantation provides adequate imaging of the soft tissue anatomy but is not able to accurately reconstruct individual seed poses relative to the prostate during or after the implantation.[1] Currently, post-implant CT is the standard of practice for evaluating and reporting dose[2-7], however, it does not allow for altering and optimizing the treatment plan intraoperatively. The 3D CT method is hampered by metal streaking artifacts and limited spatial resolution due to slice thickness effects as well as lack of intraoperative CT imaging capability.

With the introduction of dedicated ACUITY (Varian Medical System, Palo Alto, CA) cone-beam CT (CBCT) digital simulator for seed placement, we can combine the advantages of a rigidly-mounted intraoperative imaging system, for the both seed reconstruction and reconstruction of 3D anatomy of the patient which could be used for contouring.[8] However, the ACUITY CBCT imaging system in our procedure room requires about four minutes to acquire CT images and can not provide useful images with the TRUS probe and metal stirrups that are located within or occlude the field of view.

Reconstructing seeds from a few sinogram projections can overcome some of the problems associated with the CT-based method, such as limited spatial resolution due to slice thickness effect, ambiguities created by the metal streaking artifacts, and reduced imaging time since neither a full sinogram nor a reconstructed 3D image are necessary. By fusing the seed coordinates reconstructed from radiographs with TRUS images[9-17], rapid intraoperative seed reconstruction can be combined with the higher soft tissue contrast characteristic of TRUS.[18] However, widely used conventional back-projection (BP) methods[19-25] for localizing seeds from projection images require corresponding seed images in each projection to be matched. When a large number of elongated seeds are projected into a small area in each projection, it can be very difficult to completely resolve seed clusters and isolate each seed centroid.

As currently practiced, conventional seed localization techniques only attempt to find the center of the elongated line seeds (i.e., point source approximation) for dose calculation. By directly measuring the individual 3D pose of each implanted brachytherapy seed, more accurate Monte Carlo-based dose calculations (or 2D TG-43 dose calculations[31]) can be employed to include the effect of 2D anisotropy and interseed attenuation on the resultant dose distribution. Corbett *et al.*[26] found that incorporating 2D anisotropy functions into the dose calculation slightly improved (~1%) dose volume histogram (DVH) accuracy relative to the isotropic point-seed model, but they did not report on local dose differences. However, for $^{125}$I and $^{103}$Pd implants, Lindsay *et al.*[27] showed that omitting 2D anisotropy corrections introduced large local dose variations that collectively exceeded 10% in 20% to 40% of the target volume. Monte Carlo-based dose evaluations demonstrate that interseed attenuation[40, 43] may reduce $D_{90}$ doses by as much as 5% and dose-calculation models that account for the local seed anisotropy[41] may deviate by as much as 7.5% from one-dimensional point-source dose computations. While a few investigators have developed generalized BP[38-39] and CT-based algorithms[45] for estimating seed orientation as well as position, they suffer from the same limitations as their more widely used centroid localization counterparts.

In a companion paper we have introduced[28] and experimentally validated on both phantom and patient datasets a novel algorithm[29], iterative forward projection matching

(IFPM), which overcomes many of the disadvantages of CT-based and BP methods for localizing seed centroids from radiographic images. In this paper, we introduce a generalized IFPM (gIFPM) algorithm that allows reconstruction of seed orientations as well as positions. gIFPM uses a model of the projection geometry and pre-plan seed positions, and then iteratively adjusts the imaging system model parameters and the 3D seed poses to maximize agreement between the computed forward projections and measured (acquired) projections. Our method eliminates the need to match corresponding seed images, resolves overlapping seed clusters, and has the potential to accommodate incomplete data due to missing seeds. We demonstrate the accuracy and robustness of five degrees-of-freedom gIFPM using both synthetic datasets and experimentally measured projections of an in-house precision-machined prostate seed implant phantom.

## II. MATERIALS AND METHODS

### A. Generalized IFPM algorithm

The IFPM algorithm[29] was adapted from Murphy and Todor[28] and generalized to reconstruct seed orientations as well as positions. This expanded line seed-model requires five free pose parameters, $(x, y, z, \theta, \varphi)_k$ for each of the seeds $k = 1, \cdots, N$ in the world coordinate system; where, $\mathbf{r}_k = (x, y, z)_k$ denotes the coordinates of the *k-th* seed center and $(\theta, \varphi)_k$ describes its orientation. The length of the radiographically visible seed components is denoted by $L$ as shown in Figure 1. A model of the CBCT projection geometry is made and positioned at $M$ different locations and orientations specified by translation and rotation matrices, $T_{x,y,z}$ and $[R]_{\alpha.\beta.\gamma}$ for each image viewpoint. The origin of the world coordinate is at the CBCT isocenter; the x axis is left-right, the y axis is anterior-posterior, and the z axis is superior-inferior direction, for a patient in supine position with feet pointing away from the gantry stand. The three angles, $(\alpha, \beta, \gamma)$ describe the orientation of CBCT central ray and detector panel relative to the three world coordinate system axes for each image viewpoint. In practice, $\alpha = 90^o$, and $\beta = 0^o$ and $\gamma$ is the gantry angle for each $M$ image viewpoint. The detector model is parameterized by

describing its magnification, image center, image size and pixel resolution. The source to isocenter and isocenter to the detector distances are denoted by *S* and *D*, respectively.

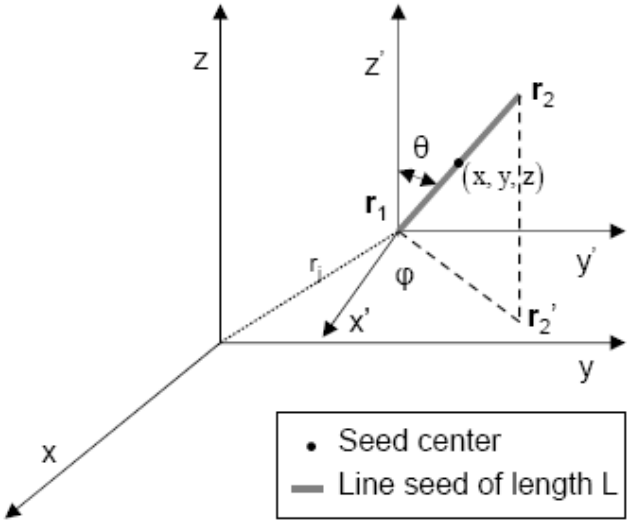


Fig.1. Elongated line seed of length, L is characterized by the seed center (black dot) positions, $(x, y, z)$ and orientation coordinates, $(\theta, \varphi)$ angle-pair in the world coordinates frame; where, *z* is the axis of implantation.

Each of the N seeds, is characterized by its centroid location, $\mathbf{r}_k$, direction cosines, $\mathbf{\Omega}_k$ describing the k-*th* seed axis orientation, and radiographically visible length, *L*. The direction cosine vector is related to the original pose variables $(\theta, \varphi)_k$ in the world coordinate system by,

$$\mathbf{\Omega}_k = (\sin\theta\cos\varphi, \sin\theta\sin\varphi, \cos\theta)_k \quad (1)$$

The endpoint coordinates of the seed marker are denoted by $\mathbf{r}_{2,k}$ and $\mathbf{r}_{1,k}$, where $|\mathbf{r}_{2,k} - \mathbf{r}_{1,k}| = L$, so that: $\mathbf{r}_{2,k} = (L/2)\cdot\mathbf{\Omega}_k + \mathbf{r}_k$ and $\mathbf{r}_{1,k} = -(L/2)\cdot\mathbf{\Omega}_k + \mathbf{r}_k$. In this study, we used either the Model 6711 $^{125}$I seed which has a 3.0 mm × 0.5 mm cylindrical radio-opaque marker for 6711, giving an $L$ = 3 mm or machined stainless steel cylinders of 0.8 mm × 4.5 mm having an $L$ = 4.5 mm. In general, each seed can be represented by a locus of points in the CBCT rotated and translated projection frame, such that, $\{\mathbf{r}'\}_k = \{\mathbf{r}' \,|\, \mathbf{r}' = \mathbf{r}_k + \eta\mathbf{\Omega}_k,\ \eta \in [-L/2, L/2]\}$. In practice, the Bresenham line drawing

algorithm[30] is used to represent each seed by a finite set of Q equally-spaced points to represent the seed in the world coordinate frame, such that,

$$\left\{\mathbf{r}'\right\}_k = \left\{\mathbf{r}'_{jk} \mid \mathbf{r}'_{jk} = \mathbf{r}_k + \left(\left(j-1\right)\cdot\delta l_k - L/2\right)\cdot\boldsymbol{\Omega}_k,\ j=1,\cdots,Q\right\} \tag{2}$$

where, $\delta l_k = L/\left(Q-1\right)$ is the interval between two adjacent points and $\left(\left(j-1\right)\cdot\delta l_k - L/2\right) = L_k$ represents the total length of the *k-th* seed.

Each member of $\left\{\mathbf{r}'\right\}_k$ projects onto the detector plane defined by gantry angle γ with coordinates $\left(u'_{jk}, v'_{jk}\right)_\gamma$ in each rotated and translated image plane. Then, we obtained the initial estimate of the computed binary image intensity, $I_0\left(u,v \mid \left\{\mathbf{r}_k, \boldsymbol{\Omega}_k\right\}, \gamma\right)$ which is set to unity for all detector pixels $\left(u,v\right)$ containing a projected point from the set $\left\{\mathbf{r}'\right\}_k$ and zero elsewhere. More explicitly, the digitized line seed image pixels intensity is given by,

$$I_0\left(u,v \mid \left\{\mathbf{r}_k, \boldsymbol{\Omega}_k\right\}, \gamma\right) = \begin{cases} 1 & \text{if } \exists\, j,k \text{ such that } P_\gamma\left(\mathbf{r}_{j,k}\right) \in \left(u,v\right),\ 1 \le j \le Q,\ 1 \le k \le N \\ 0 & \text{if not.} \end{cases} \tag{3}$$

where, $P_\gamma\left(\mathbf{r}\right) = \left(u'_k, v'_k\right)_\gamma$ are the coordinates of the point $\mathbf{r}$ in the detector plane for a gantry angle of $\gamma$ and $\left\{\mathbf{r}_k, \boldsymbol{\Omega}_k\right\}$ denotes the set of *N* seed centroids and direction cosines.

The projected seeds on the detector plane were dilated one pixel along each direction, yielding a line segment of uniform brightness and thickness *t*, which is approximately equal to the width of the shadow cast by a Model 6711 $^{125}$I 0.5 mm diameter radiographic marker. This ensured that each computed binary seed projection had approximately the same shape and size as binary seed images segmented from experimentally acquired projections. In our notation, the index j is dropped because after projecting the points corresponding to a line seed, it was represented by a line segment of uniform intensity on the 2D detector plane. The binary mask representation of the projected line seed was then blurred by convolving it with a 2D Gaussian blurring

function with a standard deviation σ. For a set of *N* line seeds projected from the world frame then the total computed image is,

$$I_c\left(u,v\,|\,\{\mathbf{r}_k,\boldsymbol{\Omega}_k\},\sigma,\gamma\right)=\sum_k\sum_{u_k',v_k'} I_0\left(u_k',v_k'\,|\,\mathbf{r}_k,\boldsymbol{\Omega}_k,\gamma\right)\exp\left[-\left(u-u_k'\right)^2/2\sigma^2-\left(v-v_k'\right)^2/2\sigma^2\right] \quad (4)$$

where, $\left(u-u_k'\right)$ and $\left(v-v_k'\right)$ denote the distances between the corresponding pixel centers. The main purpose of the Gaussian blurring is to create a continuous-value grayscale image to which a gradient-driven iterative search process can be applied. In the absence of any blurring on the images, large areas of the intensity map would have zero intensity, providing no gradient to guide the similarity minimization search. The blurring creates a "source attractive" potential well around each seed with tails extending beyond the seed footprint, causing computed seed images to be pulled towards measured seed images, and accelerating the convergence of the iterative minimization search.

The metric sum-of-squared-differences (*SSQD*), which describes the "similarity" between all grayscale images, $I_c\left(u,v\,|\,\{\mathbf{r}_k,\boldsymbol{\Omega}_k\},\sigma,\gamma\right)$ of a candidate set of the seed poses $\{\mathbf{r}_k,\boldsymbol{\Omega}_k\}$ and the corresponding experimentally acquired or "measured" images, $I_m\left(u,v\,|\,\sigma,\gamma\right)$ at nominal gantry angle γ, is given by,

$$SSQD\left(\{\mathbf{r}_k,\boldsymbol{\Omega}_k\}\,|\,\sigma,\gamma\right)=\sum_\gamma\sum_{u,v}\left[I_c\left(u,v\,|\,\{\mathbf{r}_k,\boldsymbol{\Omega}_k\},\sigma,\gamma\right)-I_m\left(u,v\,|\,\sigma,\gamma\right)\right]^2 \quad (5)$$

The seed pose parameters, $\{\mathbf{r}_k,\boldsymbol{\Omega}_k\}$ were iteratively adjusted by simultaneously adjusting the seed poses and the imaging viewpoint parameters relative to the first projection[28,29] (i.e., the reference viewpoint, which is not allowed to vary; other imaging viewpoints are defined relative to the first projection in terms of rotation and translation) and then computing updated $I_c\left(u,v\,|\,\{\mathbf{r}_k,\boldsymbol{\Omega}_k\},\sigma,\gamma\right)$. By allowing the projection viewpoints to vary, we were able to correct for imprecision in the measured gantry positions and thereby obtain a more precise projection match. The parameter adjustments were calculated from the first derivatives of *SSQD* with respect to each degree of freedom. For example, the derivative with respect to the x-coordinate of the *k-th* seed was computed as follows;

$$\partial\left(SSQD\right)/\partial x_k = 2\sum_{\gamma}\left(\sum_{u,v}\left[I_c\left(u,v\,|\,\{\mathbf{r}_k,\boldsymbol{\Omega}_k\},\sigma,\gamma\right)-I_m\left(u,v\,|\,\sigma,\gamma\right)\right]\,\partial I_c\left(u,v\,|\,\{\mathbf{r}_k,\boldsymbol{\Omega}_k\},\sigma,\gamma\right)/\partial x_k\right) \quad (6)$$

Because the image grayscale intensities are represented entirely by the Gaussian blurring function, the grayscale image gradient, $\partial I_c\left(u,v\,|\,\{\mathbf{r}_k,\boldsymbol{\Omega}_k\},\sigma,\gamma\right)/\partial x_k$ for each seed was calculated analytically from equation (4) for that degree of freedom. Similarly, we computed the first derivatives of *SSQD* with respect to the other spatial and angular coordinates. Detailed derivations of the gradient calculation can be found in the appendix.

After computing the analytical gradients to adjust all free parameters, the process iteratively refined the 3D seed's pose and each imaging viewpoint parameter (except first projection) until the computed projections optimally matched the measured projections of the seed geometry. The computed and measured projections must have the same imaging geometry, image size and pixel resolution. At least two, but preferably three or more pairs of computed and measured projections with corresponding imaging geometry are required for a stable reconstruction process. The 5*N* seed pose plus 6 (*M* -1) degrees of freedom for the relative viewpoints (i.e., excluding the first fixed projection) are the freely moveable parameters in each iteration, where, *M* is the total number of projections.

To iteratively adjust the free parameters, leading to the minimization of *SSQD*, we used a nonlinear gradient search method[28,29] that combined a steepest descent gradient search with a parabolic approximation of the *SSQD* surface around the global minimum.

For overlapping clusters and highly migrated seeds, it was observed that the computed seed pose at convergence varied somewhat with initial starting configuration. This indicated less than optimal convergence matching. For example, if the initial seed position estimates are far from the measured configuration, the gIFPM algorithm may not converge to an optimal configuration. To improve the accuracy in such settings, we applied a two step adaptive blurring scheme in which a larger 2D Gaussian blurring (i.e., $\sigma_1$) was used for the initial iterations. The output of the first-step convergence was taken and used as an initial estimate with a reduced gaussian spreading (i.e., $\sigma_2$) for the remaining iterations. The two-step blurring strategy used a more diffuse computed image

with larger capture range in the beginning to draw the computed seeds closer to the measured ones and then increased the sharpness of the computed image to improve accuracy at the final convergence. The optimal values of two-step blurring, $\sigma_1$ and $\sigma_2$ were obtained from trial and error for each seed configuration and were between (3.0 – 2.2) mm and (2.0 – 1.4) mm, respectively.

**B. Validation via simulated implant geometries**

The numerical simulation studies used computational models of configurations of 56 to 70 elongated line seed sources in 3D space. Clinically realistic initial estimates of the seed configuration and synthetically- produced projections were obtained from patient pre-plans based upon a pre-treatment ultrasound volume study, which give the centroid coordinates $\{\mathbf{r}_k\}$ relative to the planning target volume (PTV) for each patient. Since our gIFPM algorithm used the CBCT reference frame, the ultrasound-based preplan coordinates were transformed to the CBCT coordinate system by using rotation, translation and scaling.

Then line seeds of length $L$ (3.0 mm × 0.5 mm cylindrical radio-opaque marker of Model 6711 $^{125}$I seed) were centered at the transformed $\{\mathbf{r}_k\}$ centroid coordinates and aligned with the axis of implantation (i.e. $\theta = 0, \varphi = 0$) which we called the "straight seed" implant. This was our initial estimate of the implant seed configuration. The 3D position of each seed in the configuration was shifted by a displacement, $\boldsymbol{d}_k$ randomly sampled from the uniform distribution [-2 mm, 2 mm] in each of the three directions, resulting in a mean displacement of 1.98 mm. The $\theta$ and $\varphi$-values were randomly sampled from the uniform [-π/6, π/6] and [-π/2, π/2] distributions, respectively. To simulate migrated seeds in the implant, we manually adjusted the 3D pose of a few seeds after perturbing the configuration. These configurations were used to compute three "synthetic measured" projection images, i.e., projections of the configuration that we wished to determine. The source to isocenter distance was 100 cm and source to detector distance was 150 cm. The images were 288 × 288 pixels square and had a resolution of 0.388 mm/pixel.

The accuracy of each trial was quantified by calculating the root-mean-square (RMS) difference and the standard deviation between the estimated and known 3D seed poses.

**C. Validation via physical phantoms**

A validation phantom (see Figure 2) was designed and fabricated from eight interchangeable 9.5 cm × 9.5 cm × 0.6 cm acrylic slabs, allowing up to 100 decayed Model 6711 $^{125}$I seeds to be placed at known locations and orientations. Each slab, which represents a single plane of seeds, contains 10 mm diameter removable cylindrical plugs, each of which can contain a single dummy seed. The position and polar orientation, $\theta$, of each seed are determined by the location and angle (with respect to plug rotational axis) of the seed cavity created by a digital milling machine. The azimuthal angle $\varphi$ can be controlled by rotating the plug within its slab and is quantified by means of an angular scale [see Figure 2 (a)]. Because plugs and planes are interchangeable, one can realize many different seed configurations. The seeds were arranged in rectilinear layers separated by 6 mm, with 6 mm to 10 mm interseed (center-to-center) spacing within each slab. Up to 10 clusters of as many as 5 seeds were physically modeled in the implants (for example, see Figure 3) in order to test the robustness of gIFPM in the presence of both clustered and non-overlapping seeds. The slabs are held in rigid configuration by placing them inside a hollow acrylic rectangular box designed for this purpose [see Figure 2 (b)] prior to scanning. The positional accuracy of the known 3D seed centroids of the precision-machined phantom was +/-0.1 mm in each of the three directions and about 1$^{o}$ angular accuracy for the $\theta$ and $\varphi$ angle-pair.

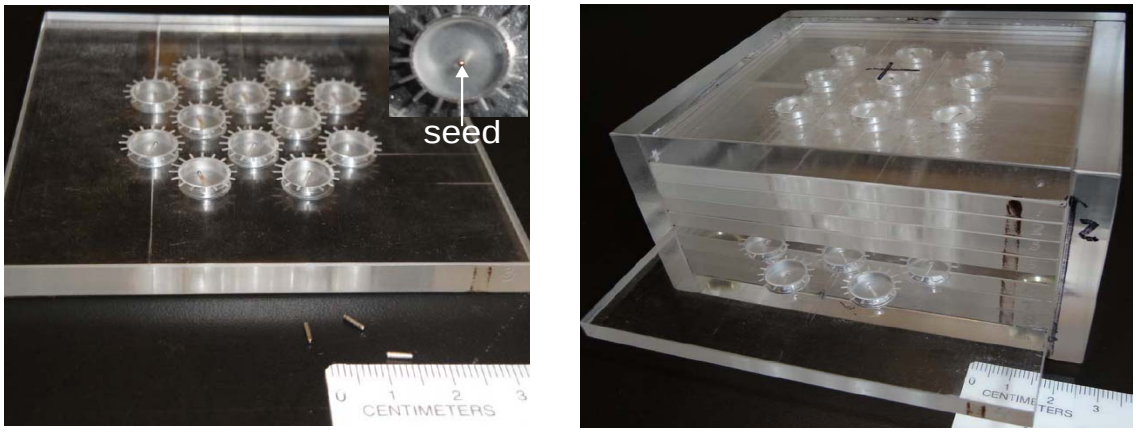


(a) (b)

Fig.2. Close-up photographs, (a) an acrylic slab of the phantom containing Model 6711 $^{125}$I seeds; where the polar angle $\theta$ is defined as the angle between implant axis and the major axis of the seed. It was assigned across the slab at different orientation for each seed (see inset). The azimuthal angle, $\varphi$ was assigned by using the adjustable reference grid drawn for each seed in known orientation, and (b) multi-configuration precision-machined phantom assembly with all 8 replaceable slabs. This phantom was used to create different seed configurations to test the gIFPM algorithm seed localization accuracy in the clinical setting.

Initial estimates of each seed configuration were obtained by randomly perturbing the known 3D seed configuration, as described earlier. The initial estimates of $\theta$ and $\varphi$-values were also randomly sampled from the uniform [-π/6, π/6] and [-π/2, π/2] distributions, respectively. To make the computed projection images, the perturbed seeds configuration was rotated and translated to each imaging viewpoint and then projected on the $(u,v)$ detector planes. The seed centroids were transformed to obtain extended line seeds before making projections as described in § II (A).

In this study, three clinically realistic brachytherapy seed configurations containing totals of 50, 72 and 76 seed datasets were realized on the phantom. For the 50 seed case, decayed Model 6711 $^{125}$I seeds obtained from Oncura Inc. were used. In that case, we modeled only 3 mm radio-graphically visible radio-opaque marker. For the remaining cases, machined stainless steel cylinders (4.5 mm long by 0.8 mm in diameter) were used.

**D. Acquisition and processing of radiographic projections**

To experimentally validate this algorithm, the phantom was imaged on a Varian ACUITY imaging system which is used for performing image-guided brachytherapy insertions in our dedicated brachytherapy suite. The Acuity system can be operated in CBCT, fluoroscopic, or radiographic mode. CBCT images of the phantom were acquired for a complete gantry rotation around the phantom capturing approximately 660 projections through $360^{o}$ using a Varian 4030CB flat panel detector (FPD). The detector is 40 cm × 30 cm with a 1024 × 768 image size and pixel resolution of 0.388 mm/pixel and a 16-bit depth. The ACUITY imaging geometry consists of a 100 cm source to isocenter distance and a 150 cm source to detector distance. Three to ten radiographic projections at $5^{o}$ to $10^{o}$ angular intervals were selected from the full set CBCT x-ray projections between $\pm 30^{o}$ gantry angles. The choice of perspectives was based on maximizing visibility of the implanted seeds in the projections and avoiding excessively small parallaxes.

The post-processing involved a) cropping the images to 288 × 288 pixels square; b) normalizing the image intensity by finding its maximum and minimum values in the image; c) morphological top-hat-filtering to suppress the background; and d) automatic thresholding using the 3-standard deviation value of the pixel intensity histogram to create binary line-seed images in each projection in order to separate the seeds from the background. This process resulted in binary bitmap images with zero intensity in the background and intensity 1 over the area of each projected line seed.

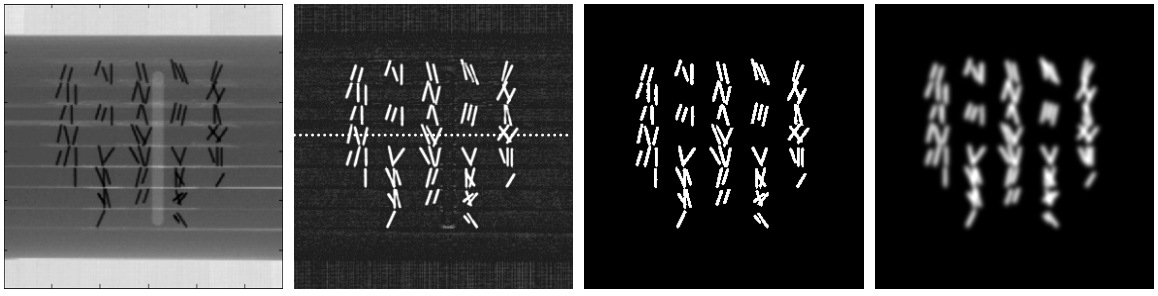


Fig.3. An example case of the image post-processing of the projection images obtained from the Varian 4030CB digital simulator, (a) raw projection image, (b) filtered image, (c) binary seed only bitmap image, and (d) blurred grayscale image using the gIFPM algorithm for 76 seed phantom datasets.

The gIFPM method does not require transforming cylindrical seed images into point-like landmarks. Instead we match elongated line-seed features in the 2D images including overlapping seed clusters. This avoids a major difficulty encountered by back-projection methods: resolving seed clusters and isolating each seed centroid before reconstruction. The binary images were then convolved with the same 2D Gaussian blurring function that is used for the computed projection to create diffuse elongated seed lines with a known intensity distribution. This produces smoothly-varying grayscale image gradients that can be calculated analytically in the computed projections to guide towards minimization of the objective function, *SSQD* and speed up the convergence of the matching process. An example case of image post-processing is shown in Figure 3.

**E. Assessment of the seed reconstruction/ registration error**

In the simulated implant study, the accuracy of each trial was quantified by calculating the root-mean-square (RMS) difference and the standard deviation between all estimated and true/synthetic measured 3D pose parameters.

For the phantom studies, the seed reconstruction error was quantified in three ways. First, the seed reconstruction error was computed by directly comparing the computed seed coordinates with the known seed poses obtained from the precision-machined phantoms. In the second approach, the seed registration error was evaluated by re-projecting the gIFPM line seed pose at convergence onto the 2D image planes, overlaying the computed and measured seed projection, and calculating the nearest-neighbor difference between the measured and computed seed poses in each image plane. In this approach, for all non-clustered computed seed images, we empirically calculated the seed centroids (center of mass of each seed region) and orientation angles (angle between the x-axis and the major axis of each seed) in each 2D image plane and compared with those obtained from the measured seed images at convergence.

In the third approach, we compared the gIFPM positional coordinates to those obtained by the VariSeed planning 8.0 software (Varian Medical System, Palo Alto, CA) operating on the CBCT dataset reconstructed from the same set of projections from

which the gIFPM measured projections were selected. VariSeed automatic seed finder tool was used. Since VariSeed frequently detected more seeds than were actually implanted, manual corrections were performed to estimate the approximate seeds locations. As VariSeed does not provide the individual seed orientations coordinate, we compared only the seed centroids. Accuracy was quantified in terms of the minimum 3D distance between each gIFPM seed centroid position and the nearest VariSeed seed location. The seed reconstruction error was quantified by computing the vector and scalar displacement between the gIFPM and VariSeed positions. VariSeed seed centroids have limited accuracy due to the CT partial volume artifacts, metal streaking artifacts, and difficulty in resolving overlapping seed clusters. These uncertainties were included in our estimation of the accuracy of the gIFPM solution for the seed positions.

## III. RESULTS

### 1. Simulated implants

In Figure 4 we illustrate an example, of the iterative matching process for a simulated implant consisting of 60 seeds. The three projections have gantry angles of 0°, ±30°. The initial seed configuration was obtained from a patient's pre-procedure planned implant geometry assuming the seed axes to be parallel to the gantry axis. Comparison of the final computed images 4 (c) to the measured images (d) shows excellent agreement, including reproducing overlapping seed clusters which appear as brighter and/or extended seed group image features. The gIFPM algorithm successfully found seeds that were placed as far as 5 mm from their pre-planned positions. This case required 11 iterations in the 1$^{st}$ step (gaussian width, $\sigma_1$ = 2.8 mm) with computation time of about 12 min/iteration and 4 iterations in the second step ($\sigma_2$ = 1.8 mm), with computation time of about 16 min/iteration on 1 GHz processor (computation time depended upon number of seeds used in the implants, i.e., the number of free parameters to optimize in each iteration).

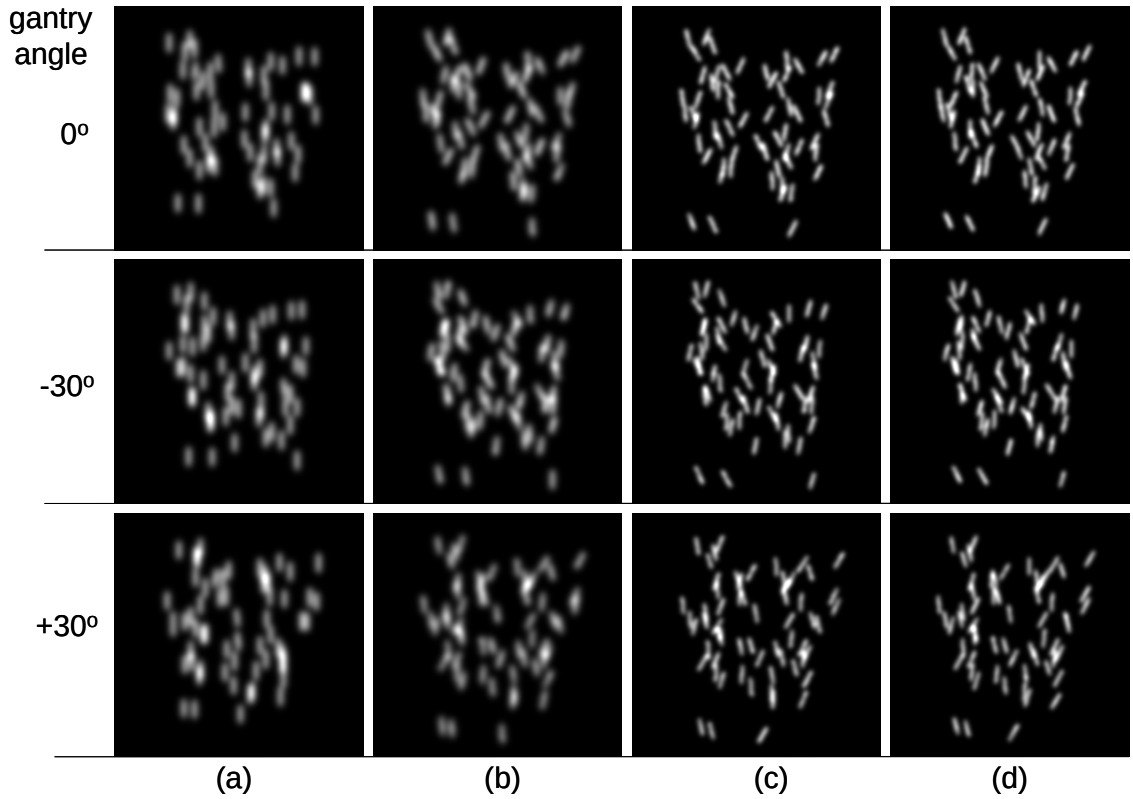


Fig.4. An illustration of the convergence process for a 60 seed simulated implant, (a) initial estimated seed configuration with "straight seeds" derived from a patient pre-plan, (b) computed images after convergence with $\sigma_1$ = 2.8 mm, (c) computed images after convergence with $\sigma_2$ = 1.8 mm and using poses (b) as the initial configuration; and (d) the true/synthetic measured images, where the rows represent different gantry angles. The gIFPM algorithm was able to reproduce orientation of each individual seed including overlapping clustered and highly migrated seeds.

Figure 5 shows the convergence of the objective function score for the four simulated patient implants, where the black arrow indicates the plateau regions of the similarity when switching from first step to second step iterations. Similar transitions can be seen for the other patient cases convergence histories. For the 60 seed test case, from one-to-one correspondence between the true/synthetic measured and computed sets of seed coordinates, the gIFPM absolute accuracy was (0.53 ± 0.43) mm for position and (3.7 ± 2.7)° and (4.4 ± 3.8)° for polar and azimuthal angles, respectively. Figure 6 shows the histograms of the seed localization errors. More than 98% of the reconstructed seed positions are within 1 mm of their true positions, and more than 95% of the reconstructed seed orientations are within 5° of their true orientations.

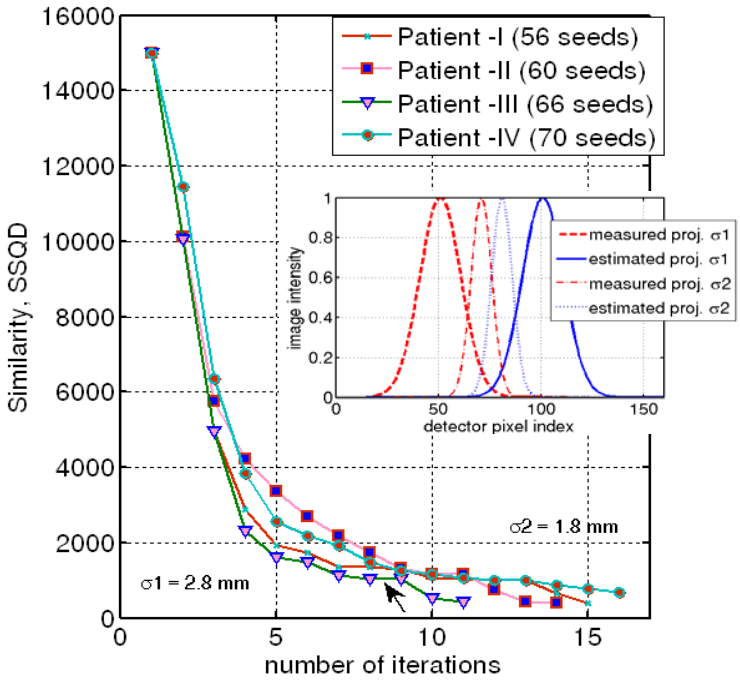


Fig.5. The similarity metric score vs. iteration number for the two step gIFPM algorithm for the four simulated patient cases: 56, 60, 66, and 70 seed configurations. The transition from larger to smaller blurring for the 66 seed configuration is shown by the black arrow. The one-dimensional image-intensity profiles in the inset illustrate the difference in capture range for the two blurring levels.

Several experiments were performed to test the accuracy and robustness of the gIFPM algorithm, including arranging the seed geometry to simulate seed clusters and overlaps of increasing complexity in more than one or more projections, e.g., 2, 3 or seeds overlapping in one or more than one projection, etc. Figure 4 illustrates successful resolution of more than 4 seed clusters consisting of up to 5 seeds in the cluster on more than one projection. We found that gIFPM could accurately determine seed poses with clusters consisting of as many as five seeds. Table I summarizes the accuracy of gIFPM reconstructions for four simulated implants derived from patient cases. In all cases, the RMS seed position error was less than 0.7 mm and the maximum error did not exceed 1.5 mm. The RMS orientation errors were found to be about $5^{o}$ for the both angular coordinates.

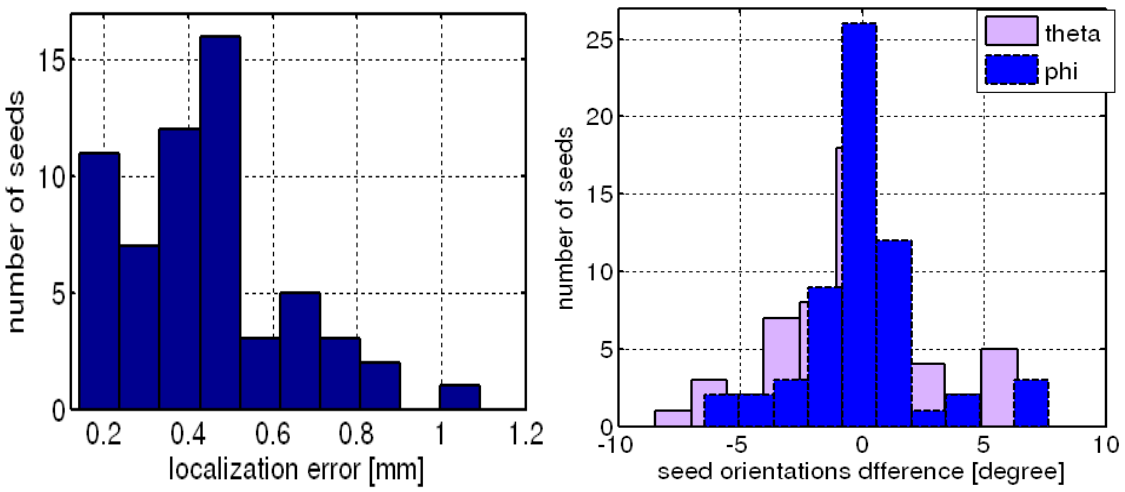


(a) (b)

Fig.6. Histograms of the seed localization error for the 60 seed simulated patient configuration, (a) positional error in terms of 3D distance between reconstructed and true location, and (b) orientation error. The gIFPM absolute accuracy was (0.53 ± 0.43) mm for position, and (3.7 ± 2.7)° and (4.4 ± 3.8)° for $\theta$ and $\varphi$ angles, respectively.

**Table I.** Accuracy of gIFPM reconstructed poses for 4 simulated implants derived from patient pre-plans. The root-mean-square (RMS) value and standard deviation for the positional and orientation coordinates are reported. The maximum displacement (Max. error) of the seed position is also reported.

| Patient # (No. of seeds) | Gantry angles (°) | Total no. of iterations | gIFPM vs. true seed pose | | | |
|---|---|---|---|---|---|---|
| | | | RMS error in seed position (mm) | Max. error (mm) | RMS error in seed orientation (°) | |
| | | | | | $\theta$ | $\varphi$ |
| I (56) | 0<br>+20<br>-20 | 15 | 0.63 ± 0.45 | 1.32 | 4.4 ± 3.2 | 5.3 ± 3.1 |
| II (60) | 0<br>-30<br>+30 | 14 | 0.53 ± 0.43 | 1.19 | 3.9 ± 2.7 | 4.4 ± 3.8 |
| III (66)* | 0<br>-20<br>+20 | 11 | 0.68 ± 0.54 | 1.46 | 5.2 ± 5.7 | 5.8 ± 5.3 |
| IV (70) | 0<br>+30<br>-30 | 16 | 0.65 ± 0.52 | 1.38 | 6.0 ± 2.8 | 6.2 ± 3.2 |

* Two extra seeds in the pre-plan

Figure 7 illustrates the convergence process for Table I Case III in which ambiguities are created by incomplete (two seeds missing from the true implant but present in estimate) and excessive (one additional seed-like artifact in the measured projections with no counterpart in the computed images) data. Figure 7 (d) shows that in both cases that the two-step iterative convergence process closely reproduces the measured seed projections. However, the gIFPM algorithm converged robustly to an optimal solution of the seed configuration that was only slightly perturbed in the region adjacent to the additional or missing seed images. Since difference images readily identify the additional and/or missing seeds, gIFPM could be rerun with a modified initial configuration having the correct number seeds and/or seed-like objects, which would slightly improve reconstruction accuracy.

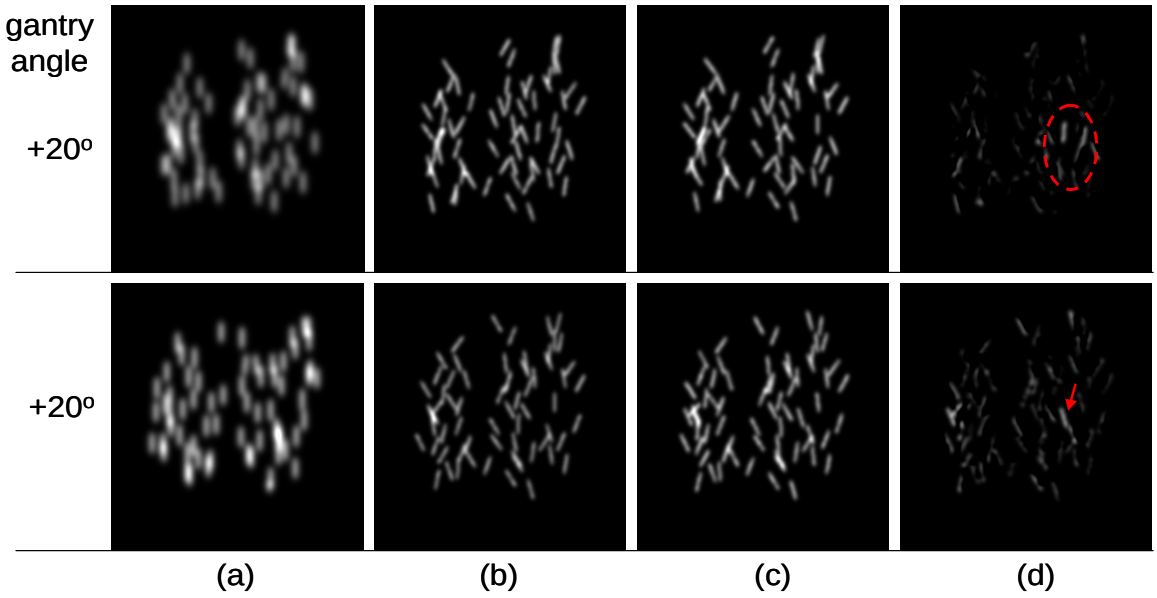


Fig.7. Illustration of gIFPM seed reconstruction for simulated case III in Table I for a single projection. In the first row (+20°), 66 seeds are present in the simulated implant derived from the preplan but 68 are assumed in the initial seed configure, (a) with seed axes parallel to the gantry axis. In the second row (+20°), 66 seeds are present both in the initial estimated configuration and in the simulated implant along with an additional seed-like artifact which is present in the measured images, (a) initial estimate of the seed configuration, (b) computed images at final convergence, (c) the synthetic measured images corresponding to the "true" seed configuration, and (d) difference between images (b) and (c). The red arrow and ellipse in (d) indicates the extra seed(s) found by gIFPM at convergence.

**2. Validation test with phantoms**

Physical phantoms with different seed configurations were imaged in order to evaluate the gIFPM algorithm in a more clinically realistic setting. Figure 8 shows the convergence of the objective function for the three example seed configurations derived

from the same phantom; where the black arrow indicates the plateau region where the algorithm transition from the larger to smaller Gaussian width.

**Table II.** Accuracy of seed poses deduced by the gIFPM algorithm for three seed configurations realized by our physical phantom and imaged on the VCU ACUITY system. The root-mean-square (RMS) value and standard deviation for the positional and orientation coordinates are reported while using 3 vs. 6 experimentally acquired projections. The maximum displacement (Max. error) of the seed position is also reported.

| No. of seeds | No. of projections | Total no. of iterations | gIFPM vs. true seed pose | | | |
|---|---|---|---|---|---|---|
| | | | RMS error in seed position (mm) | Max. error (mm) | RMS error in orientation ($^o$) | |
| | | | | | $\theta$ | $\varphi$ |
| 76** | 3 | 19 | 0.78 ± 0.57 | 1.88 | 5.7 ± 4.9 | 6.0 ± 4.1 |
| | 6 | 21 | 0.67 ± 0.47 | 1.56 | 4.6 ± 3.6 | 4.5 ± 3.3 |
| 72** | 3 | 17 | 0.72 ± 0.48 | 1.74 | 5.0 ± 3.8 | 5.7 ± 3.3 |
| | 6 | 18 | 0.56 ± 0.52 | 1.37 | 3.8 ± 2.9 | 4.2 ± 3.7 |
| 50* | 3 | 15 | 0.75 ± 0.46 | 1.78 | 4.9 ± 3.3 | 5.3 ± 3.8 |
| | 6 | 16 | 0.59 ± 0.42 | 1.44 | 3.2 ± 2.8 | 4.3 ± 2.9 |

** Line seed made up of stainless steel (4.5 mm long and 0.8 mm in diameter)
* Actual Model 6711 $^{125}$I dummy seed (3.0 mm × 0.5 mm radio-opaque marker)

As shown in Table II and Figure 9, the phantom study shows good agreement between the generalized IFPM and the known seed coordinates realized by the phantom. Table II shows RMS reconstruction errors ranging from 0.56 mm to 0.78 mm with angular coordinate RMS errors ranging from 3° to 6°. These errors are only slightly larger than those of the idealized simulated implant study, indicating that the additional errors associated with determination of the seed poses in the phantom and Acuity forward-projection modeling errors are not significant. Increasing the number of projections from 3 to 6 reduced these errors by approximately a factor of $\sqrt{2}$ at the cost of doubling computation time. For the 76 seed phantom case, from one-to-one correspondence

between the two sets of seed coordinates, the RMS error was (0.78 ± 0.57) mm. The θ and φ angle distributions were found to be (5.7 ± 4.9)° and (6.0 ± 4.1)°, respectively when using three projections. The seed reconstruction error is reported in the histograms of Figure 9 (a) show that 97% of the reconstructed seed positions are within 1.5 mm from the measured seed locations, and (b) 95% of the reconstructed seed orientations are within 8° of their known orientations.

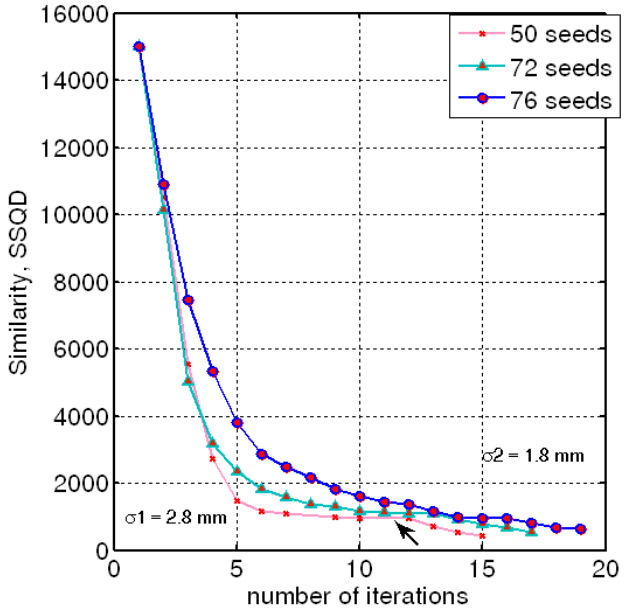


Fig.8. The similarity metric score vs. iteration number for the two-step gIFPM algorithm for the three example physical phantom seed configurations. The transition from larger to smaller blurring filter for the 50 seed configuration is highlighted by the black arrow.

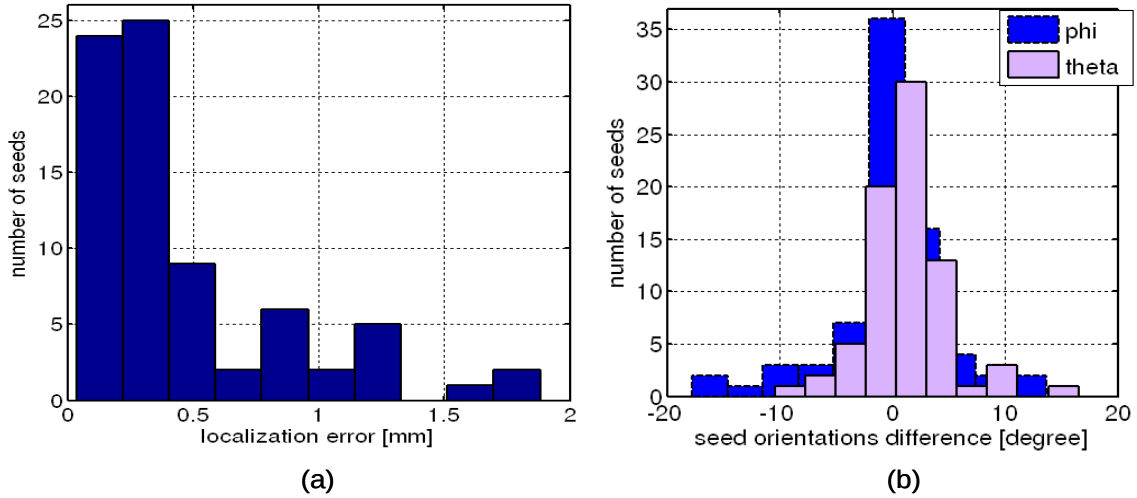


Fig.9. Histograms of the seed localization error in 3D space between reconstructed and true pose for the 76 seed phantom configuration for three projection images, (a) positional error, and (b) orientation error. The RMS error was found to be (0.78 ± 0.57) mm for position. The $\theta$ and $\varphi$ angle distributions were found to be (5.7 ± 4.9)° and (6.0 ± 4.1)°, respectively.

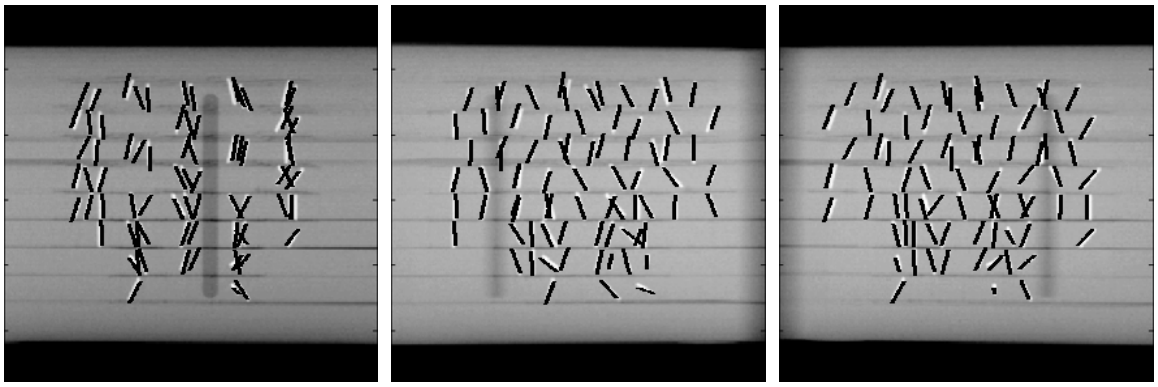


Fig.10. Superposition of measured (white) and computed (black) line seed images projected on the detector planes for gantry angles of (a) +5°, (b) -20°, and (c) +20° for 76 seed phantom configuration. While many computed seeds coincided exactly with the measured ones, a few still reveal small discrepancies.

An example of the reconstructed seed configurations projected onto the imaging planes is presented in Figure 10. For the subset of seed images that do not overlap, the residual 2D RMS error in computed vs. measured seed images were 0.69 ± 0.55 mm (+5 degree), 0.83 ± 0.56 mm (-20 degree), and 0.79 ± 0.58 mm (+20 degree) for nearest-neighbor displacement and 5.6 ± 3.7° (+5 degree), 6.9 ± 6.2° (-20 degree), and 6.7 ± 5.1° (+20 degree), respectively, for polar angle. This indicated very good agreement between measured and computed seed images.

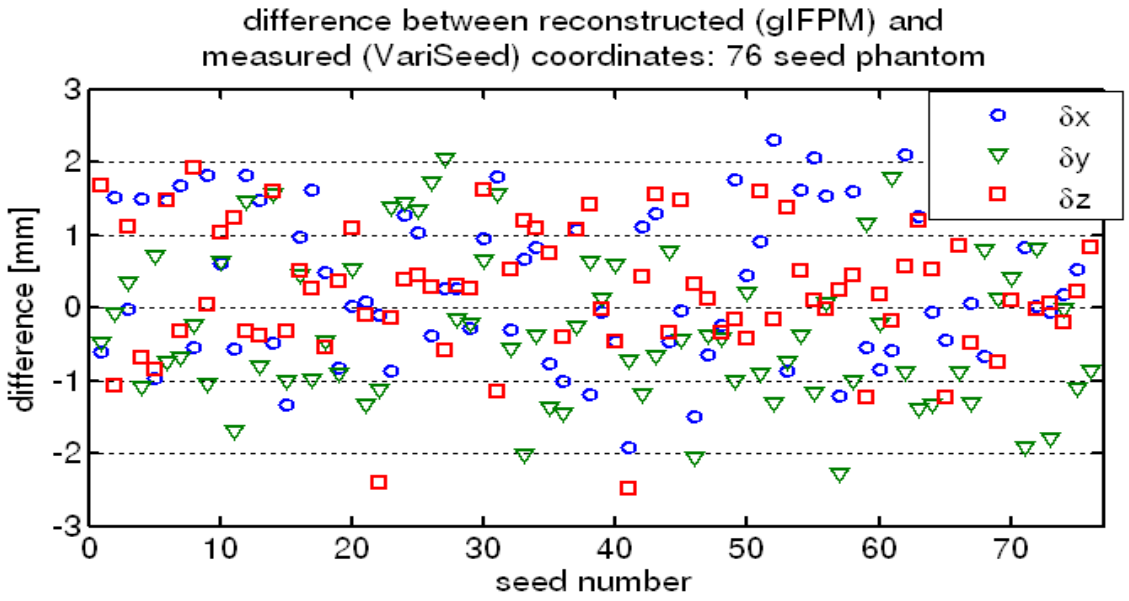


Fig.11. Seed-by-seed vector difference between gIFPM positions and those obtained from the VariSeed planning system for 76 seed phantom datasets. The 3D RMS error was (1.69 ± 0.63) mm.

Figure 11 shows the seed-by-seed vector displacement between gIFPM and VariSeed coordinates. The mean (and RMS) values along the x, y, and z directions were found to be 0.39 ± 1.02 mm (0.87 ± 0.54 mm), -0.27 ± 1.06 mm (0.90 ± 0.52 mm), and 0.35 ± 0.98 mm (0.72 ± 0.48 mm), respectively. The 3D RMS error was 1.69 ± 0.63 mm. This level of agreement seems reasonable given uncertainties in VariSeed centroid localization due to metal streaking artifacts, partial volume averaging, and finite CT slice width.

## IV. DISCUSSION

A novel IFPM algorithm has been successfully extended to the more complex five degrees-of-freedom problem of reconstructing the 3D pose, as well as centroid, of radio-opaque cylindrically symmetric implanted objects such as implanted brachytherapy seeds from a limited number of radiographic projections. IFPM approach does not require solution of the challenging NP3 seed image matching problems unlike standard BP methods. It avoids the intra- and inter-observer variability in localizing seeds that is frequently observed on three-film methods.[9-16] This method also allows the imaging viewpoints for the digitally reconstructed radiographs (DRRs) to be free parameters to adjust gantry angle uncertainties relative to the first projection. In addition, a novel precision-machined prostate seed implant phantom, capable of realizing multiple seed configurations with an accuracy of 0.1 mm, was developed for rigorously testing the new algorithm.

Several algorithms are available for reconstructing 3D seed pose, including seed orientation, from measured 2D projections.[19-20, 38-39] The algorithms presented by Tubic *et al.*[19-20] use mathematical morphology to detect the center of the seeds as well as their orientation on the 2D image plane. This information (seed center and orientation in 2D) was then used to perform 3D reconstruction of each individual seed including orientation.[44] However, their method fails to correctly reconstruct seeds in large clusters of more than three seeds. Another approach, proposed by Siebert *et al.*[38], separately back-projects the tip and end positions of each seed image and uses a heuristic search algorithm to efficiently solve the NP3 matching problem. While in principle this method

identifies seed orientation, no quantitative data are shown. A promising brachytherapy seed reconstruction method using seven digital-tomosynthesis (DTS) projections has recently been applied to clinical datasets.[39] In their method, seed-only 3D binary images were obtained by back-projecting each detector pixel shadowed by an elongated seed based upon pre-reconstruction binarization of each projection. They were then able to estimate orientation by finding the major and minor axes of the each reconstructed 3D binary voxel cluster. However, their method can not distinguish between orientations of seed clusters and individual seeds. The methods discussed above all have the disadvantages of BP, including intolerance to incomplete and inconsistent data as well as difficulty of resolving overlapping clusters. By accurately modeling each elongated line seed in 3D space and iteratively finding the best solution that accounts for the measured projections, our method explicitly detects the orientation of each individual seed and is capable of reproducing overlapping seed clusters and highly-migrated seeds in the implants. By using a few CBCT projections, the gIFPM has the potential for fusion-based intraoperative brachytherapy planning.

Tubic and Beaulieu[45] have proposed a new brachytherapy seed reconstruction technique that seeks to extract seed pose by analyzing the seed projections in the raw CT sinograms rather than reconstructed CT images. Essentially, their method involves segmenting the sinusoidal trace produced by each seed and fitting a mathematical model to each trace from which the centroid (derived from centerline of trace) and orientation (modulation of trace width as a function of gantry angle) can be derived. By working with higher resolution sinograms, their method avoids the major difficulties of CT-based localization, such as limited spatial resolution due to slice thickness limitation and uncertainties created by metal streaking artifacts. Excellent results were obtained for an idealized 16 seed phantom. However, automatically segmenting the sinusoidal seed projections, especially in the presence of realistic anatomic structure and image noise, remains a significant and unsolved technical challenge. Similarly, detecting variable-width traces, quantifying trace width, dealing with seeds normal to the scanner axis, and resolving tightly bunched seed clusters also challenge this algorithm. While we have not yet applied our five degrees-of-freedom gIFPM algorithm to actual clinical data, in our

previous study[29] our relatively simple filtering and segmentation algorithms were successfully applied to anterior and oblique x-ray images of four Model 200 $^{103}$Pd seed implants.

The$^{125}$I and $^{103}$Pd seeds exhibit considerable anisotropy in their dose distributions due to their internal geometry. The "self-attenuation" by the material along the seed major axis is the main cause for the seed anisotropy. However, identification of the seed orientations on CT images is difficult primarily because of the slice thickness and voxel size limitations. To avoid this difficulty, the AAPM TG-43[31] one-dimensional point-source approximation, employing an average distance-dependent anisotropy correction, the 1D anisotropy function, is used almost universally in clinical treatment planning. This approach is valid for a multi-seed implant if all seed orientations are equally probable. However, Corbett *et al.*[26] demonstrated that the seeds are preferentially orientated along the needle directions, based upon the distribution of the polar angle, $\theta$, derived from analysis of seed projection angles on one-month post-implant anterior-posterior radiographs of ten patients. By averaging the dose over an ensemble of $^{125}$I implants with identical centroids but randomly sampled orientations from the above distributions, Corbett *et al.*[26] demonstrated that seed orientation had little effect on DVH parameters, e.g., $D_{90}$, commonly used for clinical dose specification.

However, the theoretical study presented by Prasad *et al.*[32] concluded that the actual dose rate may differ from the expected dose rate by a factor of 2 when taking account of the anisotropy of the individual seeds. In the post-implants geometry using $^{125}$I and $^{103}$Pd seed, Lindsay *et al.*[27] showed that the 1D TG-43 treatment of anisotropy resulted in significant local dose computation errors (±10% for CTV and ±5% for the rectum) compared to the more accurate 2D line-seed model which requires specification of the seed orientation. However, none of these studies had available actual seed orientations for their studies nor did they present a practical method for measuring orientation. Our five parameter model allows the individual seed position and orientation distribution to be determined for each implant. By directly measuring the individual 3D

pose of each implanted brachytherapy seed, our method allows the 3D dose distribution to be more rigorously computed using the full 2D TG-43 line-seed formalism.[31]

As reported in the literature[42] and found in our clinical experience, metallic $^{103}$Pd or $^{125}$I seeds cause moderate to severe streaking artifacts on CBCT images which introduce errors in soft-tissue segmentation, deformable image registration, and CT-based dose calculation. Accurate identification of the metal seed boundary and its orientation in the sinogram projections is very useful for suppressing such artifacts by projecting each metal seed boundary onto the sinogram so that the missing soft-tissue information can be recovered by interpolation from the surrounding soft-tissue image texture. Reconstruction of CBCT images with corrected sinogram projections can then be performed. Thus, another application of gIFPM is aiding in the accurate identification of seed traces in support of interpolative sinogram corrections. By reducing streak and associated noise propagation artifacts, significant clinical value can be added to CBCT imaging for image-guided brachytherapy.

By subtracting the measured images from the computed images at convergence, in the current version of gIFPM, one can locate extra-seed(s) in the implant. Future versions of gIFPM will automatically correct for over- and under-counted seed(s) in the implant and re-run the reconstruction process to obtain a more optimal match. More extensive investigation of the initial estimate of the seed configurations using TRUS pre-implant geometry of the actual patient will be performed to further validate this algorithm. This iterative pose search method has not been optimized for speed. Improving the computation efficiency is also an area of future development.

The data presented in this paper demonstrate that the gIFPM algorithm works effectively for seeds with radio-opaque markers having aspect ratios of 6:1 or larger. Besides the Model 6711 $^{125}$I seed, other seed models satisfying this constraint include the selectSeed[33], (Amersham 6733 seed, IsoAid Advantage, DraxImage LS-1, Source Tech Medical STM1251)[34], symmetra[35], Model 9011[36] and Best Model 2301[37] sources. Our previous work[29] demonstrated that the three degrees-of-freedom IFPM algorithm can not

accurately estimate the centroids of such elongated seeds because of the requirement that computed projections produce seed shadows that closely approximate the shape and size of the actual seed binary images. The centroid-only IFPM localization algorithm was shown to accurately reconstruct the positions of Model 200 $^{103}$Pd seeds, which contain cylindrical lead markers with a 2:1 aspect ratio. Thus, to apply IFPM reconstruction to Model 6711 $^{125}$I implants, the gIFPM is essential. The gIFPM method is further being generalized to reconstruct larger and non-cylindrically symmetric metal objects in brachytherapy treatment, e.g., intracavitary applicators (i.e., colpostats and tandem) of known but arbitrary shape from a small set of 2D x-ray projections.

## V. CONCLUSION

We have presented a new approach to brachytherapy seed localization, gIFPM able to accurately recover the orientation as well as location of individual seeds within a densely implanted volume from a limited set of measured 2D x-ray projections. By knowing the full 3D pose of each implanted seed, more rigorous Monte Carlo-based or 2D TG-43 dose calculations can be performed. Based on both physical and simulated implants, seed reconstruction errors were about 0.7 mm and 6° for $\theta$ and $\varphi$-angles. The algorithm exhibits robust performance in the presence of overlapping seed clusters, highly migrated seeds, erroneous seed count, and errors in specifying the radiographic projection geometry. By incorporating a five degrees-of-freedom search capability, the IFPM approach, which does not require matching of corresponding images on each projection, can be extended to localization of cylindrically symmetric objects, e.g. implanted fiducial markers, whose aspect ratios are 6:1 or larger. This algorithm is more robust and tolerant of incomplete data than back-projection and has the potential to make intraoperative dose reconstruction and adaptive replanning from fused TRUS images and a few quick radiographic projections feasible.

## ACKNOWLEDGMENTS

This work was supported in part by grants from Varian Medical System and the National Institutes of Health (P01 CA 116602). The authors would like to thank Virginia Gilbert

of Virginia Commonwealth University (VCU) for her continuous support of collecting data. The authors are grateful to Dr. John Ford of VCU for proof reading the manuscript.

## APPENDIX: ANALYTIC GRADIENT OF THE SIMILARITY, *SSQD* WITH RESPECT TO FIVE DEGREES OF FREEDOM OF EACH SEED

Recalling equation (2), for each line seed k, in the rotated and translated CT frame,

$$\{\mathbf{r}'\}_k = \left\{\mathbf{r}'_{jk} \mid \mathbf{r}'_{jk} = \mathbf{r}_k + \left((j-1)\cdot\delta l_k - L/2\right)\cdot\boldsymbol{\Omega}_k,\ j=1,\cdots,Q\right\} \tag{A1}$$

where, $j=1,\cdots,Q$ is a finite set of Q points spaced at interval $\delta l_k = L/(Q-1)$ that represents the *k-th* seed.

Now, rotate and translate the CT frame to the each projection coordinate system (in which z axis corresponds with its central axis), rewriting equation (A1) more explicitly,

$$\begin{Bmatrix} x' \\ y' \\ z' \end{Bmatrix}_k = [R]_{\alpha.\beta.\gamma}\left(\begin{Bmatrix} x_j \\ y_j \\ z_j \end{Bmatrix}_k + \left((j-1)\cdot\delta l_k - L/2\right)\begin{Bmatrix} \sin\theta\cos\varphi \\ \sin\theta\sin\varphi \\ \cos\theta \end{Bmatrix}_k\right) - T_{x,y,z} \tag{A2}$$

where, $[R]_{\alpha.\beta.\gamma} = \begin{bmatrix} R11 & R12 & R13 \\ R21 & R22 & R23 \\ R31 & R32 & R33 \end{bmatrix}_{\alpha.\beta.\gamma}$ is the complete rotation matrix for each image viewpoint, and $\left((j-1)\cdot\delta l_k - L/2\right) = L_k$ represents the total length of the *k-th* seed. No translation is applied, i.e., $T_{x,y,z} = 0$. The complete rotation matrix was obtained by taking the product of the three rotation matrices defined in the world coordinate system, for each image viewpoint. The line seeds in the CT frame project to the detector plane $(u,v)$ are given by,

$$\left(u'_k, v'_k\right) = M\left(z'_k\right)\left(x'_k, y'_k\right) \tag{A3}$$

where, $M_k = \left(S + D/S + z'_k\right)$ is the magnification factor, which is different for each endpoints; $S$ and $D$ are the source-to-isocenter and isocenter-to-detector distances, respectively. Since, the brachytherapy line seed has rotational symmetry around the axis of rotation; we computed one derivative per seed per degree of freedom with respect to the each seed center coordinates (note that: the index j has been dropped). From equation (4), the image grayscale gradient for *x*-degree of freedom was calculated as follows,

$$I_c\left(u,v\,|\,\{\mathbf{r}_k,\boldsymbol{\Omega}_k\},\sigma,\gamma\right)\Big/\partial x_k=\sum_k\sum_{u_k^{'},v_k^{'}}\left(I_0\left(u_k^{'},v_k^{'}\,|\,\mathbf{r}_k,\boldsymbol{\Omega}_k,\gamma\right)\Big/\sigma^2\right)\Big[\left(u-u_k^{'}\right)\partial u_k^{'}/\partial x_k + \left(v-v_k^{'}\right)\partial v_k^{'}/\partial x_k\Big].g\left(u-u_k^{'},v-v_k^{'}\,|\,\sigma\right) \tag{A4}$$

where, $g\left(u-u_k^{'},v-v_k^{'}\,|\,\sigma\right)=\exp\left[-\left(u-u_k^{'}\right)^2\Big/2\sigma^2-\left(v-v_k^{'}\right)^2\Big/2\sigma^2\right]$ and $\gamma$ is the estimate of the imaging viewpoint.

Finally, from equations (A2) and (A3), using chain rule, we get,

$$\left.\begin{aligned}\partial u_k^{'}/\partial x&=M_k\left[R11-\left(R31\right)x_k^{'}\Big/\left(S+z_k^{'}\right)\right]\\ \partial v_k^{'}/\partial x&=M_k\left[R21-\left(R31\right)y_k^{'}\Big/\left(S+z_k^{'}\right)\right]\end{aligned}\right\} \tag{A5}$$

and similarly for the *y* and *z* coordinates of each seed. The analytical gradient of the similarity, *SSQD* with respect to $\theta$-angle coordinate for each seed was calculated from equation (5) as follows,

$$\partial\left(SSQD\right)\Big/\partial\theta_k=2\sum_{\gamma}\left(\sum_{u,v}\Big[I_c\left(u,v|\{\mathbf{r}_k,\boldsymbol{\Omega}_k\},\sigma,\gamma\right)-I_m\left(u,v|\sigma,\gamma\right)\Big]\,\partial I_c\left(u,v|\{\mathbf{r}_k,\boldsymbol{\Omega}_k\},\sigma,\gamma\right)\Big/\partial\theta_k\right) \tag{A6}$$

Again, from equation (4) we computed the image grayscale gradient with respect to $\theta$-degree of freedom,

$$\partial I_c\left(u,v\,|\,\{\mathbf{r}_k,\boldsymbol{\Omega}_k\},\sigma,\gamma\right)\Big/\partial\theta_k=\sum_k\sum_{u_k^{'},v_k^{'}}\left(I_0\left(u_k^{'},v_k^{'}\,|\,\mathbf{r}_k,\boldsymbol{\Omega}_k,\gamma\right)\Big/\sigma^2\right)\Big[\left(u-u_k^{'}\right)\partial u_k^{'}/\partial\theta_k + \left(v-v_k^{'}\right)\partial v_k^{'}/\partial\theta_k\Big].g\left(u-u_k^{'},v-v_k^{'}\,|\,\sigma\right) \tag{A7}$$

Finally, from equations (A2) and (A3), using chain rule, we get,

$$\left.\begin{aligned}\partial u_k^{'}/\partial\theta_k&=M_kL_k\Big[\left(R11.\cos\theta\cos\varphi+R12.\cos\theta\sin\varphi-R13.\sin\theta\right)\\&\qquad-\left(R31.\cos\theta\cos\varphi+R32.\cos\theta\sin\varphi-R33.\sin\theta\right)x_k^{'}\Big/\left(S+z_k^{'}\right)\Big]\\ \partial v_k^{'}/\partial\theta_k&=M_kL_k\Big[\left(R21.\cos\theta\cos\varphi+R22.\cos\theta\sin\varphi-R23.\sin\theta\right)\\&\qquad-\left(R31.\cos\theta\cos\varphi+R32.\cos\theta\sin\varphi-R33.\sin\theta\right)y_k^{'}\Big/\left(S+z_k^{'}\right)\Big]\end{aligned}\right\} \tag{A8}$$

Similarly, we have computed analytical gradient of *SSQD* with respect to $\varphi$-angle coordinate of each seed.

**References**

[1]B. H. Han, K. Wallner, G. Merrick, W. Butler, S. Sutilef, and J. Sylvester, "Prostate brachytherapy seed identification on post-implant TRUS images," Med. Phys. 30, 898-00 (2003)

[2]W. S. Bice, D. F. Dubois, J. J. Prete, and B. R. Prestidge, "Source localization from axial image sets by iterative relaxation of nearest neighbor criterion," Med. Phys. 26, 1919-24 (1999)

[3]J. N. Roy, K. E. Wallner, P. J. Harrington, C. C. Line, and L. L. Anderson, "A CT-based evaluation method for permanent implants: Applications to prostate," Int. J. Radiat. Oncol., Biol., Phys. 26, 163-69 (1993)

[4]Z. Li, I. A. Nalcacioglu, S. Ranka, S. K. Sahini, J. R. Palta, W. Tome, and S. Kim, "An algorithm for automatic, computed-tomography-based source localization after prostate implant," Med. Phys. 28, 1410-15 (2001)

[5]D. H. Brinkmann and R. W. Kline, "Automated seed localization from CT datasets of the prostate," Med. Phys. 25, 1667-72 (1998)

[6]H. Liu, G. Cheng, Y. Yu, R. Brasacchio, D. Rubens, J. Strang, L. Liao, and E. Messing, "Automatic localization of implanted seeds from post-implant Ct images," Phys. Med. Biol. 48, 1191-03 (2003)

[7]Y. Yu, L. L. Anderson, Z. Li, D. E. Mellenberg, R. Nath, M. C. Schell, F. M. Waterman, A. Wu, and J. C. Blasko, "Permanent prostate seed implant brachytherapy: Report of American Association of Physicists in Medicine Task Group Vo. 64," Med. Phys. 26, 2054-76 (1999)

[8]H. Westendorp, C. J. Hoekstra, A. van't Riet, A. W. Minken, and J. J. Immerzeel, "Intraoperative adaptive brachytherapy of iodine-125 prostate implants guided by C-arm cone-beam computed tomography-based dosimetry," Brachytherapy 6, 231-37 (2007)

[9]A. Y. C. Fung, "C-Arm imaging for brachytherapy source reconstruction: Geometrical accuracy," Med. Phys. 29, 724-26 (2002)

[10]R. L. Siddon and L. M. Chin, "Two-film brachytherapy reconstruction algorithm," Med. Phys. 12, 77-83 (1994)

[11]H. I. Amols and I. I. Rosen, "A three-film technique for reconstruction of radioactive seed implants," Med. Phys. 8, 210-14 (1981)

[12]D. D. Jackson, "An automated method for localizing radioactive seeds in implant dosimetry," Med. Phys. 10, 370-72 (1983)

[13]P. J. Biggs and M. D. Kelley, "Geometric reconstruction of seed implants using a three-film technique," Med. Phys. 10, 701-04 (1983)

[14]M. D. Altschuler, P. A. Findlay, and R. D. Epperson, "Rapid accurate, three-dimensional location of multiple seeds in implant radiotherapy treatment planning," Phys. Med. Biol. 28, 1305-18 (1983)

[15]M. S. Rosenthal and R. Nath, "An automatic seed identification technique for interstitial implants using three isocentric radiographs," Med. Phys. 10, 475-79 (1983)

[16]M. D. Altschuler and A. Kassaee, "Automated matching of corresponding seed images of three simulator radiographs to allow 3D triangulation of implanted seeds," Phys. Med. Biol. 42, 293-02 (1997)

[17]L. Gong, P. S. Cho, B. H. Han, K. E. Waller, S. G. Sutlief, S. D. Pathak, D. R. Haynor, and Y. Kim, "Ultrasonography and fluoroscopic fusion for prostate brachytherapy dosimetry," Int. J. Radiat. Oncol., Biol., Phys. 54, 1322-30 (2003)

[18]W. L. Smith, C. Lewis, G. Bauman, G. Rodrigues, D. D'Souza, R. Ash, D. Ho, V. Venkatesan, D. Downey, and A. Fenster, "Prostate volume contouring: a 3D analysis of segmentation using 3DTRUS, CT, and MR," Int. J. Radiat. Oncol., Biol., Phys. 67, 1238-47 (2007)

[19]D. Tubic, A. Zaccarin, J. Pouliot, and L. Beaulieu, "Automated seed detection and three-dimensional reconstruction: I. Seed localization from fluoroscopic images or radiographs," Med. Phys. 28, 2265-71 (2001)

[20]D. Tubic, A. Zaccarin, L. Beaulieu, and J. Pouliot, "Automated seed detection and three-dimensional reconstruction: II. Reconstruction of permanent prostate implants using simulated annealing," Med. Phys. 28, 2272-79 (2001)

[21]D. A. Todor, G. N. Cohen, H. I. Amols, and M. Zaider, "Operator-free, film-based 3D seed reconstruction in brachytherapy," Phys. Med. Biol. 47, 2031-48 (2002)

[22]D. A. Todor, M. Zaider, G. N. Cohen, M. F. Worman, and M. J. Zelefsky, "Intraoperative dynamic dosimetry for prostate implants," Phys. Med. Biol. 48, 1153-71 (2003)

[23]S. Narayanan, P. S. Cho, and R. J Marks II, "Fast cross-projection algorithm for reconstruction of seeds in prostate brachytherapy," Med. Phys. 29, 1572-79 (2002)

[24]Y. Su, B. J. Davis, M. G. Herman, and R. A. Robb, "Prostate brachytherapy seed localization by analysis of multiple projections: Identifying and addressing the seed overlap problem," Med. Phys. 31, 1277-87 (2004)

[25]S. Narayanan, P. S. Cho, and R. J Marks II, "Three-dimensional seed reconstruction from an incomplete data set for prostate brachytherapy," Phys. Med. Biol. 49, 3483-94 (2004)

[26]J. F. Corbett, J. J. Jezioranski, J Crook, T. Tran, and I. W. T. Yeung, "The effect of seed orientation deviations on the quality of $^{125}$I prostate implants," Phys. Med. Biol. 44, 2785-00 (2001)

[27]P. Lindsay, J. Battista, and J. V. Dyk, "The effect of seed anisotropy on brachytherapy dose calculations using $^{125}$I and $^{103}$Pd," Med. Phys. 28, 336-45 (2001)

[28]M. J. Murphy and D. A. Todor, "Demonstration of a forward iterative method to reconstruct brachytherapy seed configurations from x-ray projections," Phys. Med. Biol. 50, 2715-37 (2005)

[29]D. Pokhrel, M. J. Murphy, D. A. Todor, E. Weiss and J. F. Williamson, "Clinical application and validation of an iterative forward projection matching algorithm for permanent brachytherapy seed localization from conebeam-CT x-ray projections," Med. Phys. 37, 5092-01 (2010)

[30]A. S. Glassner, "GRAPHIS GEMS," UK: Academic Press Limited, 98-04 (1990)

[31]M. J. Rivard, B. M. Coursey, L. A. DeWerd, W. F. Hanson, M. S. Huq, G. S. Ibbott, M. G. Mitch, R. Nath, and J. F. Williamson, "Update of AAPM Task Group No. 43 Report: A revised AAPM protocol for brachytherapy dose calculations Dose distributions," Med. Phys. 31, 633-74 (2004)

[32]S. C. Prasad, D. A. Bassano, and P. I. Fear, "Dose distributions for $^{125}$I implants due to anisotropic radiation emission and unknown seed orientation," Med. Phys. 14, 296-98 (1987)

[33]P. Karaiskos, P. Papagiannnis, L. Sakelliou, G. Anagnostopopulos, and D. Baltas, "Monte Carlo dosimetry of the selectSeed $^{125}$I interstitial brachytherapy seed," Med. Phys. 28, 1753-60 (2001)

[34]M. J. Rivard, W. M. Butler, L. A. DeWerd, M. S. Huq, G. S. Ibbott, A. S. Meigooni, C. S. Melhus, M. G. Mitch, R. Nath, and J. F. Williamson, "Supplement to the 2004 update of the AAPM Task Group No. 43 Report," Med. Phys. 34, 2187-05 (2007)

[35]H. Hedtjarn, G. A. Carlsson, and J. F. Williamson, "Monte Carlo-aided dosimetry of the symmetra model I25.S06 $^{125}$I, intestinal brachytherapy seed" Med. Phys. 27, 1076-85 (2000)

[36]M. J. Rivard, "Monte Carlo radiation dose simulations and dosimetric comparison of the model 6711 and 9011 $^{125}$I brachytherapy sources," Med. Phys. 36, 486-91 (2009)

[37]K. T. Sowards and A. S. Meigooni, "A Monte Carlo evaluation of the dosimetric characteristics of the Best Model 2301 125I brachytherapy source," Applied Radiation and Isotopes 57, 327-33 (2002)

[38]F.-A. Siebert, A. Srivastav, L. Kliemann, H. Fohlin, and G. Kovacs, "Three-dimensional reconstruction of seed implants by randomized rounding and visual evaluation," Med. Phys. 34, 967-75 (2007)

[39]M. Brunet-Benkhoucha, F. Verhaegen, S. Lassalle, D. B. Nadeau, B. Reniers, D. Donath, D. Taussky, and J.-F. Carrier, "Clinical implementation of a digital tomosynthesis-based seed reconstruction algorithm for intraoperative postimplant dose evaluation in low dose rate prostate brachytherapy," Med. Phys. 36, 5235-44 (2009)

[40]H. Afsharpour, M. D'Amours, Benoite Cote, J.-F. Carrier, F. Verhaegen, and L. Beaulieu, "A Monte Carlo study on the effect of seed design on the interseed attenuation in permanent prostate implants," Med. Phys. 35, 3671-81 (2008)

[41]O. Chibani, J. F. Williamson, and D. Todor, "Dosimetric effects of seed anisotropy and interseed attenuation for $^{103}$Pd and $^{125}$I prostate implants," Med. Phys. 32, 2557-66 (2005)

[42]D. J. Moseley, J. H. Siewerdsen, and D. A. Jaffary, "High-contrast object localization and removal in cone-beam CT," Proc. of SPIE Vol. 5745, 40-50 (2005)

[43]J-F Carrier, L. Beaulieu, F. Therriault-Proulx, and R. Roy, "Impact of interseed attenuation and tissue composition for permanent prostate implants," Med. Phys. 33, 595-04 (2006)

[44]G. Leclerc, M.-C. Lavallee, D. Tubic, J. Metivier, E. Vigneault, and L. Beaulieu, "Idealized line source configuration for permanent 125I prostate implants," Radiother. Oncol. 72, 213-20 (2004)

[45]D. Tubic and L. Beaulieu, "Sliding slice: A novel approach for high accuracy and automatic 3D localization of seeds from CT scans," Med. Phys. 32, 163-74 (2006)

**Paper III**

# Localizing intracavitary brachytherapy applicators from cone-beam CT x-ray projections via a novel iterative forward projection matching algorithm

Damodar Pokhrel

Martin J Murphy

Dorin Todor

Elisabeth Weiss

Jeffrey F Williamson

Accepted for publication in Medical Physics, October (2010)

# Localizing intracavitary brachytherapy applicators from cone-beam CT x-ray projections via a novel iterative forward projection matching algorithm

Damodar Pokhrel, Martin J Murphy, Dorin A Todor, Elisabeth Weiss, and Jeffrey F Williamson
Department of Radiation Oncology, School of Medicine, Virginia Commonwealth University, Richmond, Virginia 23298

## Abstract

**Purpose:** To present a novel method for reconstructing the 3D pose (position and orientation) of radio-opaque applicators of known but arbitrary shape from a small set of 2D x-ray projections in support of intra-operative brachytherapy planning.

**Methods and materials:** The generalized iterative forward projection matching (gIFPM) algorithm finds the six degree-of-freedom pose of an arbitrary rigid object by minimizing the sum-of-squared-intensity-differences (SSQD) between the computed and experimentally-acquired auto-segmented projection of the objects. Starting with an initial estimate of the object's pose, gIFPM iteratively refines the pose parameters (3D position and three Euler angles) until the SSQD converges. The object, here specialized to a Fletcher-Weeks intracavitary brachytherapy (ICB) applicator, is represented by a fine mesh of discrete points derived from complex combinatorial geometric models of the actual applicators. Three pairs of computed and measured projection images with known imaging geometry are used. Projection images of an intrauterine tandem and colpostats were acquired from ACUITY cone-beam CT (CBCT) digital-simulator. An image post-processing step was performed to create blurred binary applicators only images. To quantify gIFPM accuracy, the reconstructed 3D pose of the applicator model was forward projected and overlaid with the measured images and empirically calculated the nearest-neighbor applicator difference for each image pair.

**Results:** In the numerical simulations, the tandem and colpostats positions (x, y, z) and orientations ($\alpha$, $\beta$, $\gamma$) were estimated with accuracies of 0.6 mm and $2^{o}$, respectively. For experimentally acquired images of actual applicators, the residual 2D registration error was less than 1.8 mm for each image-pair corresponding to about 1 mm positioning accuracy at isocenter with a total computation time of less than 1.5 min on a 1 GHz processor.

**Conclusion:** This work describes a novel, accurate, fast and completely automatic method to localize radio-opaque applicators of arbitrary shape from measured 2D x-ray projections. Our results demonstrate ~1 mm accuracy while compared against the measured applicator projections. No lateral film is needed. By localizing the applicator internal structure as well as radioactive sources, the effect of intra- and inter-applicator attenuation can be included in the resultant dose calculations. Further validation tests using clinically acquired tandem and colpostats images will be performed for the accurate and robust applicator/sources localization in ICB patients.

Key words: Intracavitary Brachytherapy Applicators, Localization, Generalized Iterative Forward Projection Matching, Cone-beam CT, X-ray projections.

## I. INTRODUCTION

Despite more than a century of routine clinical use, intracavitary brachytherapy (ICB) treatment planning for gynecological malignancies continues to be dominated by the six-decade old practice of using orthogonal 2D radiographs to localize the radioactive sources in the patient.[1] Because this process involves manual drawing of the source positions on films or digital images; it is time consuming and may be error prone. Tandem sources are difficult to visualize in the 30% of cases for larger patient (thickness greater than 38 cm) due to poor lateral radiograph quality while the colpostats edges are almost always obscured in the lateral view because of the pelvic bone and the overlap of the two colpostats.[2] Brachytherapy applicators have complex internal structures[3-6], the pose (position and orientation) of which relative to the patient's anatomy needs to be determined for more accurate dose evaluation via Monte Carlo simulation[5-10] or utilizing Acuros$^{TM}$ (Transpire, Inc., Gig Harbor, WA), a grid-based Boltzmann solver algorithm to account for dose perturbations due to inhomogeneities.

The conventional ICB clinical workflow involves moving and repositioning the patient with applicator insert on the fan beam CT table often inaccurately and then returning the patient to the treatment room. This can result in patient discomfort and large (up to 10.4 mm) uncertainties due to moving the applicators relative to the central pelvic

organs.[11] Also, it does not allow for altering and optimizing the treatment plan intra-operatively. In order to obtain a true intra-operative optimized plan, one must automatically identify the 3D pose of the applicator and source position with respect to the patient 3D anatomy in near real time. Brachytherapy procedure tables equipped with intra-operative 3D cone-beam CT (CBCT) or planar imaging systems have the potential to support more accurate source localization, intra-operative correction of implants, and more accurate post-implant dose evaluation without moving or repositioning the patient. However, the 3D CT method is severely hampered by metal streaking artifacts, time required to manually segment or threshold the applicator surface, and limited spatial resolution due to slice thickness effects. The ACUITY CBCT imaging system in our procedure room requires over two minutes to acquire CBCT images[12] and can not provide useful images with the metal applicators in the field of view.

The problem of localizing applicators is closely related to the problem of metal streaking artifacts. The widely-used shielded vaginal applicators[13-14] are known to cause severe streaking artifacts limiting the value of CT imaging for segmenting critical organs at risk relative to the implanted applicators. Over the past few decades, the problem of metal artifact suppression has been studied extensively by restoring the missing information's in the sinogram region either using interpolation techniques[15-18] or registering a prior metal-free CT images.[19] Another more general approach is to use iterative solutions. The alternating minimization (AM) and other iterative statistical algorithms[20-21] can provide artifact-free CT images of the soft tissues near implanted foreign metal bodies; provided that a priori model of the metal object, including its pose, shape, and attenuation map is essential when using AM image reconstruction to suppress metal streaking artifacts. The iterative forward projection matching (IFPM) approach[22-24] contributes to this solution by using high spatial resolution projections, rather than streak-limited CT images for applicator localization and by making accurate applicator pose estimates available as an input to the iterative reconstruction algorithm.

Because the spatial resolution of the applicators in the 2D image planes is superior to CT, reconstructing applicators from radiographic images can address some of

the problems associated with the post-operative CT as described above. This can be done using the ACUITY imaging system in the brachytherapy treatment room with applicator reconstruction from measured 2D CBCT projections. To accomplish these goals, we have further generalized the IFPM (gIFPM) algorithm[22-24] from five degree-of-freedom needed to reconstruct permanent implant seed centroids and orientations, to the six degree-of-freedom needed to reconstruct the 3D pose of arbitrary-shaped objects from the measured 2D x-ray projections. The applicator model is a fine mesh of discrete points derived from a complex combinatorial geometric (CCG) modeling[5] of the actual applicators. Each applicator model has three translational and three rotational degrees of freedom. The parameterized 3D applicator model was forward projected on the 2D detector planes using CBCT projection geometry and then adjusted iteratively to match with the measured images. In this approach, each applicator model moves independent of the others in the 3D space. The numerical simulation studies with tandem and colpostats were performed to demonstrate the proof of concepts of this method. Also, we used measured images of the actual applicator configurations to experimentally validate the new algorithm in a clinical setting.

## II. MATERIALS AND METHODS

### A. Example shielded applicator system

A low dose-rate (LDR) manual afterloading system using $^{137}$Cs sources loaded into Weeks[4] CT-compatible Fletcher-Suit applicator is used in this study [see Figure 1 (a)]. The applicators consist of thin-walled central tandem and aluminum colpostats. The volume based CCG modeling code[5] was used to obtain the initial estimate of the 3D pose of the applicator models (i.e., mathematical representation of the applicator models including internal structure as well as outer surface). Given a completed geometric model, the code package supports point and segment classification as well as advanced ray tracing through the applicator components. As shown in Figure 1 (b), detailed 2D images of the 3D geometric models of each applicator component were generated by using CBCT projection geometry. It uses set theoretic definitions of region boundary, interior, and exterior, and complex regions as set-theoretic unions, intersections and differences of the complex regions (i.e., mathematically defined geometric objects). Such

complex modeling of the applicator geometry is essential to obtain partial transmission through the applicator components and to obtain accurate Monte Carlo dose distributions.


Fig.1. (a) Close-up photograph of the Fletcher-Weeks CT-compatible after-loadable colpostats and one of the tandems used in this study, (b) computed CBCT projections of the 3D tandem and right colpostat models, where the image background represent uniform elliptical water cylinder. The image intensity values represent an arbitrary integer number assigned to each material in the model.

**B. Generalized IFPM algorithm and initial estimates**

The IFPM algorithm[22-24] was further generalized to accurately localize ICB applicators of known metal body shape, known materials but unknown locations and orientations inside the 3D anatomy using only a few CBCT projection images.

The generalized IFPM algorithm requires six pose parameters to fully describe each of the N applicators $k = 1, \cdots, N$ (typically N = 3 for tandem and colpostats) in the world coordinate system (WCS) which takes as its origin the isocenter of the imaging system and has X, Y, Z directions defined by the x axis is left-right, the y axis is anterior-posterior, and the z axis is superior-inferior direction, for a patient in supine position with feet pointing away from the gantry stand. For the k-*th* applicator, $\left(t_x, t_y, t_z, \alpha, \beta, \gamma\right)_k$ where, $\mathbf{t}_k = \left(t_x, t_y, t_z\right)_k$ denotes the WCS coordinates of origin of the k-*th* applicator's local coordinate system and the three equal-spaced angles $\mathbf{\Theta}_k = \left(\alpha, \beta, \gamma\right)_k$ describe its orientation of this local coordinate system in WCS relative to CBCT isocenter around the x, y, z axes, respectively. Each applicator is described by a fine mesh of $Q_k$ points:

$\{\mathbf{r}\}_k = \{\mathbf{r}_{ik} \mid \mathbf{r}_{ik} \in A_k, i = 1, \cdots, Q_k\}$ derived from the CCG applicator model when $\boldsymbol{\Theta}_k = 0$ and $\mathbf{t}_k = 0$ described in the previous section. Typically, a mesh of 1 × 1 × 1 mm$^3$ is used. A model of the CBCT projection geometry is made and positioned at *M* locations and orientations (gantry angles for ACUITY) specified by translation and rotation matrices for each image viewpoint. In the extrinsic detector model, the orientation of each isocentric projection in the world coordinate frame is defined by the angles $(\varphi, \psi, \eta)$ which describe rotations of the detector image plane around the x, y, z axes, respectively. The detector model is parameterized by describing its magnification, image center, image size and pixel resolution for each image viewpoint. The source to isocenter and isocenter to the detector distances are denoted by the symbols S and D, respectively.

The mesh of discrete points, $\{\mathbf{r}\}_k$ derived from a CCG modeling[5] of the actual applicator, needs to be done only once. For a candidate pose, $(\mathbf{t}_k, \boldsymbol{\Theta}_k)$, we obtain the rotated and translated set of mesh points,

$$\left\{\mathbf{r}' \mid (\mathbf{t}_k, \boldsymbol{\Theta}_k)\right\}_k = \left\{\mathbf{r}'_{ik} \mid \mathbf{r}'_{ik} = \left[\mathbf{R}_{\alpha.\beta.\gamma}(\boldsymbol{\Theta}_k)\right]\mathbf{r}_{ik} + \mathbf{t}_k, \mathbf{r}_{ik} \in A_k, i = 1, \cdots, Q_k\right\} \quad (1)$$

where, the rotation matrix $\left[\mathbf{R}_{\alpha.\beta.\gamma}(\boldsymbol{\Theta}_k)\right]$ is derived in the appendix. Each point in $\mathbf{r}'_{ik} \in \left\{\mathbf{r} \mid (\mathbf{t}_k, \boldsymbol{\Theta}_k)\right\}_k$ is projected onto the detector plane defined by gantry angle $\eta$, giving rise to a 2D coordinate position $P_\eta(\mathbf{r}'_{ik}) = (u'_{ik}, v'_{ik})_\eta$ where $P_\eta(\mathbf{r})$ denotes the continuous coordinates of the point $\mathbf{r}$ in 3D space projected into the detector plane for a gantry angle of $\eta$. Then, we obtain the computed binary image of the *N* applicators, $I_0\left(u, v \mid \{\mathbf{r}(\mathbf{t}_k, \boldsymbol{\Theta}_k)\}_k, \eta\right)$, corresponding to the initial set of pose estimates, $\{\mathbf{r}(\mathbf{t}_k, \boldsymbol{\Theta}_k)\}_k$, by setting to unity all those detector pixels $(u, v)$ that contain one or more projected points $(u'_{ik}, v'_{ik})_\eta$ from one of the applicator mesh projections and zero elsewhere. More explicitly, the discretized applicator image pixels intensity is given by,

$$I_0\left(u, v \mid \{\mathbf{r}_k, \boldsymbol{\Theta}_k\}, \eta\right) = \begin{cases} 1 & \text{if } \exists\, i,k \text{ such that for } \mathbf{r}_{ik} \in \left\{\mathbf{r} \mid (\mathbf{t}_k, \boldsymbol{\Theta}_k)\right\}_k, P_\eta(\mathbf{r}_{i,k}) \in \{u, v\} \\ 0 & \text{if not.} \end{cases} \quad (2)$$

where $\{u,v\}$ denotes the set of 2D coordinates contained with the detector pixel indexed by $u$ and $v$. The binary mask representation of the projected applicator is then blurred by convolving it with 2D Gaussian blurring function with a standard deviation, σ. For a set of N applicators projected from the world frame then the total computed image is,

$$I_c\left(u,v\,|\,\{\mathbf{r}_k,\boldsymbol{\Theta}_k\},\sigma,\eta\right)=\sum_{u_{ik}^{'},v_{ik}^{'}} I_0\left(u_{ik}^{'},v_{ik}^{'}\,|\,\mathbf{r}_k,\boldsymbol{\Theta}_k,\eta\right)\exp\left[-\left(u-u_{ik}^{'}\right)^2\Big/2\sigma^2-\left(v-v_{ik}^{'}\right)^2\Big/2\sigma^2\right] \qquad (3)$$

where $\left(u_{ik}^{'},v_{ik}^{'}\right)$ denote the center spatial coordinates of the image plane pixel indexed by $u$ and $v$. The main purpose of the Gaussian blurring is to create a continuous-value grayscale image to which a gradient-driven iterative search process can be applied. In the absence of any blurring on the images, large areas of the intensity map would have zero intensity, providing no gradient to guide the similarity minimization search. The blurring creates "source attractive" potential well around each applicator with tails extending beyond the applicator footprint, causing computed applicator images to be pulled towards measured applicator images, and accelerating the convergence of the iterative minimization search.

The overall similarity metric, SSQD is the total of the pixel-by-pixel sum of the squared intensity differences for all $M$ computed, $I_c\left(u,v\,|\,\{\mathbf{r}_k,\boldsymbol{\Theta}_k\},\sigma,\eta\right)$ and the experimentally acquired (measured) blurred $I_m\left(u,v\,|\,\sigma,\eta\right)$ applicator image pairs,

$$SSQD\left(\{\mathbf{r}_k,\boldsymbol{\Theta}_k\}\,|\,\sigma,\eta\right)=\sum_{\eta}\sum_{u,v}\left[I_c\left(u,v\,|\,\{\mathbf{r}_k,\boldsymbol{\Theta}_k\},\sigma,\eta\right)-I_m\left(u,v\,|\,\sigma,\eta\right)\right]^2 \qquad (4)$$

The applicator poses parameters, $\{\mathbf{r}_k,\boldsymbol{\Theta}_k\}$, are iteratively updated by simultaneously adjusting poses of all applicators, computing updated images $I_c\left(u,v\,|\,\{\mathbf{r}_k,\boldsymbol{\Theta}_k\},\sigma,\eta\right)$, and re-evaluating the objective function, Equation (4). The pose updates are calculated from the first derivatives of SSQD with respect to each degree of freedom. For example, the derivative with respect to the x-coordinate of the k-*th* applicator was computed as follows;

$$\partial(SSQD)\big/\partial x_k=2\sum_{\eta}\left(\sum_{u,v}\left[I_c\left(u,v\,|\,\{\mathbf{r}_k,\boldsymbol{\Theta}_k\},\sigma,\eta\right)-I_m\left(u,v\,|\,\sigma,\eta\right)\right]\partial I_c\left(u,v\,|\,\{\mathbf{r}_k,\boldsymbol{\Theta}_k\},\sigma,\eta\right)\big/\partial x_k\right) \qquad (5)$$

Because the image grayscale intensities are represented entirely by the Gaussian blurring function, each grayscale partial derivative, such as $\partial I_c\left(u,v\,|\,\{\mathbf{r}_k,\boldsymbol{\Theta}_k\},\sigma,\eta\right)\big/\partial x_k$ , was calculated analytically for each applicator pixel (u,v) and found the best gradients. That is, to provide a single derivative with respect to each degree of freedom for updating $\{\mathbf{r}_k,\boldsymbol{\Theta}_k\}$, $\partial I_c\left(u,v\right)\big/\partial x_k$ was averaged over all pixels $\left(\mathrm{u},\mathrm{v}\right)$ contained within the shadow of the k-*th* arbitrary-shape applicator model (i.e., $\overline{\partial I_c\left(u,v\right)\big/\partial x_k}$ and so on). Similarly, we computed the first derivatives of SSQD with respect to all other spatial and angular coordinates. Detailed derivations of the gradient calculation can be found in appendix.

After computing the gradients, the free parameters were updated using a nonlinear gradient search method[22] that combines steepest descent gradient search with a parabolic approximation of the SSQD surface around the global minimum. The process iteratively refines the 3D applicator pose parameters until the closet match between computed and measured projections is achieved. The computed and measured images should have the same imaging geometry, image size and pixel resolution. Each three pairs of computed and measured images datasets with corresponding imaging parameters are required for one reconstruction process. In this way, the voxelized 3D geometric model of arbitrary shape was integrated into the forward projection matching method for computing the 2D projection images of the 3D ICB applicators, iteratively.

**C. Validation via simulated applicator models**

Numerical simulation studies were performed to demonstrate the feasibility of our approach. The 3D geometry of the Fletcher-Weeks tandem and colpostats was modeled as described in §II.A, producing a fine mesh of points to represent the applicator. Two different types of experiments were performed: (a) applicator reconstruction using intrauterine tandem only; (b) applicator components reconstruction using the entire applicator system consisting of bilateral colpostats plus tandem. In these simulation studies, the true applicator system pose consisted of tandem was placed in the middle of the field of view; bilateral colpostats were placed on either side of the tandem, had

equivalent transaxial bisecting planes, and centers 25 mm, 35 mm, and 45 mm apart. This is the true pose of the applicators configuration which we wished to determine. Using these applicator configurations, synthetic measured projection images were computed using the CBCT projection geometry at different gantry angles within ±30$^{o}$. The projected applicators on the imaging plane were masked to create the binary bitmap images. In 3D space, each applicator component was shifted by a displacement ±2.5 mm in each coordinate axis and rotated ±8$^{o}$ around each rotation axis. This was our initial estimate. Both the true/synthetic measured and computed images were blurred using 2D Gaussian blurring function ($\sigma$ = 3.0 mm to 4.0 mm) with a known intensity distribution. The source to detector distance was 150 cm and source to object distance was 100 cm. The images were 288 × 288 pixels square and had a pixel resolution of 0.388 mm/pixel. Several trials were performed by varying colpostat separation distance from 25 mm to 45 mm.

**D. Validation via physical (actual) applicators**

To experimentally validate this algorithm, the applicators (tandem and colpostats) were imaged on a Varian Acuity imaging system (Varian Inc., Palo Alto, CA) which is used for performing image-guided brachytherapy insertions in our dedicated brachytherapy suite. Projection images of the actual applicators were acquired in different gantry angle positions within ±30$^{o}$ using the Varian 4030CB imager. The detector is 40 cm × 30 cm with a 1024 × 768 image size and pixel resolution of 0.388 mm/pixel. The image post-processing involved a) cropping the images to 576 × 576 pixels square; b) normalizing the image intensity by finding its maximum and minimum values in the image; c) morphological top-hat-filtering to suppress the background; and d) automatic thresholding using the 3-standard deviation value of the pixel intensity histogram to create binary applicator images in each projection in order to separate the applicators from the background. This process resulted in binary bitmap images with zero intensity in the background and intensity one over the area of each projected applicator model. The binary images were then convolved with a 2D Gaussian blurring function chosen from $\sigma$ = 3.0 mm to 4.0 mm. An example case of image post-processing is shown in Figure 2.

Three different experiments were performed by keeping the colpostat separation at 30 mm, 40 mm, and 50 mm, respectively.

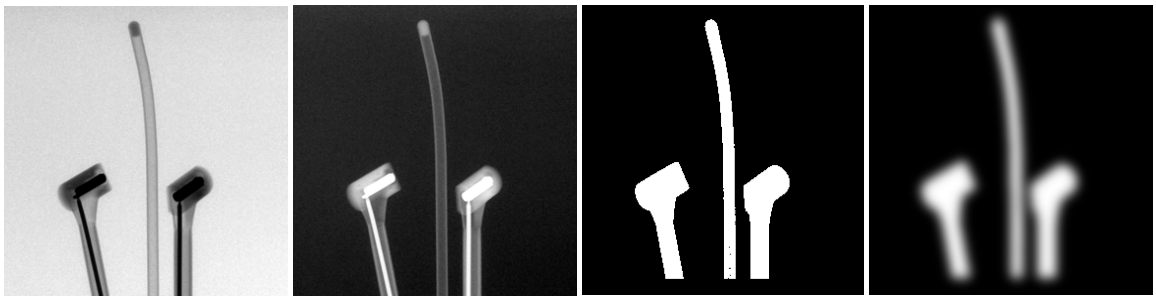


Fig.2. An example illustrating post-processing of experimentally acquired ACUITY projection images, (a) raw projection image, (b) top-hat filtered image, (c) binary image, and (d) blurred grayscale image used as an input to the generalized IFPM algorithm.

Initial estimates of the applicator model were obtained by perturbing the known 3D applicator components, as described earlier. To make the computed projection images, the perturbed applicators configuration was rotated and translated to each imaging viewpoint and then projected on the $(u, v)$ detector planes. For each candidate set of poses, $\{\mathbf{r}_k, \boldsymbol{\Theta}_k\}$, computed applicator images were evaluated as described in §II.B using the same CCG geometric model.

**E. Assessment of the applicator reconstruction/registration error**

For the simulation study, the actual known pose of the applicators was used to benchmark gIFPM. First, the accuracy of each trial was quantified by calculating the difference between all estimated and the true 3D pose parameters of the each applicator component. In addition, agreement was qualitatively assessed by calculating the difference between the measured and final computed images for each gantry angle. In the second approach, the residual 2D registration error was computed by re-projecting the applicator pose at convergence onto the 2D image planes, overlaying the computed and measured applicator projections, and calculating the nearest-neighbor positional difference between the measured and computed applicator positions in each image plane. In this approach, for all computed applicator components, we empirically calculated the applicator center location in each 2D image plane and compared with those obtained

from the measured applicator components images at convergence. The center of mass position of the entire tandem was used. For the bilateral colpostats we empirically calculated the center of mass of the each source position.

For the physical applicator study, there were no ground truth coordinates. The applicator registration error was computed in terms of residual 2D radial difference between computed and measured applicator images at convergence in each image plane as described above.

## III. RESULTS

### 1. Simulated applicator models

Several experiments were performed to test the accuracy and robustness of this algorithm, including different initial estimates of the digital tandem. Figure 3 (a) shows one of the convergence rate graphs of the gIFPM for a digital tandem, and (b) shows reconstructed 3D view overlaid with the true/measured tandem. This case required 9 iterations (Gaussian width, $\sigma$ = 3.6 mm) with a total computation time of less than 40 second on a 1 GHz processor. The error in positional and angular pose components was found to be (0.32, 0.46, -0.37) mm and (1.03, 0.87, 1.16) $^{o}$, respectively.

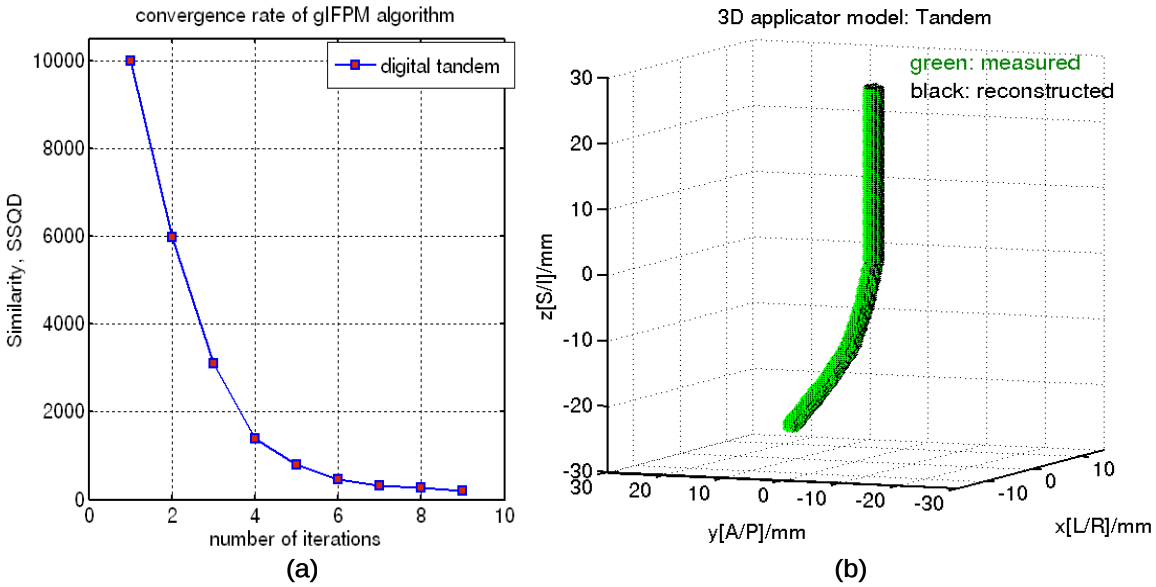


Fig.3. Results of a simulation of tandem localization by gIFPM. (a) The similarity metric score vs. iteration number and (b) point-by-point overlay of the reconstructed tandem (black) with the true/ synthetic

measured tandem (green), demonstrating near coincidence achieved by the 3D/2D gIFPM registration process.

Figure 4 shows an example of the iterative matching process for simulated full ICB applicator system, i.e., intrauterine tandem and bilateral colpostats. The three projections have gantry angles of 0°, ±30°. The small difference in Figure 4 (d) shows very good agreement between the measured and computed binary images at convergence, including reproducing overlapping applicator components.

**Table I.** Accuracy of gIFPM reconstructed poses for 3 simulated full applicator system configurations. The difference for the each applicator component position and orientation coordinates is reported.

| Separation between the colpostats (mm) | Image viewpoint used ($^o$) | Applicator components | gIFPM vs. true applicator pose | | | | | |
|---|---|---|---|---|---|---|---|---|
| | | | Difference in applicator position (mm) | | | Difference in applicator orientation ($^o$) | | |
| | | | $\Delta x$ | $\Delta y$ | $\Delta z$ | $\Delta\alpha$ | $\Delta\beta$ | $\Delta\gamma$ |
| 25 | 0, -30, +30 | Tandem | 0.41 | 0.59 | -0.38 | -0.98 | 0.78 | 1.86 |
| | | R. colpostats | 0.18 | -0.56 | 0.48 | 2.03 | 1.71 | -0.89 |
| | | L. colpostats | -0.38 | -0.48 | 0.61 | -0.85 | 2.04 | 1.95 |
| 35 | 0, +20, -20 | Tandem | 0.15 | -0.37 | 0.46 | 0.89 | 0.95 | -0.86 |
| | | R. colpostats | -0.32 | -0.15 | 0.36 | 1.56 | -0.74 | 1.62 |
| | | L. colpostats | -0.28 | 0.54 | -0.51 | -0.87 | 1.42 | 0.73 |
| 45 | 0, -30, +30 | Tandem | -0.18 | 0.27 | 0.34 | -0.86 | -0.64 | -0.72 |
| | | R. colpostats | 0.14 | 0.18 | -0.35 | 0.46 | 0.58 | 0.65 |
| | | L. colpostats | -0.20 | 0.34 | 0.52 | 0.87 | 1.06 | -0.56 |

In Figure 5 we show the cost function convergence as a function of iteration number for all three simulated example cases. All test trials converged in 10 to 12 iterations (Gaussian width, $\sigma$ = 3.8 mm) with a total computation time of about 1.5 min on a 1 GHz processor. The comparison is summarized for all three cases in Table I. In all trials the difference errors were less than 1 mm and 2$^o$ for each of the positional and angular coordinates, respectively.

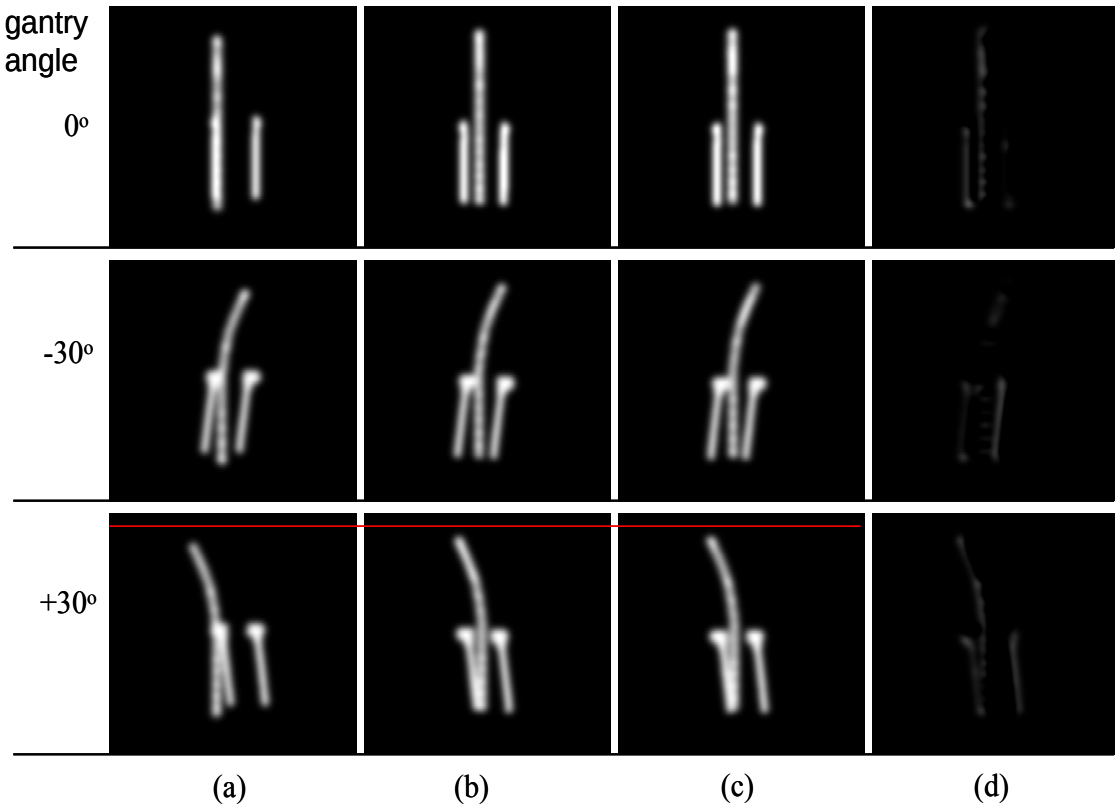


Fig.4. An illustration of the iterative convergence process for a simulated implant consisting of tandem and bilateral colpostats for a 25 mm colpostat separation; Column (a) initial estimate of the applicator configuration, (b) computed images at convergence, (c) the true/synthetic measured images, and (d) difference between (b) and (c), where the rows represents different gantry angles. The red line in the 3rd row indicates that the reference of the initial estimate with respect to the measured images in (c). The generalized IFPM algorithm was able to reproduce each applicator pose, as well as overlapping components.

Large numbers of experiments were performed using different gantry angle combinations as well as different initial starting configurations of the applicator models in the course of this study. Theoretically, one should expect SSQD = 0 at the convergence, i.e., all computed applicators images exactly match with those measured. However, from Figure 5, for the combined-applicators geometries, it is evident that the SSQD does not exactly converge to zero (i.e. less than 3% difference between measured and computed applicators images), showing less than optimal convergence (i.e., trapping in local minima). That means if the initial estimate of the applicators configuration is far apart from the measured configuration there is a chance of less than optimal matching.

Finite width of the detector pixel size may also affect the convergence rate of gIFPM algorithm (i.e., larger the pixel size less than optimal the convergence).

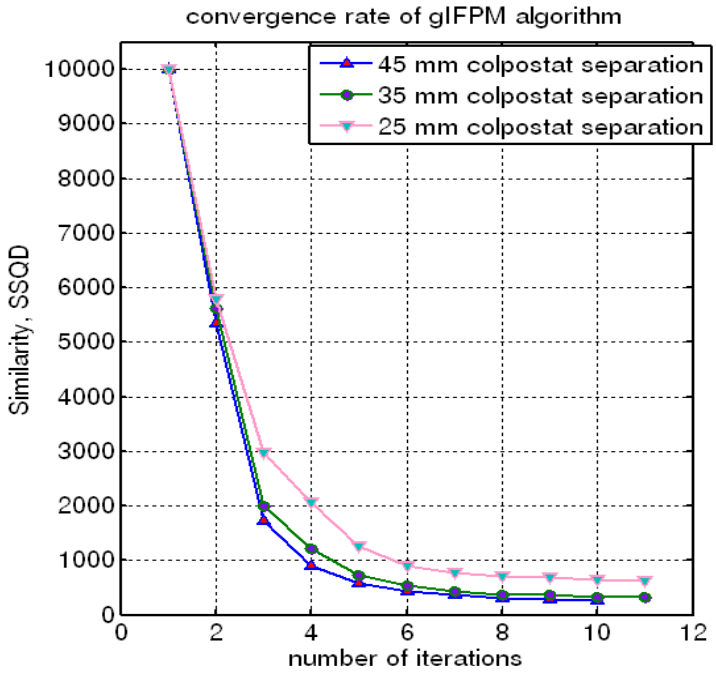


Fig.5. The similarity metric score vs. iteration number for the generalized IFPM algorithm for the three simulated full ICB applicator configurations.

**2. Validation test with measured images**

Several experiments were performed using projection images of the actual intrauterine tandem and bilateral colpostats acquired from the ACUITY digital simulator to validate this algorithm. An example of the reconstructed applicators projected onto the imaging planes is presented in Figure 6 when using colpostat separation of 40 mm. In this case, the residual 2D registration error in computed vs. measured applicators image at each gantry angle were less than 1 mm for the intrauterine tandem and about 1.5 mm for the bilateral colpostats.

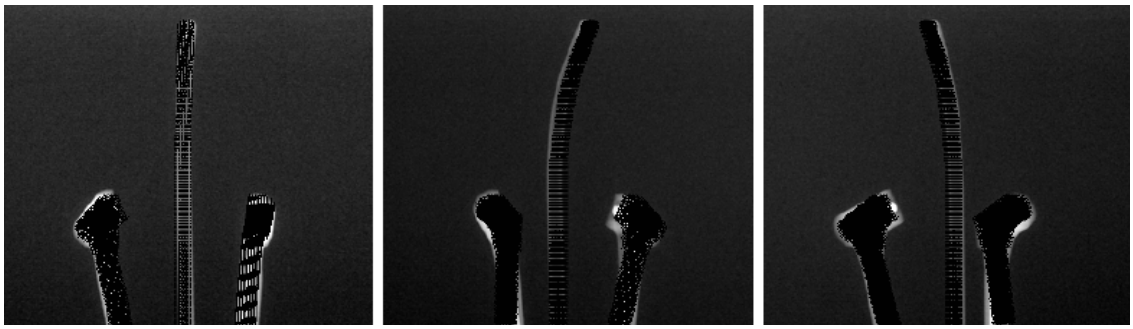


Fig.6. Superposition of experimentally acquired binary images (white) with automatically reconstructed applicators positions (black) projected onto the detector planes, (a) $0^o$ gantry angle, (b) $-30^o$ gantry angle, and (c) $+30^o$ gantry angle, respectively when using 40 mm colpostat separation. The applicator registration error was less than 1 mm for the intrauterine tandem and about 1.5 mm for the bilateral colpostats on each image plane.

**Table II.** The residual 2D registration error between computed and measured applicator projection in terms of 2D radial difference in each image plane. The center of mass position of the entire tandem is reported, whereas center of mass of the source position is empirically calculated for the right- and left colpostats.

| Separation between the measured colpostats (mm) | Applicator components | gIFPM vs. measured applicator position: 2D residual error (mm) | | |
|---|---|---|---|---|
| | | gantry = $0^o$ | gantry = $-30^o$ | gantry = $+30^o$ |
| 30 | Tandem | 0.88 | 1.12 | 1.16 |
| | R. colpostats | 0.93 | 1.88 | 1.57 |
| | L. colpostats | 1.25 | 1.75 | 1.93 |
| 40 | Tandem | 0.67 | 0.89 | 0.78 |
| | R. colpostats | 1.14 | 1.46 | 1.81 |
| | L. colpostats | 0.96 | 1.67 | 1.66 |
| 50 | Tandem | 0.58 | 0.91 | 0.75 |
| | R. colpostats | 0.87 | 1.46 | 1.42 |
| | L. colpostats | 0.72 | 1.58 | 1.54 |

Table II shows the residual 2D registration error between the measured and computed applicator components in each image plane. In all cases, the majority of the 2D radial difference of the applicator registration error was about 1.5 mm or less and no error exceeded 2.0 mm in the detector plane. These preliminary results indicated that good agreement between measured and computed applicators images.

## IV. DISCUSSION

A novel IFPM algorithm has been successfully extended to more complex six degree-of-freedom problem of automatically reconstructing the 3D pose of radio-opaque non-symmetric objects (e.g., ICB applicators) from measured 2D projections. No lateral film is required. With further testing and integration into the clinical workflow, our gIFPM has the potential to support real-time, robust, and unsupervised reconstruction of implanted object pose for the purpose of supporting intra-operative ICB planning, dose evaluation, or plan adaptation.

Several methods are available for automatically localizing ICB sources and applicators from 3D CT studies[4, 7, 25] including brachytherapy catheters reconstruction.[26] The plastic applicators developed by Schoeppel et al.[25], does not produce streaking artifacts in the CT images and has the ability to shield portions of the bladder and rectum by retaining through the use of tungsten alloy shields which are after-loadable with the radioactive sources. However, the physical size of the applicators geometry was too large. An approach developed by Lerma and Williamson[7] in which a 3D rigid model of the external applicator shape is rigidly registered to the corresponding surface manually contoured in the reconstructed CT images. For typical ICB applicator orientations, they demonstrated that the localization accuracy was about 1/3 the slice thickness. Because 2D projection image resolution is superior to that of 3D CBCT, gIFPM has the potential to reconstruct 3D applicator poses more accurately than the 3D CT method. Another advantage of gIFPM over the 3D CBCT method is that the latter requires acquisition and reconstruction of entire 3D image, which currently requires 2 to 4 minutes for the Varian ACUITY system plus repositioning of the patient to enable a $180^{o}$ sinogram acquisition orbit, compared few seconds for acquiring 3 projections within 30 degrees of an en face anterior view.

Another 2D radiographic approach developed by Li *et al.*[27], is based on identifying several corresponding landmark points on the 2D projections, which allows the pose of the object to be reconstructed. gIFPM can be viewed as a generalization of this process which does not require manual identification of landmark points and uses all information available in the applicator footprint. Because of the excellent soft-tissue

contrast, MRI-based applicator reconstruction[28-30] could be the future trend. However, as it is now, the cost associated with intra-operative MRI in brachytherapy suite causes their installation to be uncommon and MR-compatible applicators are expensive themselves.

For ICB applicators containing high-atomic number structural (steel, brass) or shielding materials (tungsten alloys), the often cause severe metal streaking artifacts[13-14] further challenge the 3D CT method. Such artifacts reduce the accuracy of applicator body delineation as well as difficult in visualization of the soft tissue organ boundaries and introduce large error in the dose calculations, clearly hindering integration of CT into the planning process. The streaking artifacts are sufficient to defeat deformable image registration, commonly use for image-guided procedures. Our six parameter model exploits 3D pose of the each applicator component using few CBCT projections sinogram. In the future, we therefore plan to use the accurate 3D pose of each applicator component into the CT images reconstruction process. That is after extracting the actual metal object boundaries from the sinogram region, we can recover the missing soft-tissues information's obscured by the ICB applicators either from pre-operative metal-free projections[19] or using AM reconstruction algorithm[20-21] to suppress the metal streaking artifacts.

To improve the accuracy of the applicator localization validation study, we plan to design a precision-machined pelvic phantom that house ICB applicators and test the gIFPM performance against a more realistic ground truth. Also, the dependence of convergence rate and accuracy on the initial estimate needs more extensive investigation. Our current IFPM implementation is limited to estimating the 3D applicator pose. Incorporating geometric uncertainties such as gantry angle inaccuracy and detector displacement and orientation into the estimation model is an area of future development. The algorithm could also be extended to other types of objects, e.g., stirrups, retractors, and table supports, including parameters to describe flex or internal motion within the applicators, partial transmission objects, and matching of un-segmented grayscale images are fruitful avenues for future development.

## V. CONCLUSION

We have presented a new approach to brachytherapy applicator localization, gIFPM that we believe to be the first fully automatic approach described in the literature able to accurately recover the orientation as well as location of individual applicator components using few 2D x-ray projections. By localizing the applicator internal structure and the sources, the effect of intra- and inter-applicator attenuation can be included in the resultant Monte Carlo or other dose calculations. Based on both simulated and actual applicator models, the localization errors were less than 1.5 mm and 2° for orientation angles. By incorporating six degrees of freedom search capability, the IFPM approach, can be extended to pose estimation of any shape radio-opaque object that can be geometrically modeled. The gIFPM algorithm is fast and has the potential to support intra-operative dose reconstruction and adaptive replanning. In combination with advanced image-reconstruction algorithms, accurate 3D localization of metal attenuation maps in the patient could contribute to mitigation of metal artifact streaking artifacts.

## ACKNOWLEDGMENTS

This work was supported in part by grants from Varian Medical System and the National Institutes of Health (P01 CA 116602). The authors would like to thank Virginia Gilbert of Virginia Commonwealth University (VCU) for her continuous support of collecting data. The authors are grateful to Dr. Dimitrios Lazos (Beth Israel Medical Center, NY) and Andrew Sampson (VCU) for their help with combinatorial geometric modeling we described.

## APPENDIX: ANALYTIC GRADIENT OF THE SIMILARITY, SSQD WITH RESPECT TO SIX DEGREES OF FREEDOM OF THE APPLICATOR MODEL

For each of the *i-th* coordinates of the *k-th* applicator model in the rotated and translated CT frame,

$$\left\{\mathbf{r}' \mid (\mathbf{t}_k, \boldsymbol{\Theta}_k)\right\}_k = \left\{\mathbf{r}'_{ik} \mid \mathbf{r}'_{ik} = \left[\mathbf{R}_{\alpha.\beta.\gamma}(\boldsymbol{\Theta}_k)\right]\mathbf{r}_{ik} + \mathbf{t}_k, \mathbf{r}_{ik} \in A_k, i = 1, \cdots, Q_k\right\} \quad \text{(A1)}$$

Rewriting equation (A1) more explicitly,

$$\begin{Bmatrix} x' \\ y' \\ z' \end{Bmatrix}_k = \left[\mathbf{R}_{\alpha.\beta.\gamma}\right]_k \begin{Bmatrix} x \\ y \\ z \end{Bmatrix}_{ik} + \mathbf{t}_k \tag{A2}$$

where,

$$\left[\mathbf{R}_{\alpha.\beta.\gamma}\right]_k = \begin{bmatrix} R11 & R12 & R13 \\ R21 & R22 & R23 \\ R31 & R32 & R33 \end{bmatrix}_k = \begin{bmatrix} \cos\gamma\cos\beta & \cos\gamma\sin\beta\sin\alpha - \sin\gamma\cos\alpha & \cos\gamma\sin\beta\cos\alpha + \sin\gamma\sin\alpha \\ \sin\gamma\cos\beta & \sin\gamma\sin\beta\sin\alpha + \cos\gamma\cos\alpha & \sin\gamma\sin\beta\cos\alpha - \cos\gamma\sin\alpha \\ -\sin\beta & \cos\beta\sin\alpha & \cos\beta\cos\alpha \end{bmatrix}_k$$

is the complete rotation matrix. The complete rotation matrix was obtained by taking the product of the three rotation matrices defined in the world coordinate system, for each image viewpoint. No translation is applied (i.e., $\mathbf{t}_k = 0$). The equation (A2) can be written as,

$$\left.\begin{aligned} x'_k &= \left(R11.x_i\right)_k + \left(R12.y_i\right)_k + \left(R13.z_i\right)_k \\ y'_k &= \left(R21.x_i\right)_k + \left(R22.y_i\right)_k + \left(R23.z_i\right)_k \\ z'_k &= \left(R31.x_i\right)_k + \left(R32.y_i\right)_k + \left(R33.z_i\right)_k \end{aligned}\right\} \tag{A3}$$

Rewriting equation (A2) more explicitly,

$$\left.\begin{aligned} x'_k &= \left(\cos\gamma.\cos\beta.x_i\right)_k + \left(\cos\gamma.\sin\beta.\sin\alpha.y_i - \sin\gamma.\cos\alpha.y_i\right)_k + \left(\cos\gamma.\sin\beta.\cos\alpha.z_i + \sin\gamma.\sin\alpha.z_i\right)_k \\ y'_k &= \left(\sin\gamma.\cos\beta.x_i\right)_k + \left(\sin\gamma.\sin\beta.\sin\alpha.y_i + \cos\gamma.\cos\alpha.y_i\right)_k + \left(\sin\gamma.\sin\beta.\cos\alpha.z_i - \cos\gamma.\sin\alpha.z_i\right)_k \\ z'_k &= \left(-\sin\beta.x_i\right)_k + \left(\cos\beta.\sin\alpha.y_i\right)_k + \left(\cos\beta.\cos\alpha.z_i\right)_k \end{aligned}\right\} \tag{A4}$$

The applicator models in the rotated CT frame project to the detector plane $(\mathrm{u}, \mathrm{v})$ are given by,

$$\left(u'_{ik}, v'_{ik}\right) = M\left(z'_k\right)\left(x'_k, y'_k\right) \tag{A5}$$

where, $M_k = \left(S + D/S + z'_k\right)$ is the magnification factor, which is different for each point mesh; S and D are the source-to-isocenter and isocenter-to-detector distances, respectively. Since, the brachytherapy applicator has non-rotational symmetry (i.e., arbitrary shape) around the axis of rotation; we computed one derivative per point per applicator per degree of freedom and found the best derivative for that degree of freedom. From equation (3), the image grayscale gradient for x-degree of freedom was calculated as follows,

$$\partial I_c\left(u,v\,|\,\{\mathbf{r}_k,\boldsymbol{\Theta}_k\}\,|\,\sigma,\eta\right)/\partial x_k = \sum_{u_{ik}^{'},v_{ik}^{'}}\left(I_0\left(u_{ik}^{'},v_{ik}^{'}\,|\,\mathbf{r}_k,\boldsymbol{\Theta}_k\right)/\sigma^2\right)\left[\left(u-u_{ik}^{'}\right)\partial u_{ik}^{'}/\partial x_{ik} + \left(v-v_{ik}^{'}\right)\partial v_{ik}^{'}/\partial x_{ik}\right].g\left(u-u_{ik}^{'},v-v_{ik}^{'}\,|\,\sigma\right) \tag{A6}$$

where, $g\left(u-u_{ik}^{'},v-v_{ik}^{'}\,|\,\sigma\right)=\exp\left[-\left(u-u_{ik}^{'}\right)^2/2\sigma^2-\left(v-v_{ik}^{'}\right)^2/2\sigma^2\right]$, $\eta$ is the gantry angle and $\boldsymbol{\Theta}_k$ related to the original pose variables $\left(\boldsymbol{\alpha},\boldsymbol{\beta},\boldsymbol{\gamma}\right)_k$ in the 3D space.

Finally, from equations (A3) and (A5), using chain rule, we get,

$$\left.\begin{aligned}\partial u_{ik}^{'}/\partial x_{ik} &= M_k\left[R11-\left(R31\right)x_k^{'}/\left(S+z_k^{'}\right)\right]\\ \partial v_{ik}^{'}/\partial x_{ik} &= M_k\left[R21-\left(R31\right)y_k^{'}/\left(S+z_k^{'}\right)\right]\end{aligned}\right\} \tag{A7}$$

and similarly for the y and z coordinates of each applicator model. The analytical gradient of the similarity, SSQD with respect to α-angle coordinate for each applicator model was calculated from equation (4) as follows,

$$\partial\left(SSQD\right)/\partial\alpha_k = 2\sum_{\eta}\left(\sum_{u,v}\left[I_c\left(u,v\,|\,\{\mathbf{r}_k,\boldsymbol{\Theta}_k\},\sigma,\eta\right)-I_m\left(u,v\,|\,\sigma,\eta\right)\right]\partial I_c\left(u,v\,|\,\{\mathbf{r}_k,\boldsymbol{\Theta}_k\},\sigma,\eta\right)/\partial\alpha_k\right) \tag{A8}$$

Again, from equation (3) we have computed the image grayscale gradient with respect to α-degree of freedom,

$$\partial I_c\left(u,v\,|\,\{\mathbf{r}_k,\boldsymbol{\Theta}_k\},\sigma,\eta\right)/\partial\alpha_k = \sum_{u_{ik}^{'},v_{ik}^{'}}\left(I_0\left(u_{ik}^{'},v_{ik}^{'}\,|\,\mathbf{r}_k,\boldsymbol{\Theta}_k\right)/\sigma^2\right)\left[\left(u-u_{ik}^{'}\right)\partial u_{ik}^{'}/\partial\alpha_k + \left(v-v_{ik}^{'}\right)\partial v_{ik}^{'}/\partial\alpha_k\right].g\left(u-u_{ik}^{'},v-v_{ik}^{'}\,|\,\sigma\right) \tag{A9}$$

Finally, from equations (A4) and (A5), using chain rule, we get,

$$\left.\begin{aligned}\partial u_{ik}^{'}/\partial\alpha_k &= M_k\left\{\left[\cos\gamma\sin\beta\cos\alpha+\sin\gamma\sin\alpha\right]y_{i,k}-\left[\cos\gamma\sin\beta\sin\alpha-\sin\gamma\cos\alpha\right]z_{i,k}\right.\\ &\qquad\left.-\frac{x_k^{'}}{\left(S+z_k^{'}\right)}\left\{\left[\cos\beta\cos\alpha\right]y_{i,k}-\left[\cos\beta\sin\alpha\right]z_{i,k}\right\}\right\}\\ \partial v_{ik}^{'}/\partial\alpha_k &= M_k\left\{\left[\sin\gamma\sin\beta\cos\alpha-\sin\alpha\cos\gamma\right]y_{i,k}-\left[\sin\gamma\sin\beta\sin\alpha+\cos\gamma\cos\alpha\right]z_{i,k}\right.\\ &\qquad\left.-\frac{y_k^{'}}{\left(S+z_k^{'}\right)}\left\{\left[\cos\beta\cos\alpha\right]y_{i,k}-\left[\cos\beta\sin\alpha\right]z_{i,k}\right\}\right\}\end{aligned}\right\} \tag{A10}$$

Similarly, we have computed analytical gradient of SSQD with respect to β and γ-angle coordinates of each applicator model and obtained the best derivatives (i.e., $\overline{\partial u_{ik}^{'}/\partial \alpha_k}$ , $\overline{\partial v_{ik}^{'}/\partial \alpha_k}$ and so on).

**References**


[1]International Commission on Radiation Units and measurement, report No. 38 Dose and volume specifications for reporting intracavitary therapy in gynecology, (1985)

[2]C. A. Pelizzari and G. T. Y. Chen, "A new method for localization of sources in Fletcher-Suit tandems," Int. J. Radiat. Oncol. Biol., Phys.15 (1988)

[3]W. L. Saylor and M. Dillard, "Dosimetry of 137Cs sources with the Fletcher-Suit gynecological applicator," Med. Phys. 3, 117-19 (1976)

[4]K. J. Weeks and G. S. Montana, "Three-dimensional applicator system for carcinoma of the uterine cervix," Int. J. Radiat. Oncol. Biol., Phys.37, 455-63 (1988)

[5]Z. Li and J. F. Williamson, "Volume-based geometric modeling for radiation transport calculations," Med. Phys. 19, 667-77 (1992)

[6]M. J. Price, K. A. Gifford, J. l. Horton et al., "Monte Carlo model for a prototype CT-compatible, anatomically adaptive, shielded intracavitary brachytherapy applicator for the treatment of cervical cancer," Med. Phys. 36, 4147-55 (2009)

[7]J. Markman, J. F. Williamson, J. F. Dempsey and D. A. Low, "On the validity of the superposition principle in dose calculations for intracavitary implants with shielded vaginal colpostats," Med. Phys. 28, 147-55 (2001)

[8]F. A. Lerma and J. F. Williamson, "Accurate localization of intracavitary brachytherapy applicators from 3D CT imaging studies," Med. Phys. 29, 325-33 (2002)

[9]K. J. Weeks, "Monte Carlo dose calculations for a new ovoid shield system for carcinoma of the uterine cervix," Med. Phys. 25, 2288-92 (1998)

[10]K. A. Gifford, F. Mourtada, S. H. Cho et al., "Monte Carlo calculations of the dose distribution around a commercial gynecologic tandem applicator," Radiother. Oncol. 77, 210-15 (2005)

[11]N. R. Datta, R. Basu, K. J. Das, et al., "Problems and uncertainties with multiple point A's during multiple high-dose-rate intracavitary brachytherapy in carcinoma of the cervix," Clini. Oncol., 16, 129-37 (2004)

[12]L. A. Feldkamp, L. C. Davis and J. W. Kress, "Practical cone-beam algorithm," Journal of the Optical Society of America A," Optics, Image Science, and Vision 16, 612-19 (1984)

[13]K. A. Gifford, J. L. Horton, Jr., C. E. Pelloski, et al., "A three-dimensional computed tomography-assisted Monte Carlo evaluation of ovoid shielding on the dose to the bladder and rectum in intracavitary radiotherapy for cervical cancer," Int. J. Radiat. Oncol. Biol., Phys. 63, 615-21 (2005)

[14]C. C. Ling, M. C. Schell, K. R. Working et al., "CT assisted assessment of bladder and rectum dose in gynecological implants," Int. J. Radiat. Oncol. Biol., Phys. 13, 1577-82 (1987)

[15]G. H. Golver and N. J. Pelc, "An algorithm for the reduction of metal clip artifacts in CT reconstruction," Med. Phys. 8, 799-807 (1981)

[16]W. A. Kalender, R. Hebel and J. Ebersberger, "Reduction of CT Artifacts Caused by Metallic Implants," Radiology, 164, 576-77 (1987)

[17]J. Hsieh, "Adaptive streak artifacts reduction in computed tomography resulting from excessive x-ray photon noise", Med. Phys. 25, 2139-47 (1998)

[18]D. J. Moseley, J. H. Siewerdsen and D. A. Jaffary, "High-contrast object localization and removal in cone-beam CT," Proc. of SPIE Vol.5745, 40-50 (2005)

[19]A. Docef, M. Murphy, P. Keall et al., "Deformed CT reconstruction from limited projections," Proc. of CARS Vol. 1281, 104-8 (2005)

[20]R. J. Murphy, S. Yan, J. A. O'Sullivan, D. L. Snyder, B. R. Whiting, D. G. Politte, G. Lasio, and J. F. Williamson, "Pose estimation of known objects during transmission tomographic image reconstruction," IEEE transactions on medical imaging, vol. 25, no. 10 (2006)

[21]J. F. Williamson, B. R. Whiting, J. Benac, R. J. Murphy, G. J. Blaine, J. A. O'Sullivan, D. G. Politte, and D. L. Snyder, "Prospects for quantitative computed tomography imaging in the presence of foreign metal bodies using statistical image reconstruction," Med. Phys. 29, 2404-18 (2002)

[22]M. J. Murphy and D. A. Todor, "Demonstration of a forward iterative method to reconstruct brachytherapy seed configurations from x-ray projections," Phys. Med. Biol. 50, 2715-37 (2005)

[23]D. Pokhrel, M. J. Murphy, D. A. Todor, E. Weiss and J. F. Williamson, "Clinical application and validation of an iterative forward projection matching algorithm for permanent brachytherapy seed localization from conebeam-CT x-ray projections," accepted for publication in Med. Phys. 37, 5092-5101 (2010)

[24]D. Pokhrel, M. J. Murphy, D. A. Todor, E. Weiss and J. F. Williamson, "Reconstruction of brachytherapy seed positions and orientations from conebeam-CT x-ray projections via a novel iterative forward projection matching," accepted for publication in Med. Phys. September (2010)

[25]S. L. Schoeppel, B. A. Frass, M. P. Hopkins et al., "A CT-compatible version of the Fletcher system intracavitary applicator: clinical application and 3-dimentional treatment planning," Int. J. Radiat. Oncol. Biol., Phys. 17, 1103-09, (1989)

[26]N. Milickovic, S. Giannouli, D. Balats et al., "Catheter autoreconstruction in computed tomography based brachytherapy treatment planning," Med. Phys. 27, 1047-57 (2000)

[27]S. Li, C. A. Pelizzari, C. Reft, H. G. Sutton and G. T. Y. Chen, "Computer-aided geometric reconstruction of Fletcher-Suit source positions," Med. Phys. 21, 1123-30 (1994)

[28]S. Haack, S. K. Nielsen, J. C. Lindegaard et al., "Applicator reconstruction in MRI 3D image-based dose planning of brachytherapy for cervical cancer," Radiother. Oncol. 91, 187-93 (2009)

[29]A. C. Leeuw, M. A. Moerland, C. Nomden et al., "Applicator reconstruction and applicator shifts in 3D MR-based PDR brachytherapy of cervical cancer," Radiother. Oncol. 93, 341-46 (2009)

[30]J. P. Calatayud, F. Kuipers, F. Ballester et al., "Exclusive MRI-based tandem and colpostats reconstruction in gynecological brachytherapy treatment planning," Radiother. Oncol. 91, 181-86 (2009)